Elements for the Design of Precision Machine Tools and their Application to a Prototype 450mm Si-Wafer Grinder

by

Gerald Rothenhöfer

S.M., Massachusetts Institute of Technology, 2007
Dipl.-Ing. University of Stuttgart, Germany, 2005

Submitted to the Department of Mechanical Engineering
in partial fulfillment of the requirements for the degree of

Doctor of Philosophy

at the

MASSACHUSETTS INSTITUTE OF TECHNOLOGY

August 2010
[September 2010]

ARCHIVES

Signature of Autho

Department of Mechanical Engineering
August 27, 2010

Certified by: _____

Alexander H. Slocum
Professor of Mechanical Engineering, MacVicar Faculty Fellow
Chairman of the Committee, Thesis Advisor

Accepted by: _____

David E. Hardt
Professor of Mechanical Engineering
Chairman, Committee for Graduate Students

Elements for the Design of Precision Machine Tools and their Application to a Prototype 450mm Si-Wafer Grinder

by

Gerald Rothenhöfer

Submitted to the Department of Mechanical Engineering

on August 27, 2010, in Partial Fulfillment of the

Requirements for the Degree of

Doctor of Philosophy

ABSTRACT:

Keywords: adjustable kinematic couplings, hydrostatic bearings, feed back control, structural loop

Next generation precision machines will require ever more rigid elements to achieve the required machining tolerances. The presented work focuses on the application of ultra stiff servo-controllable kinematic couplings and hydrostatic bearings to minimize the structural loop of multi-axis precision grinding machines while reducing complexity.

The fundamental importance of these ultra stiff, adjustable machine elements is demonstrated in the design of a grinding machine for 450mm diameter silicon wafers. A new generation of silicon wafer grinding machines is needed to back-grind large (450mm diameter) wafers from the production thickness of up to 1mm down to less than 50µm so as to reduce the cost of Si-wafer based components.

The grinding process needs to be done in about 90 sec (fine-grinding, e.g. -200 micron) to 160 sec (coarse grinding, e.g. -600 micron). After completion of the fine grinding process the wafer must be flat to 0.1µm/□45mm and parallel to 0.6µm/450mm diameter. The surface roughness must be less than R_{ymax} 0.1µm and R_a 0.01µm.

Even though the required machining forces are <10N, the machine must be extremely rigid in order to achieve the necessary surface quality with a reasonable grinding feed-rate. Assuming a feed-rate of 5m/min and a total allowable error motion of 5nm, a stiffness of >1 N/nm is required, which is many times stiffer than a typical machine tool (0.1 to 0.3 N/nm).

In cooperation with industry, this work had the aim of creating a new machine design philosophy, with an example application that focuses on nano-adjustable kinematic coupling and feedback controlled water hydrostatic bearing technology. This new design philosophy is needed to enable the design of a relatively small footprint, compact precision machines.

In particular, a ball screw preloaded height adjustable kinematic coupling and a magnetically preloaded hydrostatic thrust bearing were designed and built. The adjustable kinematic coupling allows for up to 8mm of vertical height adjust and 7N/nm stiffness at 26 kN preload. By varying the preload on the coupling by +/- 10%, in-process nm to micron height and tilt adjustment at >95% of the nominal stiffness is possible.

Under the assumption of a constant flow supply, the hydrostatic bearing achieves a theoretical stiffness of 1N/ nm at a 20 micron bearing gap and 7000 N combined gravitational and magnetic preload. In practice, the stiffness is limited by the pressure flow characteristics of the supplying pumps. To increase the bearing stiffness to a required 4N/ nm, various control loops have been developed and tested.

Thesis Supervisor: Alexander H. Slocum
Title: Professor of Mechanical Engineering, Mac Vicar Faculty Fellow

1 Introduction

To manage cost of increasingly complex semiconductor devices (Integrated Circuits,ICs), such as on chip systems or photovoltaic cells, manufacturing productivity must be increased.

Figure 1 and Figure 2 show the manufacturing productivity as measured in dies per wafer for different target IC sizes as well as different wafer diameters. A generally accepted rule of thumb is that doubling the wafer area reduces unit cost by 20% to 30%.

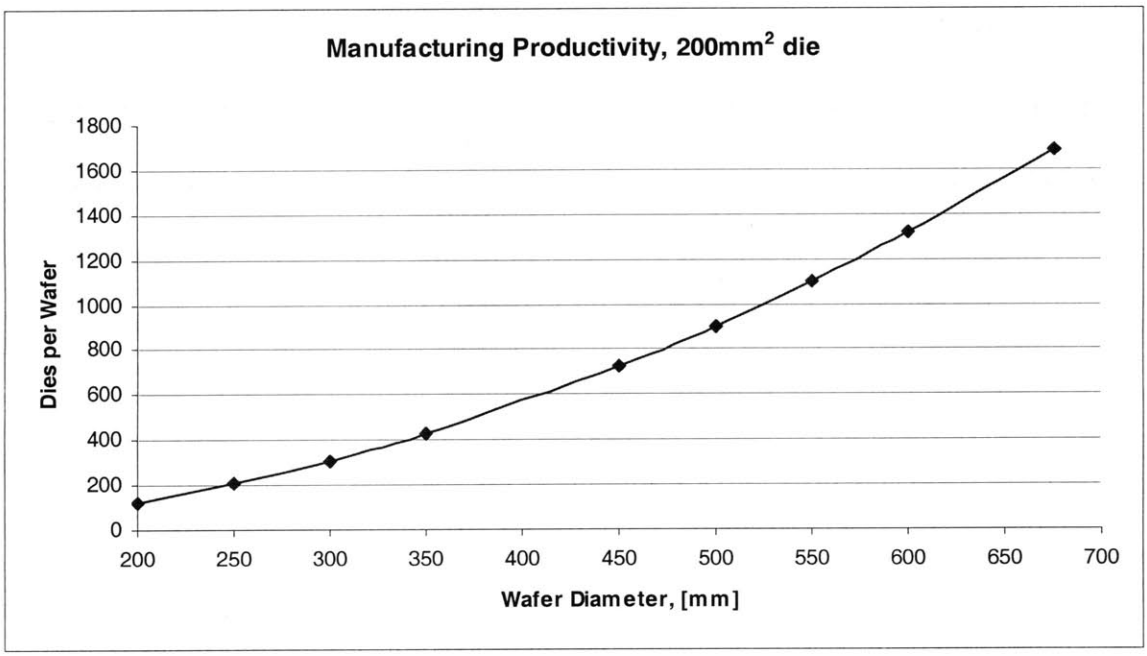

Figure 1: manufacturing productivity for different wafer sizes, 200mm² IC

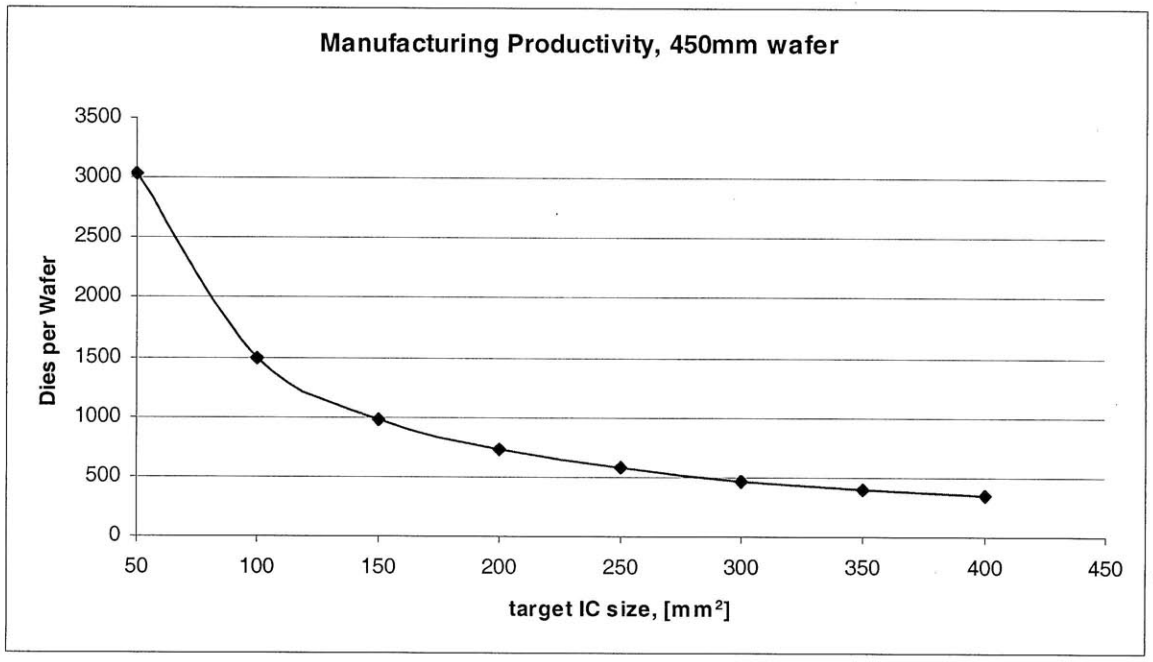

Figure 2: manufacturing productivity for different IC sizes, 450mm wafer

Increasing the wafer diameter, while maintaining roughly constant manufacturing cycle times, requires stiffer and therefore more accurate manufacturing equipment, Figure 3.

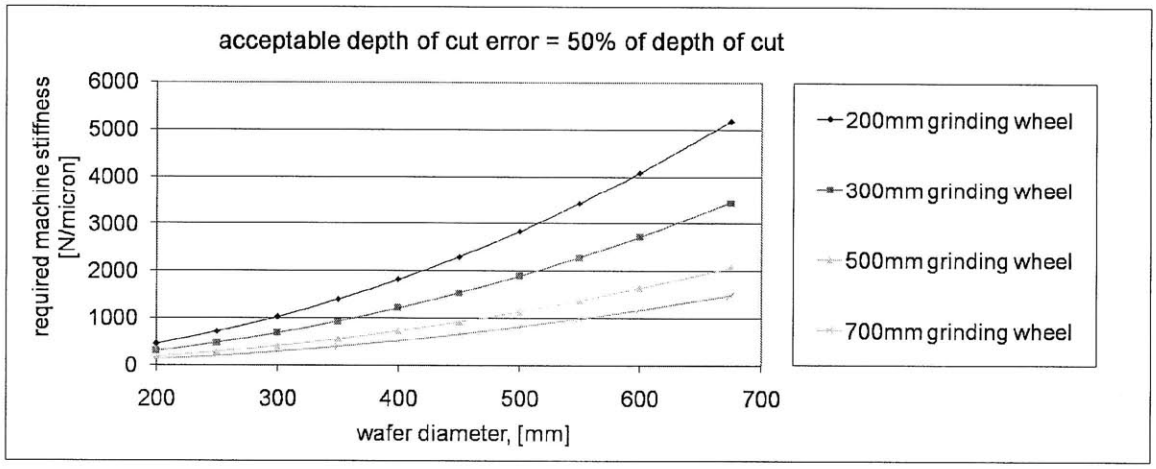

Figure 3: required machine stiffness for accurate grinding of Si-wafers

Since the beginning of microelectronics high purity silicon wafers have been the raw materials for computer chips, photovoltaic cells and other microelectronic devices. In 1965 Fairchild Semiconductor presented the first Integrated Circuit on a Silicon substrate.

Depending on the application, different wafer materials such as Gallium Phosphide (GaP), Lithium Tantalate (LiTa) and many others are also available [1]. However, in industry use, the size of non-silicon wafers is typically limited to about 100mm in diameter due to the finite mechanical strength of the respective material at a required wafer thickness. Generally, the wafer must withstand gravitational loading without cracking during handling [2].

Silicon wafers are formed of up to 99.9999% pure, nearly defect-free, mono-crystalline material. Different crystal growth processes such as the Czochralski process, where a seed crystal is slowly pulled out of a melt, are used to form a cylindrical ingot of highly pure silicon. In consequent manufacturing steps the wafer is cut from the ingot using a wire saw, lapped or ground to its final thickness, etched/cleaned and polished. Other manufacturing steps include edge profiling, and marking of the crystal grid orientation (Miller index) on the raw wafer.

While in 1990 the diameter of high purity silicon wafers was limited to 200mm, nowadays 300mm is standard and companies are working on machines to manufacture and handle 450mm wafers. According to the International Roadmap for Semiconductors (ITRS) the first 450mm wafer machines are expected to come to the market by 2012. By 2019 the International Roadmap for Semiconductors (ITRS) indicates that the wafer diameter will continue to grow to 675mm. However due to the remaining, unsolved technical hurdles, the high investment cost related to equipping a 450mm silicon wafer factory and the ongoing economic crisis, the introduction of 450mm silicon wafers might get delayed until 2017 or even 2019. Some of the technical hurdles that will need to be overcome include vibrational problems, gravitational bending, achieving of the required flatness and surface quality as well as defect free production and handling of 450mm ingots,

which will be three times heavier than the 300mm ingots and take up to four times longer to cool and twice as long to process. In short: 450mm wafers will require fundamental research and development efforts that go beyond just evolving and refining 300mm technology.

Past experience with the step from 200mm wafers, that could be manufactured in barely automated factories to 300mm wafers, that require full automation, taught companies, that despite the cost savings related to a bigger wafer diameter, it can take a long time to break-even with an initial investment. For instance the industrial use of 300mm wafers started in 2000 and reduced the price per die by about 30%-40%, but by the end of 2005 the more complicated and more expensive 300mm technology only had a 20% worldwide market share.

As mentioned previously, the driving force behind the trend for bigger wafers is the need to manage cost of larger system-on-a-chip devices and to decrease cost e.g. of photovoltaic cells – one key element to a more sustainable energy future. By increasing the wafer diameter substantial savings in the unit (die) cost are possible as the output per wafer process step (batch process) almost increases with the square of the wafer diameter. Furthermore with larger wafers relatively less surface area remains unused along the edges of the wafer. Not taking into account the surface area cost of defects as well as alignment or test features on the wafer, the idealized die per wafer count can be approximated by the following formula.

$$DPW=\frac{\pi d^2}{4S}-\frac{\pi d}{\sqrt{2S}} \quad (1\text{-}1)$$

DPW – Dies per Wafer

d – wafer diameter, [mm]

S – target IC size, [mm^2]

Besides the previously discussed points, the ITRS indicates that the wafer manufacturing process will have to be altered as conventional lapping can not fulfill the sub-surface damage requirements for wafer diameters over 300mm. Therefore future generations of silicon wafers are expected to be manufactured in a process chain with less manufacturing steps (no lapping), which puts more stringent requirements on future silicon wafer grinding machines. In order to not exceed the maximum allowed thickness of the sub surface damage layer (SSD), an increase in wafer diameter either requires a slower grinding feed-rate or a stiffer machine. According to [3, 4] "wafer grinding is not just an ordinary surface finish". Next to the reduction of sub-surface damages (SSD) resulting of disturbances of the silicon crystal grid or cracks the total thickness variation (TTV) and the overall thickness range of the wafer are important quality indicator. TTV is a measure of flatness and presently should be below 1µm for the finished wafer.

[5, 6] identify face grinding as the most promising approach to achieve the above mentioned requirements. Face grinding describes a process where a rotating cup wheel whose axis is usually displaced relative to the work piece's (wafer) axis of rotation feeds axially into the rotating wafer which is attached to a vacuum chuck in order to prevent the introduction of stress, Figure 4. The benefit of this grinding method lies in an inherently constant grinding force due to the continuous contact between the cup wheel and the wafer.

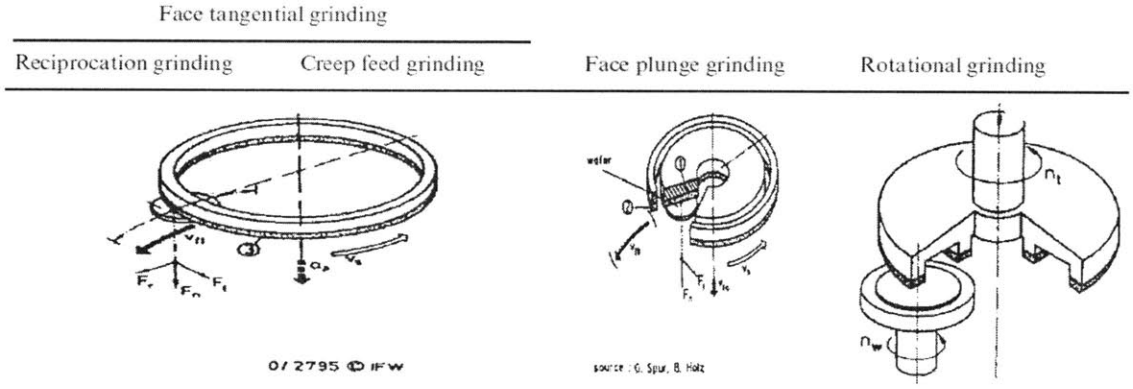

Figure 4: Face grinding schematic illustration as of [7]

Chapter 2 of this thesis presents machine requirements for the grinding of 450mm silicon wafers including a mathematical derivation of the required machine loop stiffness. It is shown that in order to successfully grind Si-wafers, while maintaining present manufacturing cycle times, future grinding machines must exceed a loop stiffness of 1000N/µm.

Chapter 3 introduces hydrostatic bearings as one key element to achieving the required loop stiffness. It is shown that the required element stiffness of >4000N/µm for a hydrostatic thrust bearing can only be reached by either applying an extremely high preload while running the bearing at the smallest possible gap (≈10µm) or by using feedback to control the bearing gap.

Chapter 4 describes the design and testing of a multi-pocket, magnetically preloaded hydrostatic thrust bearing, which was designed to reach an open loop, axial stiffness of >1000N/µm at a ≤20µm bearing gap. After examining a dynamic model of the bearing, different control algorithms to boost the axial stiffness to the required ≥4000N/µm are presented. Tests of a full scale prototype bearing, supplied by low cost, $50 gear pumps revealed an achievable closed loop bandwidth of 10Hz with the main limiting factor being

the pressure dependence of the supply flow and the pressure ripple caused by each gear tooth.

Chapter 5 consists of a journal publication that presents the design and testing of an adjustable kinematic coupling for use in machine tools with high required loop stiffness. Testing of a prototype has confirmed a theoretical stiffness of >7N/nm. Friction in the chosen "harmonic drive + ball screw" preload mechanism and the Hertz interface limited the adjustment resolution of the coupling. Suggestions for improvement of the presented coupling have been made.

Chapter 6 presents concepts for 450mm silicon wafer grinding machines and explains the decisions that lead to the final machine design, consisting of a radial and axial hydrostatic bearing work spindle, a wheel spindle with an electromagnetic thrust bearing and self compensating hydrostatic radial bearing, a simple yet extremely stiff machine structure and a new adjustable kinematic coupling for use in machine tools with high required loop stiffness. The electromagnetic wheel spindle was design in cooperation with a Professor Xiaodong Lu's research group at the University of British Columbia. For detailed description of the wheel spindle the reader is directed to Matthew Paone's master thesis (University of British Columbia).

Chapter 7 summarizes what has been achieved and what remains to be done to move from a real scale prototype to a manufacturing level machine.

2 Silicon Wafer Grinding Requirements

Figure 5 illustrates the original ITRS target schedule for wafer manufacturing. The introduction of 450mm wafers was originally expected for 2012, but due to a multitude of

unsolved technical problems as well as the on-going economic crisis, some estimates expect an introduction no earlier than 2017 or even 2019.

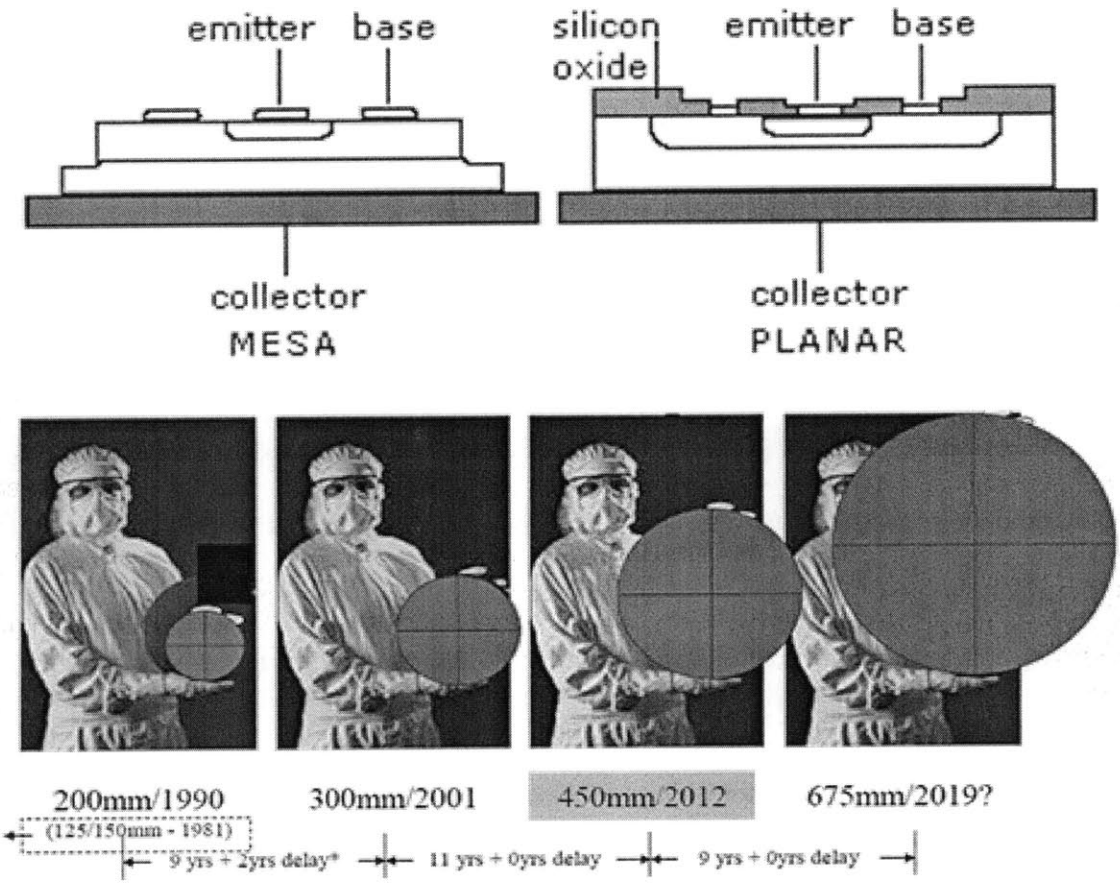

Figure 5: Silicon wafer diameter according to roadmap, [8]

Chapter 1 explains why the trend to bigger wafer diameters, as shown in Figure 5, is desirable from a manufacturing process efficiency as well as cost perspective. This chapter will focus on deriving the machine requirements for grinding larger diameter silicon wafers.

In face grinding of silicon wafer the grinding wheel is usually advanced axially into the wafer at a controlled feed-rate. If the grinding machine and wheel were infinitely stiff, the position of the grinding wheel relative to the original wafer surface would always be known accurately. However, given finite machine stiffness, the grinding process

accuracy can hardly be known exactly. Consequently to stay below a maximum allowable error motion the machine must be of a minimum required stiffness. The following, simplified, mathematical model provides an estimate for the required machine stiffness to achieve a sufficient surface quality at an acceptable feed-rate.

$$q = \frac{\pi d_w^{\,2}}{4} f \tag{2-1}$$

$$P = E_0 q \tag{2-2}$$

$$F_{tangential} = \frac{P}{\omega_s d_s} = \frac{E_0 \pi d_w^{\,2} f}{2\omega_s d_s} \tag{2-3}$$

$$F_{normal} = \frac{F_{tangential}}{\lambda} \tag{2-4}$$

$$a = \frac{2\pi f}{\omega_s} \tag{2-5}$$

$$F_{normal} = \frac{E_0 d_w^{\,2}}{4\lambda d_s} a = k_g a \tag{2-6}$$

$$k_g = \frac{E_0 d_w^{\,2}}{4\lambda d_s} \tag{2-7}$$

$$a = a_n - \delta \tag{2-8}$$

$$\delta = \frac{F_{normal}}{k_m} \tag{2-9}$$

$$\lambda \approx \frac{1}{1.3} \tag{2-10}$$

$$E_0 \approx 7 \frac{GJ}{m^3} \tag{2-11}$$

$$asssume:\ d_w = d_s = 450mm \tag{2-12}$$

$$k_m \geq (\frac{a_n}{\delta} - 1) k_g \tag{2-13}$$

$$k_m \geq (\frac{a_n}{\delta} - 1) \frac{E_0 d_w^{\,2}}{4\lambda d_s} \approx (\frac{a_n}{\delta} - 1) * 1035 \frac{N}{\mu m} \tag{2-14}$$

q – material removal rate

$F_{tangential}$ – tangential grinding force (relative to wafer surface)

F_{normal} – normal grinding force (relative to wafer surface)

d_s – wheel diameter

d_w – wafer diameter

ω_s – wheel speed

ω_w – wafer speed

f – axial federate

P – grinding power

E_0 – specific grinding energy

λ – process constant

a – depth of cut

k_g – process stiffness

k_m – required machine stiffness

a_n – nominal depth of cut per revolution of wafer

a – actual depth of cut per revolution of wafer

δ – depth of cut error

Typically precision wafer grinding requires error motions as small as 5 to 25nm [9]. Equation (2-14) indicates that a maximum depth of cut error of 5nm and loop stiffness of 1000N/µm, result in a maximum depth of cut per revolution of 10nm. At a typical work table speed of 500rpm this would correspond to a rather low feed-rate of 5µm/min. A 25nm maximum depth of cut error would result in a depth of cut of 50nm and thus a feed-rate of 25µm/min.

allowable total error motion	[nm, m]	**5**	5.00E-09
wheel diameter	[mm, m]	**500**	0.500
wafer diameter	[mm, m]	**450**	0.450

specific grinding energy	[GJ/m^3, J/m^3]	**7**	7.00E+09
Lambda	Ftangential/Fnormal		**0.77**
work spindle speed	[rpm, rad/sec]	**400**	41.89
wheel spindle speed	[rpm, rad/sec]	**2500**	261.80
machine stiffness	[N/µm, N/m]	**1000**	1.00E+09
process stiffness	[N/µm, N/m]	921	9.21E+08
max depth of cut per rev	[nm/rev, m/rev]	10.43	1.04E-08
feed-rate	[µm/min, m/sec]	4.17	6.95E-08
tangential grinding force	[N]		1.18
normal grinding force	[N]		1.54
machine stiffness * error motion	[N]		5

Figure 6: error motion based maximum feed-rate calculation

The main uncertainty in this simplified model lies in the value that has been chosen for the specific grinding energy. Process parameter research indicates that the specific grinding energy can be significantly higher depending on process parameters as well as the choice of the grinding wheel material [10]. However, uncertainty in the specific grinding energy would only cause even more stringent stiffness requirements or lower feed-rates and thus not significantly alter the conclusion of this estimate. It should be clear that in order to grind 450mm wafers, a machine of significant stiffness (≥1000N/µm) and extremely low error motions in the direction of material removal will be needed.

In order to determine component requirements with respect to stiffness and error motion, a closer look must be taken at the structural loop of the machine. Generally a face grinding machine will require at least two rotational and one translational axis of motion. Typically these are rotation of the wafer (work spindle), rotation of the grinding wheel

(wheel spindle) and material removal (typically integrated in wheel spindle). In conventional machines, such as proposed by [3], additional axes are added to move the wafer / work spindle between the grinding station and a wafer handling station or to move the wheel spindle into a position that is adequate for exchanging the grinding wheel.

This thesis proposes a novel, fundamentally three axes (two rotational + one translational + two axis tilt adjust to position the grinding wheel) machine design that reduces the length of the structural loop to the bare minimum. In order to meet requirements that compete with a minimum structural loop, such as space for exchanging the grinding wheel (industry specification is 300mm between the wheel and the work table surface), the machine needs to have two configurations:

- grinding configuration: minimum structural loop, maximum stiffness
- work preparation configuration: sufficient space for wafer handling and wheel exchange, no critical stiffness

A structural interface element is needed to switch between the two configurations with high repeatability while maximizing stiffness in the grinding configuration. In addition, according to industry requirements the interface element must have 8mm of height adjustability to compensate for wear in the grinding wheel.

When in the grinding configuration the machine essentially consists of four elements that are mechanically in series. Each of these elements is assigned a component stiffness, which must be high enough to achieve the required overall machine stiffness, Figure 7.

Component stiffness	[N/nm]	[N/nm]
Work spindle	4	4
Machine structure	3	5
Machine interface	7	7
Wheel spindle	4	3
Total [N/nm]	1024	1080

Figure 7: two versions of potential component stiffness budget

Furthermore the work and wheel spindle are assigned a maximum allowable error motion, such that even in a worst case scenario the allowable maximum error motion of (5-25nm) is not exceeded, e.g. Figure 8.

Allowable error motion	Nm
Work spindle	10
Machine structure	0
Machine interface	5
Wheel spindle	10
Total [nm]	25

Figure 8: component error motion budget

In addition to minimum stiffness and maximum error motion the following industry requirements also had to be met:

Work spindle:

- rotational speed of 10 to 500 rpm
- torque of 63Nm
- 500 mm table diameter
- 450mm wafer diameter

Wheel spindle:

- rotational speed of 2500rpm
- 45Nm torque, 11kW net spindle power
- two axes tilt adjust (+/-250μm over 500mm)
- +/-2mm of axial stroke
- Rapid feed-rate of 150mm/min
- Feed-rate 1 to 999 μm/min
- 500mm cup wheel for grinding
- Work spindle to wheel spindle axis offset of 249mm

Interface Element:

- can be opened by 300mm (wheel spindle to work spindle face to face distance) to exchange the grinding wheel
- 10mm of height adjustability in grinding configuration to compensate for wear in the grinding wheel.

Finished Wafer Requirements:

- total thickness variation (TTV) ≤0.5μm per 100wafers
- wafer to wafer variation (WTW) ≤1μm per 100wafers
- Flatness : 0.1 μm / 20mm
- Parallelism : 0.6 μm /450mm

3 Bearings as a Key Element for the Design of Ultra Stiff Machine Tools

After having outlined the essential requirements for 450mm wafer grinding in the previous chapters, this chapter focuses on the bearing technology that is needed for the design of precision machine tools with a loop stiffness exceeding 1000N/µm.

All bearings can be grouped in contact and non-contact bearings. Contact bearings can be split up in sliding and rolling contact bearings. Non-contact bearings are electro-magnetic and fluid bearings. Fluid bearings can be split up in aerostatic, aerodynamic, hydrostatic and hydrodynamic bearings.

In many applications contact bearings perform through their relatively low cost, good stiffness, reasonably low friction and high load capacity. Compared to sliding contact bearings, rolling element bearings have lower frictional losses, less wear and thus require less maintenance. Often those benefits come at the price of slightly bigger error motions and a higher price. However, in precision applications where error motions must be limited to a couple µm or sub µm, rolling element bearings and sliding element bearings are usually not suitable.

Generally, a higher precision and a longer useful bearing life time can be achieved using non-contact rather than contact bearings. Non contact bearings can be grouped in fluid bearings and electro-magnetic bearings (electro-magnetic levitation). Electro-magnetic levitation bearings have been a common choice for precision applications such as semi conductor manufacturing equipment or atomic measuring machines. Often electro-magnetic bearings are designed for high precision which usually comes at the price low

force output and consequently low dynamic stiffness at the order of several hundreds N/μm [11, 12, 13, 14, 15].

Non-contact fluid film bearings combine many of the benefits of electro-magnetic bearings and rolling element bearings. The fluid film of these bearings averages surface inaccuracies and thus reduces error motions. Furthermore the absence of mechanical contact eliminates wear and reduces required maintenance. Another important advantage for the use of non-contact bearings in semi-conductor equipment can be – depending on the used fluid - the absence of hydrocarbon based lubricants or wear-particles that would both be a potential source of process contamination.

Hydrodynamic and aerodynamic bearings require relative motion between the two bearing surfaces to support any load. This can result in significant friction at low relative velocities as well as during start-up and shut-down. Functioning independently of relative motion, hydrostatic and aerostatic bearings usually achieve a higher stiffness and load carrying capacity than hydrodynamic bearings. In a few cases hydrostatic and hydrodynamic effects can be combined in the design of a hybrid fluid bearing.

Due to the compressibility of air (gases) aerostatic bearings generally require a significantly higher preload to achieve the same stiffness as a comparable hydrostatic bearing. Furthermore, due to the finite stiffness of air (gases) aerostatic bearings can store potential energy that can be converted back into kinetic energy which can lead to oscillations (hammering). Hydrostatic bearings act as a gap modulated resistance that shows spring like behavior due to its gap dependency. However, by definition of a resistance, hydrostatic bearings can not store energy but only dissipate it. Therefore, if the dynamics of the supply system (pump, tubing, valves) are neglected, hydrostatic bearings can not oscillate.

However, the advantages of hydrostatic bearings compared to aerostatic bearings come at the price of some friction through fluid shear. Even though the friction of hydrostatic bearings is still extremely low compared to contact bearings, at high speeds, it can be high enough to cause significant warming of the bearing fluid and resulting thermal errors in the motion stage.

To summarize: compared to other bearings, hydrostatic bearings excel through high stiffness, damping, load capacity, precision of motion and the absence of wear. In applications that require a "clean" environment, such as semiconductor processing, a properly designed hydrostatic bearing can be supplied with a generally available fluid such as process coolant, grinding fluid or de-ionized water.

The physics of hydrostatic bearings are well understood and the design of hydrostatic bearings is subject to diverse publications and literature [16,17]. Extensive engineering literature also describes sophisticated restrictor and valve designs to increase the bearing stiffness ("infinite stiffness devices"). However, most literature neglects the dynamic interaction of the bearing with its supply system.

The only downside of non-contact fluid bearings in precision applications is that fluid shear can lead to significant temperature increase of the bearing fluid and it can be necessary to provide cooling in order to avoid thermal errors.

The following chapters qualitatively describe the functional principle of hydrostatic bearings, present a static and dynamic model of a single pocket bearing and its supply system, define requirements for the fluid supply system, evaluate different supply options and finally present strategies to control the bearing gap and/or increase the bearing stiffness.

3.1 Functional Principle of Hydrostatic Bearings

Generally speaking a hydrostatic bearing works similarly to an air hockey table. In the case of a hydrostatic bearing the "puck" floats on an ideally incompressible bearing fluid (e.g. water) instead of on air, and the puck is a part of a machine tool.

Hydrostatic bearings support loads by pressuring a bearing fluid such as oil or water into a bearing pocket. The bearing fluid is then pushed out of the pocket through a narrow gap (hydrostatic gap) between the stationary table and the movable carriage that carries the load. Depending on the gap height and the volume flow rate pressure is build up inside the pocket. This pressure carries the carriage and the load on top of the carriage. Unless the maximum load capacity of the bearing is exceeded, the carriage floats on a thin film of fluid. The maximum load capacity of the bearing mainly depends on the size (area) of the pocket and the supply system.

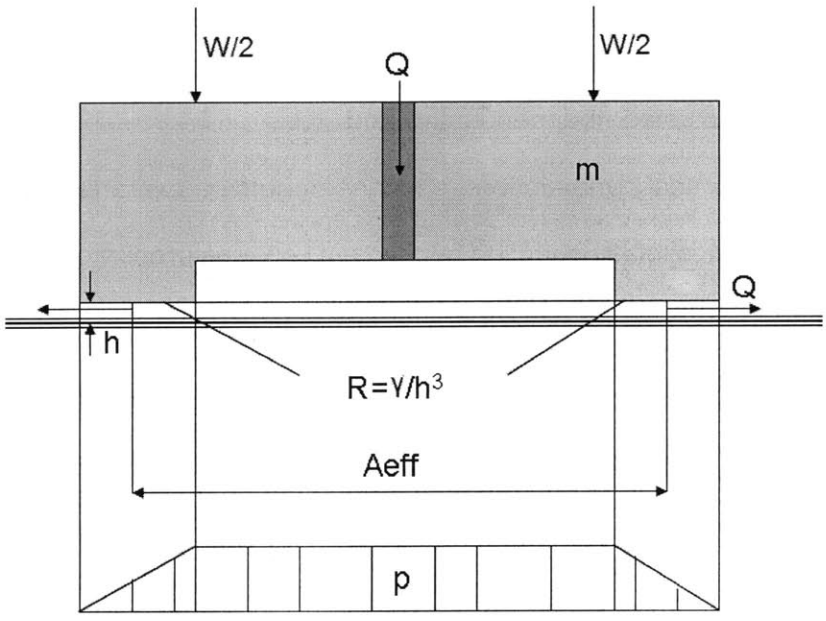

Figure 9: Schematic illustration of a hydrostatic bearing pocket

There are two different supply systems for hydrostatic bearings: constant pressure and constant flow. In the case of a constant pressure supply a restrictive element such as an orifice or a capillary is put in between the bearing and a constant pressure reservoir. If the bearing load increases, the bearing gap decreases and less fluid flows out of the bearing. Thus the pressure drop over the restrictor decreases and a higher pressure becomes available in the bearing. A constant flow bearing is usually supplied by a positive displacement pump. Ideally the flow of a positive displacement pump is proportional to the pump speed and pressure independent. If the load increases the gap decreases and so does the outflow resistance of the bearing. Thus the pressure in the bearing increases. Alternatively servo-valves can be used to maintain a nearly constant flow over a limited pressure range.

In comparison, a constant flow supply is stiffer and more efficient than a constant pressure supply as no pumping power gets lost in a restrictor. Furthermore, over time restrictive elements, as needed for a constant pressure supply, can clog with particles or biological growth. In addition a constant flow supply has the advantage that the flow in each bearing pocket can be adjusted independently and thus it is possible to compensate for unevenly applied loads, dynamic load changes or surface tolerances in the sliding rails. If the flow in each pocket is controlled such that it changes proportionally to a change in pressure in the corresponding pocket, theoretically infinite static stiffness can be achieved. Also it is possible to improve the dynamic response of the bearing to load changes by controlling the flow through each bearing pocket. This is explained in more depth in chapter 3.6, 3.7 and 4.

Some of the problems of a direct flow (or constant flow) supply versus a constant pressure supply are:

- each bearing pocket needs its own pump
- pressure independent flow is needed
- pressure and flow fluctuations caused by the pump must be kept to a minimum

In conclusion to the previous paragraphs, a constant flow supply appears as the better choice due to its higher efficiency / stiffness at given pumping power as well as the absence of a restrictive element that can wear or clog. The next chapter will discuss some of the difficulties that need to be taken into account when designing a constant flow bearing.

Independent of the supply system the bearing has to be preloaded to achieve bidirectional stiffness. The main purpose of the bearing pocket (the inner region of the bearing) is to create an area of uniform pressure to support load and to lift off the bearing from rest. The bearing lands and the bearing gap define the outflow resistance of the bearing. Furthermore the bearing lands determine the inherent "squeeze film damping" of the bearing. Squeeze film damping is the dissipation of energy through viscous flow (shear of the fluid) in the bearing gap. The bearing will only provide significant damping if the supporting structure (table) is much stiffer than the bearing itself.

3.2 Requirements for the Fluid Supply System

In order to not exceed a maximum allowable error motion, it is necessary to reduce pressure and flow fluctuations that originate from the supply system of the bearing. In constant pressure supplied bearings accumulators are used to dampen pressure and flow fluctuations that originate from the pump and thus to maintain a constant supply

pressure. Generally it is much harder to supply a bearing with a truly constant flow. Therefore, especially for a constant flow supplied bearing, the effect of flow and resulting pressure variations on the bearing performance needs to be taken into account when choosing a pump.

Starting from the design equations for hydrostatic bearings the maximum allowable flow and pressure ripples can be calculated:

$$p = Q_{out} R = Q_{out} \frac{\gamma}{h^3} \tag{3.2-1}$$

$$p = \frac{W}{A_{eff}} \tag{3.2-2}$$

$$h = (\frac{Q_{out} A_{eff} \gamma}{W})^{\frac{1}{3}} \tag{3.2-3}$$

$$\frac{\partial h}{\partial Q_{out}} = \frac{1}{3}(\frac{Q_{out} A_{eff} \gamma}{W})^{-\frac{2}{3}} \frac{A_{eff} Q_{out} \gamma}{W} \tag{3.2-4}$$

$$h = h_0 + 3\frac{W_0}{h_0}\Delta h + \frac{1}{3}(\frac{Q_{out_0} A_{eff} \gamma}{W_0})^{-\frac{2}{3}} \frac{A_{eff} \gamma}{W_0} \Delta Q_{out} \tag{3.2-5}$$

$$h = h_0 + 3\frac{W_0}{h_0}\Delta h + \frac{1}{3} h_0 \frac{\Delta Q_{out}}{Q_{out_0}} \tag{3.2-6}$$

$$\left[\frac{1}{3}(\frac{Q_{out_0} A_{eff} \gamma}{W_0})^{-\frac{2}{3}} \frac{A_{eff} \gamma}{W_0} \Delta Q_{out} = \frac{1}{3} h_0 \frac{\Delta Q_{out}}{Q_{out_0}} \right] \leq e \tag{3.2-7}$$

$$\Delta p = \Delta Q_{out} R_0 \tag{3.2-8}$$

Q_{out}, ΔQ_{out} – pocket out flow, flow ripple

p, Δp – pocket pressure, pressure ripple

W – bearing preload per pocket

A_{eff} – effective pocket area

R – pocket outflow resistance

γ – pocket resistance factor

h – bearing gap

e – acceptable error motion

The flow and pressure ripples of a pump depend on the pump type as well as the specific design. For instance in gear pumps, details such as tooth shape, number of

teeth on the driving and driven gear as well as mechanical tolerances can significantly influence the flow ripple [18].

If flow ripple is of concern, the bearing can be designed for a higher flow rate by decreasing the land width. However a smaller land width and resulting higher required flow rate also linearly increase the required pumping power while decreasing the dissipated friction power by the same factor. The designer needs to confirm that the total dissipated power consisting of pumping power and friction power, which will ultimately be converted into heat and increase the temperature of the bearing fluid, stays below an acceptable limit.

Alternatively the bearing gap can be changed. For a given bearing increasing the gap by a factor x will require a flow increase of x^3 and therefore reduce the resulting gap vibration by x^2 (assuming that the flow ripple remains unchanged). However increasing the gap by x will also decrease the stiffness the same amount.

Another point that needs to be taken into account, especially when choosing a constant flow supply, is the pressure flow characteristic of the pump. Any change in pump flow due to bearing load variations will influence the apparent bearing stiffness (see eqn. (3.2-6)). Therefore, in order to achieve optimum bearing stiffness, either a pump that can produce a pressure independent flow over a required pressure range must be chosen or the pump speed must be changed depending on the bearing pressure. Alternatively the flow can be measured and controlled. However, especially if the bearing was designed for a low supply flow, flow measurement and control can be difficult and expensive.

3.3 Pump Options for Constant Flow Supplied Bearings

The previous chapter pointed out the importance of pressure independent flow for the performance of a constant flow supplied bearing. Due to their pressure flow characteristics centrifugal pumps and other non-positive displacement or variable displacement pumps are not suitable to directly supply a hydrostatic bearing. Their use is limited to constant pressure supplied bearings, where the main task of the pump is to maintain a constant pressure inside an accumulator and where a relief or servo valve regulates the supply pressure.

In theory positive displacement pumps produce a pressure independent flow by capturing a defined amount of low pressure fluid and forcing it to the high pressure side of the pump. Generally positive displacement pumps can be grouped in reciprocating and rotary pumps. Examples of positive displacement pumps are:

- gear pumps
- diaphragm pumps
- peristaltic pumps
- piston pumps
- progressing cavity pumps
- screw pumps
- lobe pumps
- vane pumps
- regenerative (peripheral pumps)

Any positive displacement pump is plagued by internal leakage (back flow to the low pressure side) and thus can only produce a somewhat pressure dependent flow.

In addition most positive displacement pumps, by principle have a higher flow and pressure ripple than variable displacement pumps.

The following table shows a qualitative comparison of positive displacement pumps with respect to flow range, flow stiffness (pressure dependence of flow), flow ripple and pressure range. It is to be noted that the characteristics of different pump designs of the same category can vary tremendously. The following table can therefore only give a vague, qualitative overview.

	Flow range [l/min]	Flow stiffness	Flow ripple	Pressure range
Gear pumps	Very low to high volume	Medium	Medium	Medium
Diaphragm pumps	Very low to high volume	High	High	High
Peristaltic pumps	Very low to low	Medium	Low	Low
Piston pumps	Very low to high	High	High	Very high
Progressing cavity pumps	Low to high	Medium	Close to zero	High
Screw pumps	Low to very high	High	Close to zero	Very high
Lobe pumps	Low to high	Low	High	Medium
Vane pump	Low to medium	Low	High	Medium
Regenerative (peripheral) pump	Medium to high	Medium	Low	High

Figure 10: qualitative positive displacement pump comparison

Other than most piston pumps with a fast, reciprocating piston and a relatively small displacement per piston stroke, slow moving, high volume, double-acting piston pumps present a promising option to eliminate pressure ripple as well as pressure dependency of the output flow over at least the duration of one piston stroke. Chapter 3.4 presents the design of such a high volume piston pump.

In order to compensate for the previously mentioned back leakage and to achieve optimum bearing stiffness and load capacity, some kind of flow control has to be implemented to maintain a truly constant flow. In theory the flow can even be controlled such that a constant bearing gap and thus infinite static stiffness can be maintained over a limited pressure range. In the case of constant pressure supplied bearings this flow control can be done by servo valves. With a direct supply (constant flow) the pump

speed has to be changed to compensate for load variations. The following chapter describes methods to control the flow in a direct supply system for optimized bearing performance without using additional hardware in the supply line such as servo valves.

3.4 Design of a High Volume Piston Pump

To test the concept of a high volume piston pump with respect to pump internal leakage, pressure flow characteristics and smoothness of flow a commercially available, double acting Bimba air cylinder, with 2ft of stroke and 3.14in^2 piston area, was used to pump water. Figure 11 shows the design of a bench level prototype.

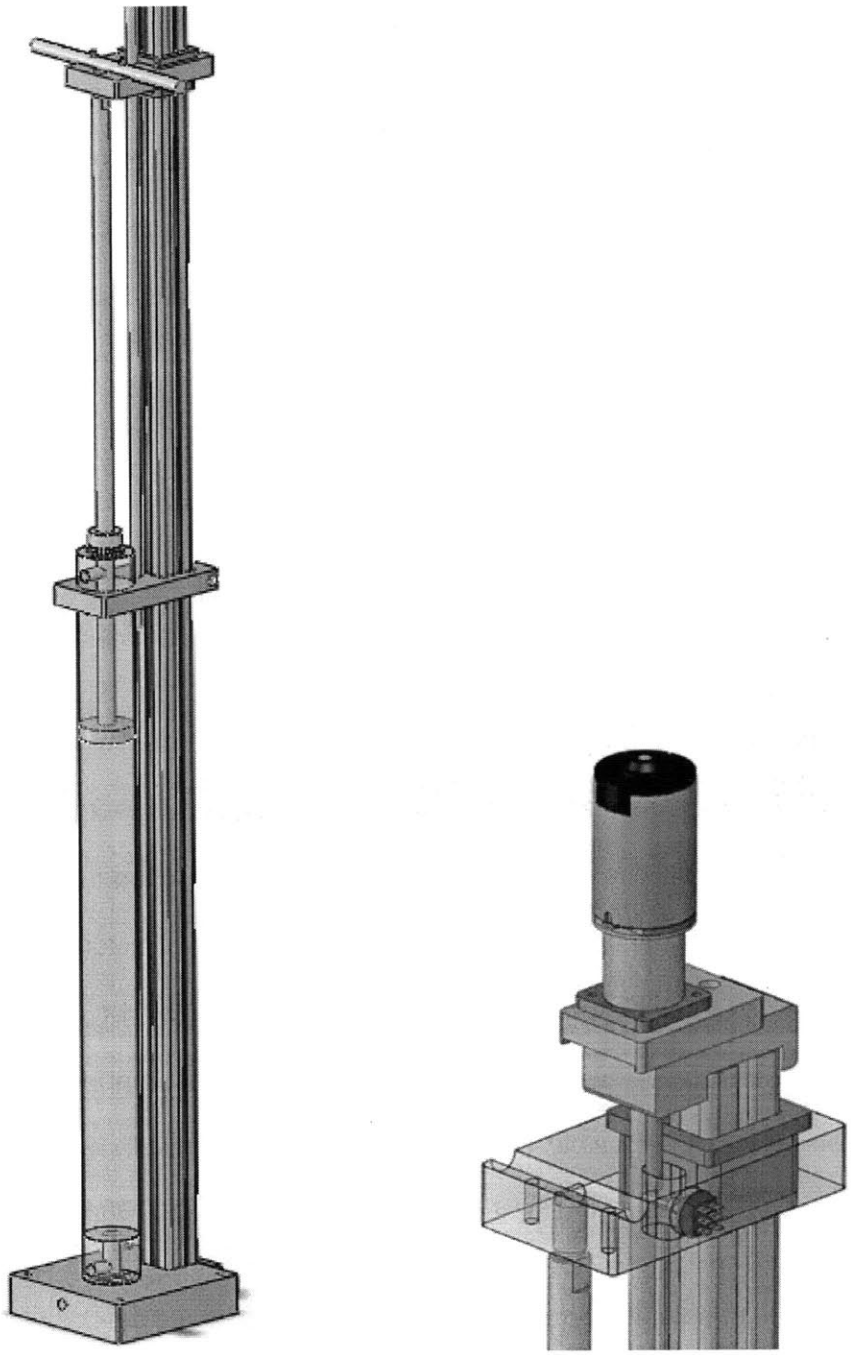

Figure 11: high volume double acting piston pump bench level prototype

A wire potentiometer was mounted between the stationary structure and the moving piston to measure piston motion.

In a first leakage test the piston was extended by about 20" and loaded with 60lbs of weights corresponding to a pressure of 20psi. Putting the weights on caused an initial displacement of about 0.8mm. This displacement was caused by compression of trapped air and deformation of the structure. Three days later the piston still had not moved any further (within 4/100in accuracy): I.e. over a time period of three days and at a pressure of 20psi the piston had leaked less than 0.007oz or 0.2ml. This is orders of magnitude better than could have been expected from any gear pump. It can be concluded that a high volume piston that is equipped with a sufficiently powerful, closed loop control positioning system can provide significantly higher flow stiffness i.e. pressure independent flow than alternative gear pumps.

One downside of using a double-acting piston is that the direction of motion has to be reversed once the piston has reached its end of travel. In this moment the outflow of the piston stops. If the piston is used to supply a hydrostatic bearing this would be unacceptable during the machining process. However, if the piston is dimensioned appropriately the reversal of direction can be timed with a break in the machining process (e.g. tool change). To reduce machine downtime it is important to switch the piston direction as fast as possible. With conventional electronically actuated valves or mechanical check valves switching times below 1sec can be achieved.

If continuous flow is absolutely required two double acting pistons can be used to supply the bearing. One piston would follow a $\sin^2$ motion while the other piston would follow a $\cos^2$ motion. Consequently when one piston is close to its switching point, its contribution to the total flow would be relatively low (close to zero) while the other piston produces maximum flow. To eliminate remaining pressure and flow fluctuations that

result of valve switching, filtering elements such as accumulators or other types of fluid borne noise silencers (Helmholtz resonators, expansion chambers, ...) can be used.

Figure 12 shows a first order estimate of relevant design requirements for a high volume piston pumps to supply a precision hydrostatic bearing.

pressure	[kPa]	60.00
flow	[ml/min]	500.00
piston diameter	[mm]	50.00
piston area	[mm^2]	1963.50
expected piston friction	[N]	10.00
required piston force	[N]	127.81
required piston speed	[mm/sec]	4.24
required actuator power	[mW, W]	542.44
time to empty piston	[min]	1
required piston stroke	[mm]	254.65
piston volume		500
nominal bearing gap	[micron]	25
bearing preload	[N]	7850
mechanical stiffness of bearing	[N/micron]	942
load step	[N]	70
mechanical deflection	[micron]	0.07
allowable flow variation as % of mechanical deflection	[%]	50%
allowable gap change due to flow variation	[micron]	0.04
allowable flow change	[%]	0.45%
allowable piston area percentage error	[%]	0.22%
piston area upper limit (+xxx%)	[mm^2]	1967.8
piston area lower limit (-xxx%)	[mm^2]	1959.2
piston diameter upper limit	[mm]	50.05
piston diameter lower limit	[mm]	49.94
max. piston diameter tolerance (upper limit)	[micron]	55
max. piston diameter tolerance (lower limit)	[micron]	-55
max. piston diameter tolerance range	[micron]	27.5
allowable piston velocity percentage error	[%]	0.22%
upper piston velocity limit	[mm/sec]	4.25
lower piston velocity limit	[mm/sec]	4.23
max. piston velocity tolerance (upper limit)	[micron/sec]	9
max. piston velocity tolerance (lower limit)	[micron/sec]	-9
max. piston velocity tolerance range	[micron/sec]	4.7
control bandwidth	[Hz]	10
linear encoder resolution	[micron]	0.47
rotary encoder resolution	[pulses per rev]	2000
max. allowable rotary to linear transmission ratio	[mm/rev]	0.93

Figure 12: hydrostatic bearing, high volume piston pump first order design requirements

3.5 Preload Options for Hydrostatic Bearings

In most bearing applications some sort of preload is used to improve motion accuracy or increase bearing stiffness. In contact bearings preload improves motion accuracy by elastic averaging over many load carrying rollers. The stiffness of contact bearings is improved by increasing preload on the (Hertz) contact interfaces of the bearing. The stiffness of non-contact, fluidic thrust bearings is directly linked to the bearing preload. Furthermore preload allows a fluid bearing to be bidirectional (as the fluid only provides repulsive force).

The stiffness of hydrostatic bearings scales proportional to the applied preload and inversely proportional to the bearing gap. Therefore, in order to achieve optimal stiffness the preload needs to be maximized while the bearing gap must be kept as small as possible. However, usually the smallest possible bearing gap is limited by manufacturing tolerances to 5 to 10µm. Therefore, often the most cost efficient way to increase the bearing stiffness is to increase the preload. The designer can choose from four preload options:

- gravity
- hydraulic
- pneumatic
- mechanical (springs)
- magnetic

Increasing bearing preload by gravity goes along with increasing the weight and volume of the floating machine component and is therefore relatively easy to do. In the case of a grinding machine the floating machine component is the rotating work table. However

the inertia of a moving machine component increases with its weight, which can require a bigger and therefore more expensive motor. Furthermore increasing the weight or volume of a component can complicate mounting a machine. Increasing the volume also makes the machine less compact and therefore ultimately can affect the overall machine stiffness. Other cost increases are related to the weight specific cost of the used material or the shipping cost of a bigger and heavier component.

The most common hydraulic preload for hydrostatic bearings are opposed pad bearings. The downsides of an opposed pad bearing design are increased space requirements as well as additional, costly precision surfaces. Compared to a single-pad-bearing, opposed-pad designs can easily double the cost of a bearing and its fluid supply system.

Similar to a hydrostatic, opposed pad design, aerostatic bearings can be used to preload a hydrostatic bearing.

Mechanical preload via springs usually requires contact between the moving components. If there is relative motion between the components an additional bearing interface becomes necessary (similar to an aerostatic or hydrostatic opposed pad design).

Another option to easily achieve preload forces of several thousand Newton is by using permanent or electro magnets. Permanent magnetic materials are extremely corrosive and therefore have to be coated if they are to be exposed to a corrosive medium such as can be the case in water hydrostatic bearings. Most magnetic steels also need to be protected, as they are not completely corrosion resistant, even if they should be labeled "stainless steel".

Electro magnets can be of concern because of the heat that they can produce.

If permanent magnets or electro magnets are used to preload a moving part eddy currents and related power losses (eddy current brake) must be taken into consideration.

Chapter 4.1 presents a permanent magnetic preload system for hydrostatic thrust bearings, illustrates encountered problems and proposes an improved design.

3.6 Dynamic Model of a Hydrostatic Thrust Bearing

The simplest way to model the reaction of a hydrostatic bearing to a load change is to consider it as a spring with a finite stiffness in parallel to a damper and preloaded by a mass. However, this model is not quite accurate since the bearing is essentially a resistance that is modulated by the hydrostatic gap. Obviously the bearings' reaction to a load change is a displacement. If the bearing is supplied with fluid from a positive displacement pump where the pump flow is proportional to the pump speed it is possible to increase the stiffness of the bearing by changing the pump speed depending on the pocket pressure or the bearing gap. As it is possible to change the bearing gap by changing the flow an increase in load (decrease of the gap) can be compensated by an increase in flow (increase of the gap). Theoretically it is possible to reach infinite stiffness by increasing the flow proportionally to the increase in pressure (as described above). However the pressure-flow characteristics of the pump, in the case of very slow load changes and the dynamics of the entire system in the case of dynamic load changes, limit the achievable stiffness.

The hydrostatic bearing gap can either be controlled by directly measuring the bearing gap or based on a model of the bearing, the flow (speed of a positive displacement pump) and the pressure in the bearing gap. Both, pump speed and pressure are easy to measure. Combined with a stiff machine frame (structure) such a feed-back controlled

hydrostatic bearing can significantly contribute to increase the accuracy of present wafer manufacturing equipment.

In the presented model the following simplifying assumptions have been taken:

- Fluid is incompressible
- No mechanical deformation of the supporting structure
- Laminar flow through the hydrostatic gap
- Density of fluid is zero (weightless fluid)
- Constant flow supply (under static load)

No limitation on pump speed or pressure. Therefore the simulation results have to be double-checked in regards to speed limits and pressure limits of the pump.

Under the assumption of constant flow the behavior of the bearing is dominated by its outflow resistance that is inversely proportional to the third power of the gap. The simplest model can be derived by linearizing this resistance as follows:

$$\frac{p}{Q_{out}} = \frac{\gamma}{h^3} \tag{3.6-1}$$

$$h = \left(\frac{Q_{out}\gamma}{p}\right)^{\frac{1}{3}} \tag{3.6-2}$$

$$h = -\frac{1}{3}\left(\frac{Q_{out}\gamma}{p}\right)^{-\frac{2}{3}} \frac{Q_{out}\gamma}{p^2}\bigg|_{p=p_0} p + h_0 \tag{3.6-3}$$

$$h = \frac{1}{3}\frac{h_0}{p_0} p + h_0 \tag{3.6-4}$$

According to the above equations the linearized outflow resistance acts like a spring. This coincides with the general observation that a hydrostatic bearing shows spring like behavior. The calculated stiffness is as found in diverse literature. However, this simplified model can not be correct since a modulated resistance (i.e. the outflow resistance) is an energy dissipator and thus should not be modeled as energy storage as in Figure 13. In this model R describes the previously mentioned squeeze film damping.

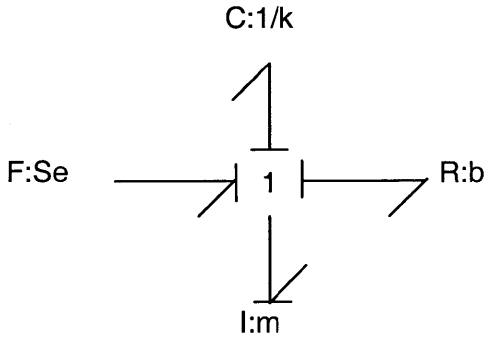

Figure 13: Bond graph model of a single pocket hydrostatic bearing, linearized outflow resistance

A better model of the bearing is shown in Figure 14.

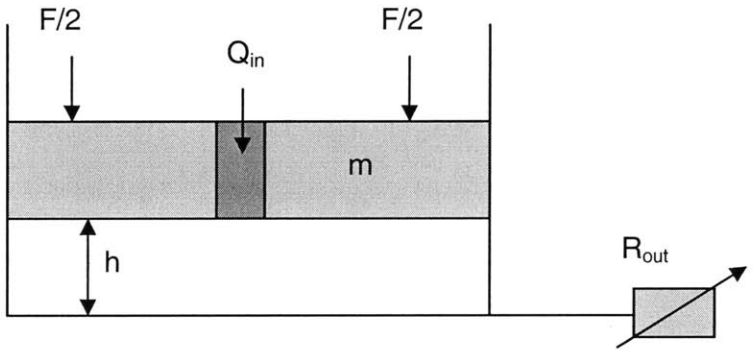

Figure 14: Model of a single pocket hydrostatic bearing

In the following model the weight of the column of bearing fluid within the bearing is neglected.

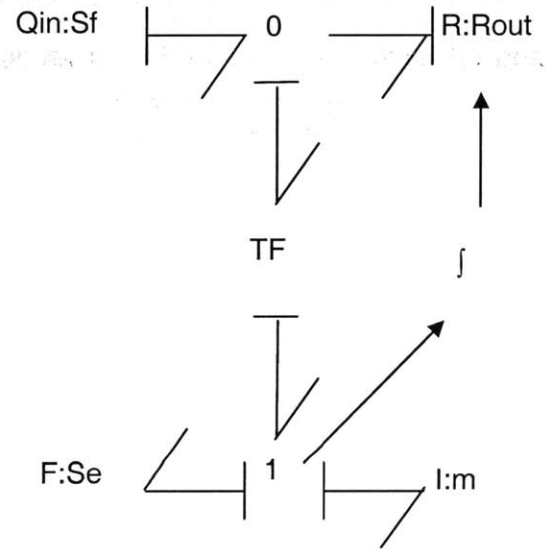

Figure 15: Model of a single pocket hydrostatic bearing

This model may seem complete. However, the reader should wonder why the inertia is in differential causality, since according to the bond graph it could as well be in integral causality. In theory integral causality is preferable due to more accurate computation. However, in this case it is not possible to run a simulation with the inertia in integral

causality. This can be visualized as follows: If the bearing is at rest and the gap is zero the outflow resistance is infinite. Consequently a step in flow will cause infinite pressure in the bearing and infinite acceleration of the bearing. In order to fix this problem the simulation can only be run starting from a nonzero bearing gap. Apparently this can not be a good model, since it only works in differential causality or for nonzero initial gaps. Furthermore, this model can not be accurate since there is no elasticity. However, it is not realistic to have a fluid supply system without elasticity in the tubing or the fluid itself (bulk elasticity). Also the pump will exhibit a pressure dependent leakage flow where fluid flows back from the high pressure side to the low pressure side. This can be confirmed by measuring the flow per revolution of the bearing for different pressures.

If the elasticity of the tubing is being included in the model a simulation of the model can be run in all integral causality. The elasticity of the tubing can be estimated as follows:

$$0 = 2\sigma t + pD \Rightarrow \sigma = \frac{-pD}{2t} \tag{3.6-5}$$

$$\sigma = \frac{\varepsilon}{E} = -\frac{pD}{2tE} \tag{3.6-6}$$

$$\Delta D = \varepsilon D = -\frac{pD^2}{2tE} \tag{3.6-7}$$

$$\Delta V = L\pi\left(\frac{(D+\Delta D)^2}{4} - \frac{D^2}{4}\right) = \frac{L\pi}{4}\left(2D + \frac{D^2 p}{2tE}\right)\frac{D^2 p}{2tE} \tag{3.6-8}$$

after linearization at $\Delta V = 0$

$$p = \frac{2tE}{D^3}\Delta V \tag{3.6-9}$$

$$k_t = \frac{2tE}{D^3} \tag{3.6-10}$$

D – inner diameter of tubing

p – pocket pressure

t – thickness of tubing

ΔV – volume change

σ – normal stress in tubing

E – young's modulus

ε – strain

With the elasticity of the tubing included the behavior of the bearing can be described by:

$$\frac{\partial^2 h}{\partial t^2} = \frac{pA_{eff} - W - F_b}{m} \tag{3.6-11}$$

$$Q_{in} = Q_t + A\frac{\partial h}{\partial t} + Q_{out} + Q_{leak} \tag{3.6-12}$$

$$Q_{out} = \frac{p}{R_{out}} \tag{3.6-13}$$

$$Q_{leak} = \frac{p}{R_{leak}} \tag{3.6-14}$$

$$p = k_t \int Q_t dt + p_0 \tag{3.6-15}$$

F_b – damping force

A – area under bearing pocket (slightly bigger than A_{eff})

m – supported mass

Q_{in} – flow into the bearing pocket

Q_{out} – flow out of the bearing pocket through the bearing gap

Q_t – flow that expands the tubing

Q_{leak} – leakage flow that does not pass through the bearing gap

In order to achieve a model that can simulate the lift-off of the bearing the support has to be included in the model. This can be done by an activated junction structure.

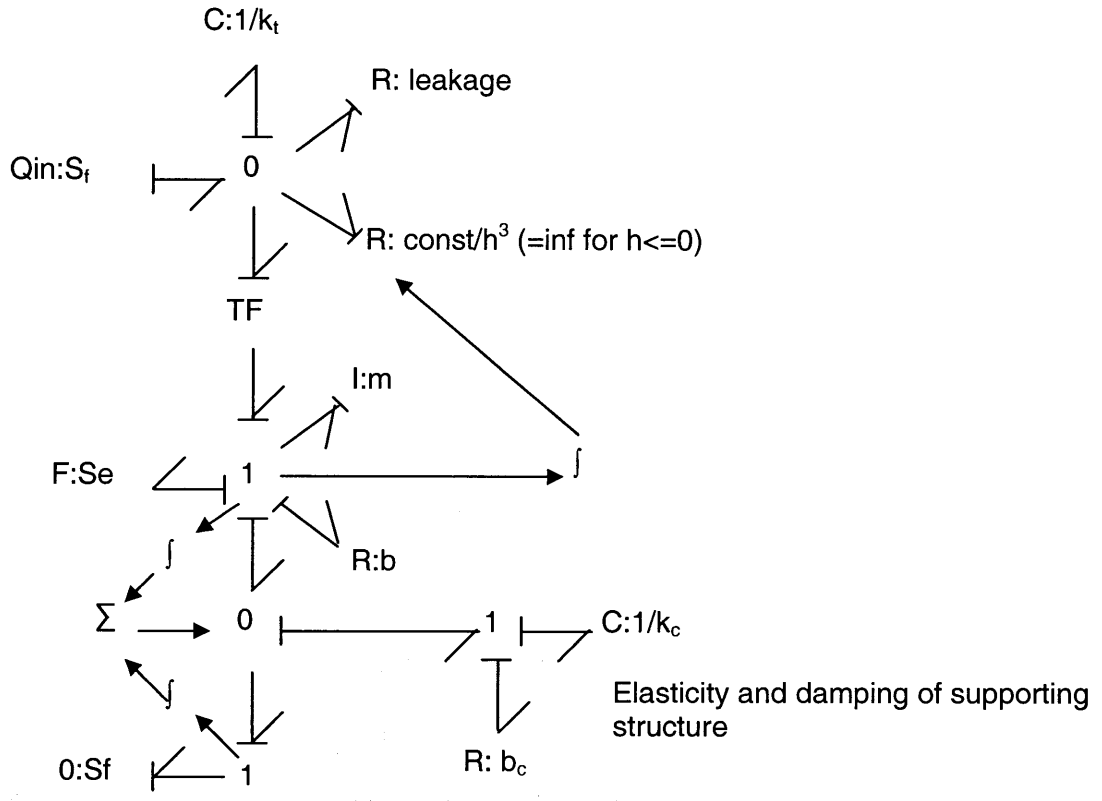

Figure 16: Complete Model of a single pocket hydrostatic bearing

Lastly, to achieve a complete model of a hydrostatic bearing the motor dynamics of the pump have to be included.

3.7 Feedback Control of Hydrostatic Bearings

The basic thought of infinite stiffness control is to make the flow out of the bearing proportional to the pressure in the bearing pocket and thus maintain an ideally constant outflow resistance. As the resistance is inversely proportional to the gap cubed a constant outflow resistance of the pocket is equivalent to a constant gap. Therefore the bearing gap can either be controlled by direct gap measurement or indirectly via the outflow resistance by measuring the bearing flow and pressure. In both cases the pump

speed / bearing flow is adjusted such that a desired bearing gap is maintained or achieved independently of the bearing load.

3.7.1 Increased Hydrostatic Bearing Stiffness through Model Based Pressure Feedback Control

In order to determine the outflow resistance both flow and pressure have to be measured. In the static case, when the gap is not changing, this can be done based on the pump speed and a pressure sensor downstream of the pump as well as an accurate pump model. If the dynamics of the bearing are neglected, a constant gap can be maintained by simply increasing the flow proportional to the pressure change. The proportionality constant in this case is the desired outflow resistance.

$$Q_{out}\frac{\gamma}{h^3} = p \tag{3.7.1-1}$$

$$\frac{\partial Q_{out}}{\partial t}\frac{\gamma}{h^3} - 3Q_{out}\frac{\gamma}{h^4}\frac{\partial h}{\partial t} = \frac{\partial p}{\partial t} \tag{3.7.1-2}$$

$$if\ \frac{\partial h}{\partial t} = 0, h = h_0, R_0 = \frac{\gamma}{h_0{}^3} \tag{3.7.1-3}$$

$$\frac{\partial Q_{out}}{\partial t}R_0 = \frac{\partial p}{\partial t} \tag{3.7.1-4}$$

$$and\ thus:\ Q_{out} = \frac{\Delta p}{R_0} \tag{3.7.1-5}$$

In the case of dynamic load changes the flow produced by the pump is not anymore equal to the flow out of the bearing. Some flow gets stored in the expansion of the tubing or in the bearing itself, as it moves to another height i.e. bearing gap. Even though the control law presented above will still work, it will not be ideal to control dynamic load

changes. The bearing gap can be controlled better by using a model based observer where R_0 is the desired resistance.

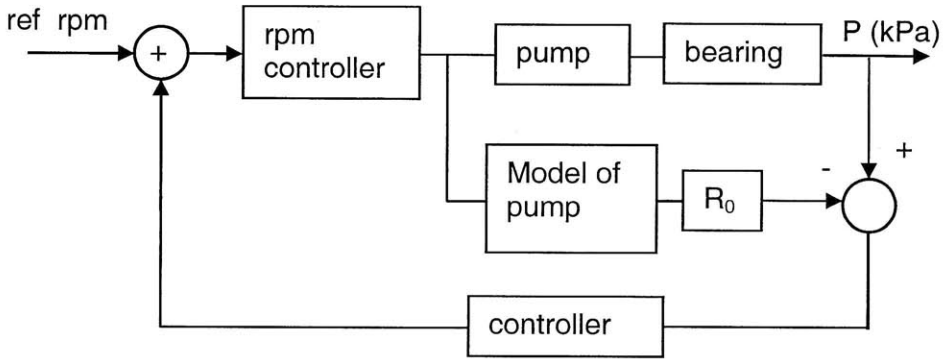

Figure 17: model based pressure feedback control

Figure 18 shows a single pocket thrust bearing test setup that was successfully used as a proof of concept for the proposed pressure control.

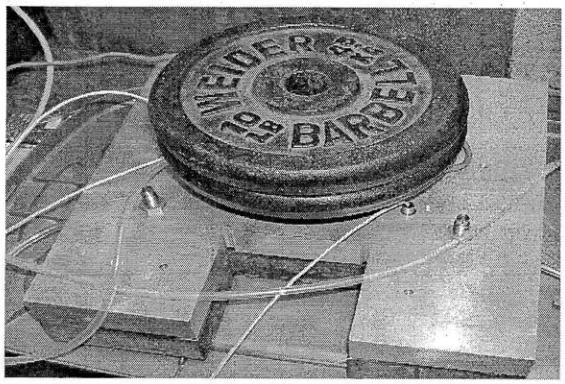

Figure 18: Test setup loaded with 90N

Figure 19, Figure 20 and Figure 21 show the response of the bearing to load changes in open loop and pressure feedback controlled closed loop.

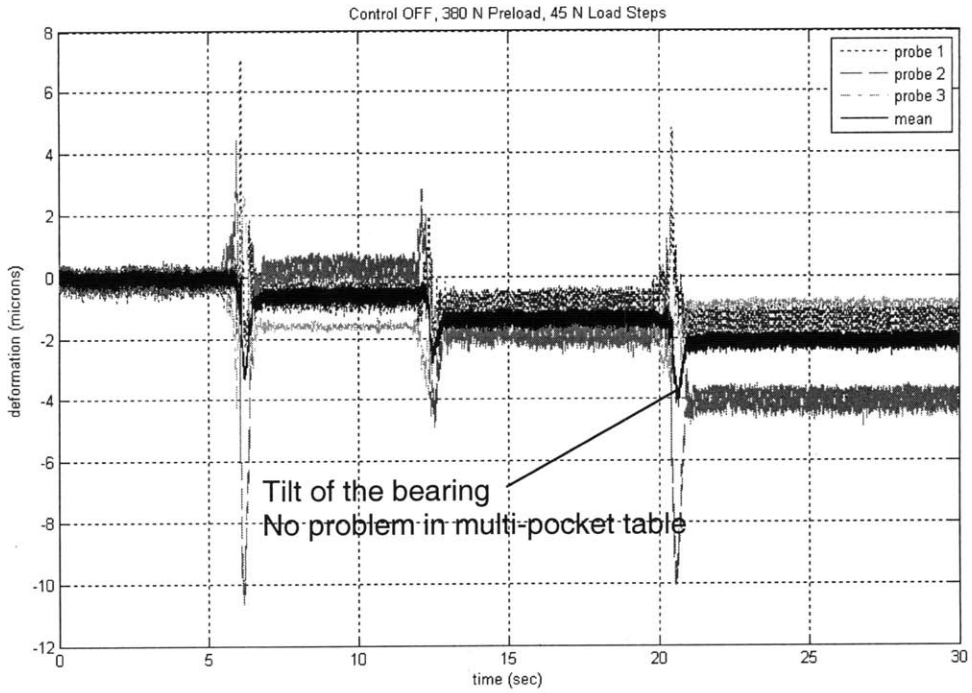

Figure 19: response of the test bearing to 45N load increases

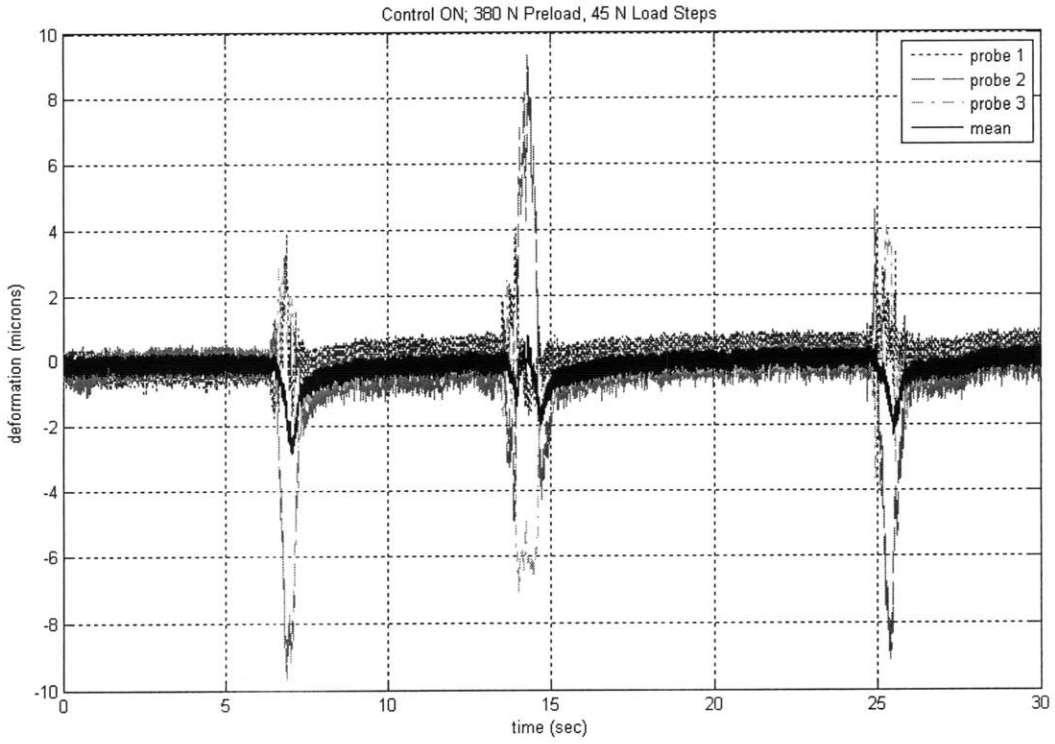

Figure 20: response of the pressure feedback controlled test bearing to 45N load increases

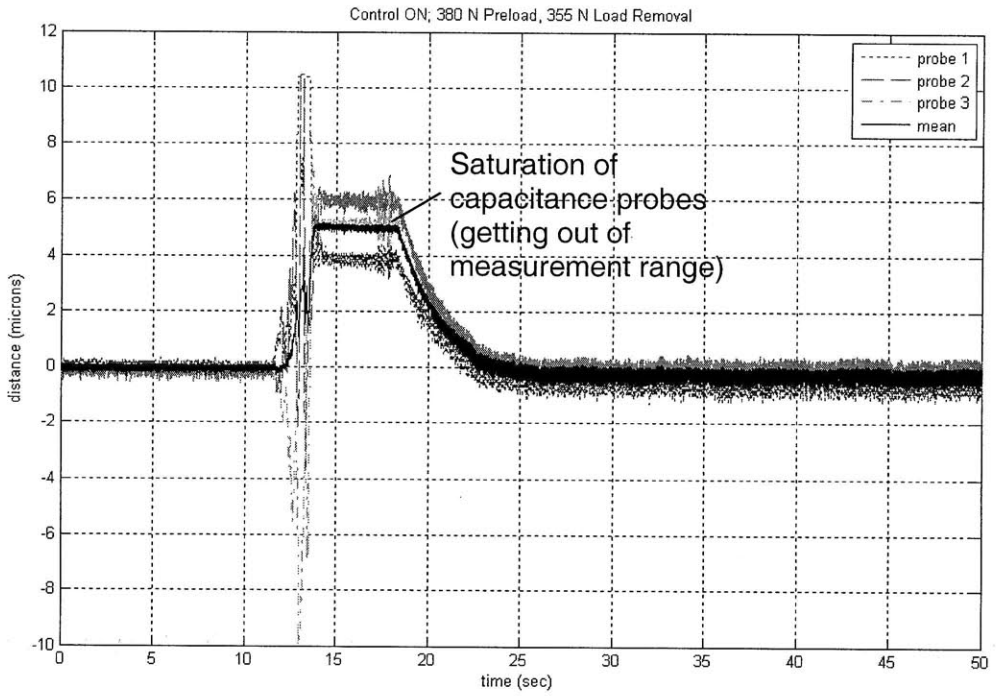

Figure 21: response to the pressure feedback controlled test bearing to a 355N load decrease

The results of the presented experiments can be summarized as follows:

- Predicted Open Loop Stiffness: 83 N/micron
- Actual Open Loop Stiffness: 73 N/micron

With pressure feedback, sensor noise and resolution limits the accuracy of the stiffness measurement:

- Stiffness (worst case from sensor noise): 590 N/micron
- Stiffness (averaging sensor noise): 1200 N/micron

The gap control can significantly increase the stiffness of the bearing and infinite stiffness over a limited pressure range seems to be feasible. Therefore, if the gap is controlled the bearing can be run at a relatively lower nominal gap which results in a higher stiffness independent of the control. Furthermore the gap control can be used in order to adjust the

bearing gap. In the case of a machine tool where a translational carriage is being supported by several hydrostatic bearing pads, the gap control can thus be used to compensate for waviness in the two bearing surfaces.

3.7.2 Increased Hydrostatic Bearing Stiffness through Gap Feedback Control

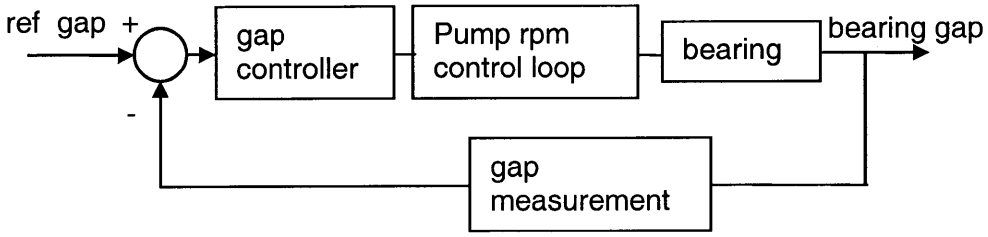

Figure 22: gap feedback algorithm

The bond graph model of Figure 16 illustrates the dynamics between the bearing gap (output) on the one hand and the bearing load as well as supply flow (inputs) on the other hand. The core thought of controlling the bearing gap via direct gap feedback is to measure the gap and change the flow such that a desired gap is achieved and maintained even in the presence of load variations.

Because the outflow resistance of the bearing is inversely proportional to the bearing gap cubed, the bearing's dynamic response to load or flow changes is highly nonlinear. Adding the pressure dependence of the supply flow (leakage and pressure flow characteristic of the supplying pump) as well as the elasticity of the tubing results in a rather complex dynamic system. Local linearization can be used to describe the bearing dynamics around an operating point ($h=h_0$). However care must be taken, as will be shown in the following paragraphs.

$$h^3 = \frac{Q_{out}\gamma}{p} \tag{3.7.2-1}$$

$$Q_{out} = Q_{in} - \frac{p}{R_l} - s\frac{p}{k_t} - Ash \tag{3.7.2-2}$$

$$pA_{eff} + F = ms^2h + bsh \tag{3.7.2-3}$$

$$h^3 = \frac{Q_{in} - \frac{p}{R_l} - s\frac{p}{k_t} - Ash}{p}\gamma \tag{3.7.2-4}$$

$$\frac{m}{k_t A_{eff}}s^3h + (\frac{m}{A_{eff}R_l} + \frac{b}{k_t A_{eff}} + \frac{m}{A_{eff}}\frac{h^3}{\gamma})s^2h + (\frac{b}{A_{eff}R_l} + A + \frac{b}{A_{eff}}\frac{h^3}{\gamma})sh \tag{3.7.2-5}$$
$$= Q_{in} + (\frac{1}{A_{eff}R_l} + \frac{h^3}{A_{eff}\gamma} + \frac{1}{A_{eff}k_t}s)F$$

if F=constant

$$\frac{m}{k_t A_{eff}}s^3h + (\frac{m}{A_{eff}R_l} + \frac{b}{k_t A_{eff}} + \frac{m}{A_{eff}}\frac{h^3}{\gamma})s^2h + (\frac{b}{A_{eff}R_l} + A + \frac{b}{A_{eff}}\frac{h^3}{\gamma})sh \tag{3.7.2-6}$$
$$-(\frac{1}{A_{eff}R_l} + \frac{h^3}{A_{eff}\gamma})F = Q_{in}$$

if Q_{in}=constant, $k_t = \infty$ and $R_1 = \infty$

$$ms^2h + (A+b)sh = Q_{in}\frac{A_{eff}\gamma}{h^3} + F \tag{3.7.2-7}$$

$$\text{linearize } Q_{in}\frac{A_{eff}\gamma}{h^3} \rightarrow 4F_0 - Q_{in}\frac{3A_{eff}\gamma}{h_0{}^4}h = 2F_0 - \frac{3F_0}{h_0}h \tag{3.7.2-8}$$

$$ms^2h + (A+b)sh + \frac{3F_0}{h_0}h = F + 2F_0 \tag{3.7.2-9}$$

Eqn. (3.7.2-9) describes the bearing as a single input, second order system. Consequently the flow input got lost in the linearization. Furthermore the bearing appears to be able to oscillate if the damping was sufficiently low. However, the only energy

storing element in the real physical system is the mass and hence oscillation without another energy storing element (e.g. elastic tubing) seems counter-intuitive. The outflow resistance appears as a spring in the linearized system, but in reality it is an energy dissipater.

Based on the nonlinear eqn. (3.7.2-5) and (3.7.2-6) the bearing's response to flow changes appears similar to a linear third order system. With infinitely stiff tubing ($k_t \rightarrow \infty$) the nonlinear "pseudo third order system" becomes a nonlinear "pseudo second order system".

It appears that even with infinitely stiff tubing, the bearing might be able to oscillate, but never go unstable or limit cycle. Again - if the tubing is infinitely stiff - there is only be one energy storing element and hence oscillation seems counter-intuitive. With finitely stiff tubing another energy storing element is added and the bearing might even become unstable (e.g. low tubing stiffness, high mass, low squeeze film damping and high leakage resistance).

A low leakage resistance, nominal gap and bearing area, paired with a high supported mass (inertia) and high required flow, describe a bearing that is extremely sensitive to load or flow changes. Through simulation of the nonlinear bearing dynamics it could indeed be proven that even under the assumption of infinitely stiff tubing a hydrostatic bearing can oscillate if the supply system is included in the model. Figure 23 shows the corresponding simulink diagram where R_{leak} describes pump internal leakage from the high pressure side back to the low pressure side of the pump. Figure 24, Figure 25 and Figure 26 show the corresponding flow step input, the resulting pressure and gap oscillation.

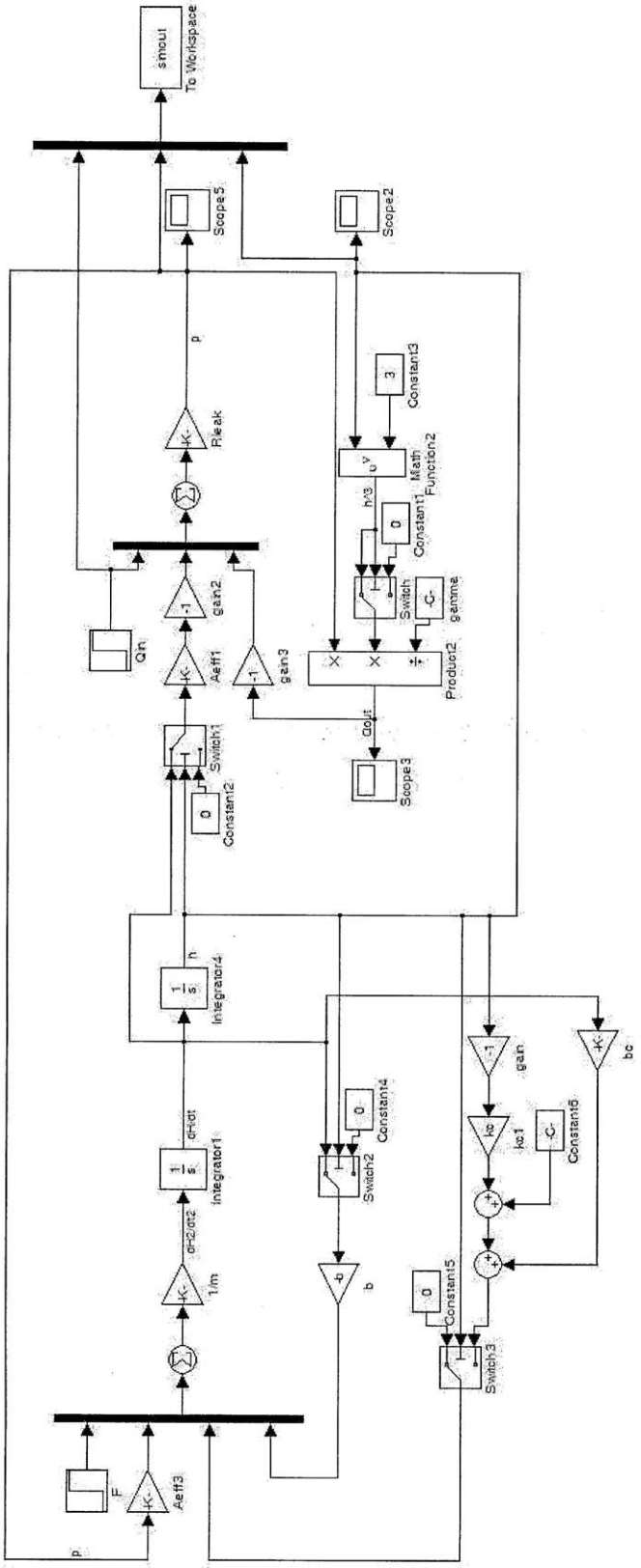

Figure 23: simulink model of hydrostatic bearing including pump internal leakage (backflow)

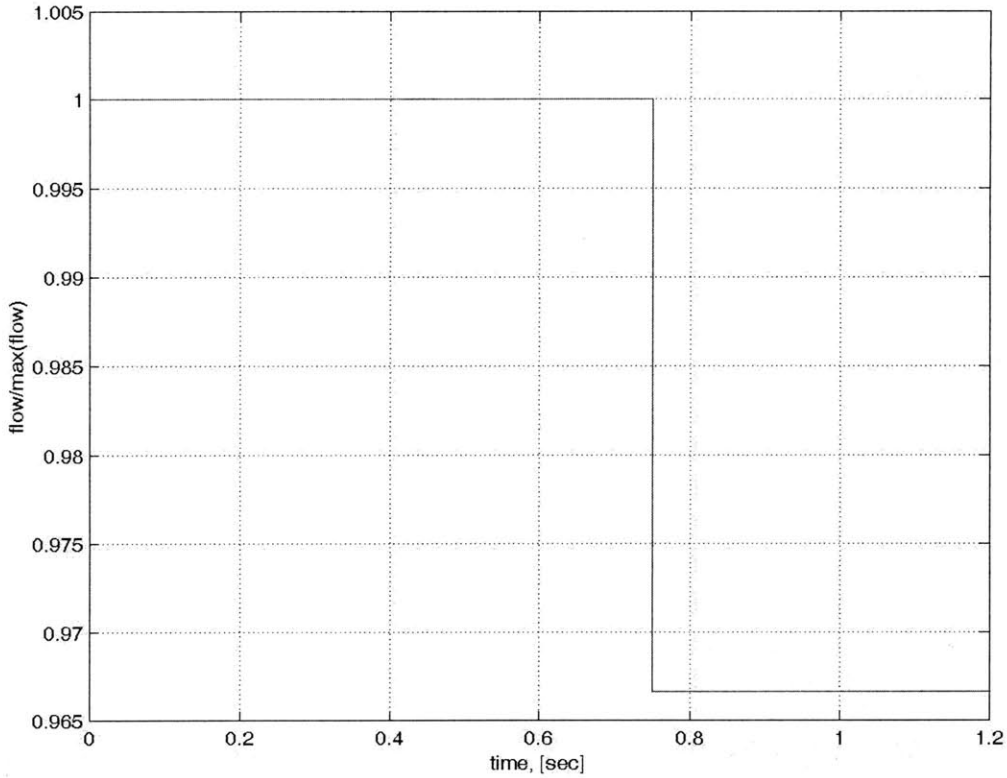

Figure 24: flow, double step input

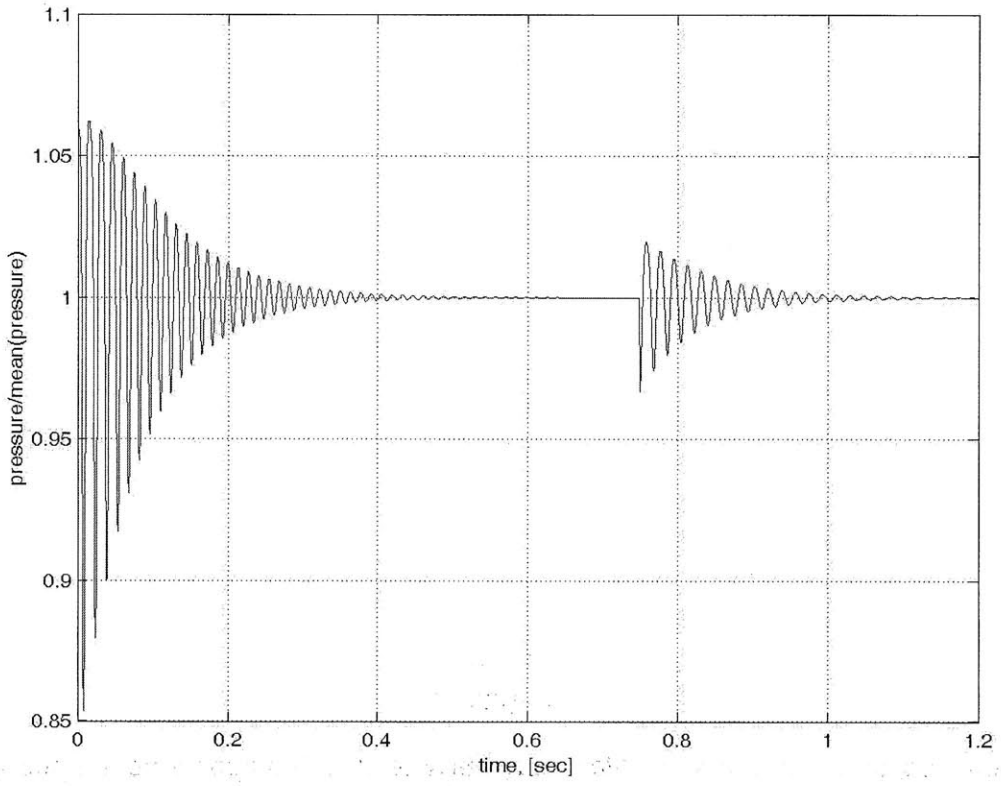

Figure 25: resulting pressure fluctuation of bearing with pump internal leakage

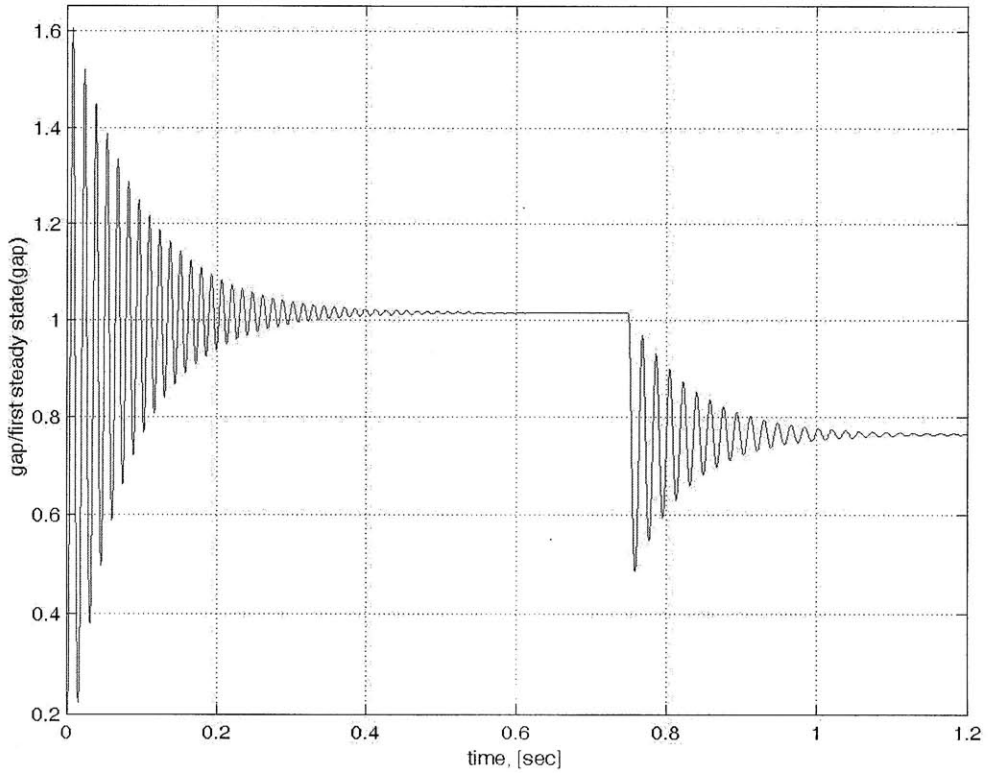

Figure 26: resulting gap fluctuation of bearing with pump internal leakage

If the tubing is of a finite stiffness the bearing system obtains a second energy storage and consequently it is intuitive for the bearing to oscillate depending on the tubing stiffness and system damping. Figure 27 shows the simulink model of the bearing including pump internal leakage as well as elastic tubing. Figure 28 and Figure 29 illustrate the pressure and gap oscillation that results of a flow step input as in Figure 24.

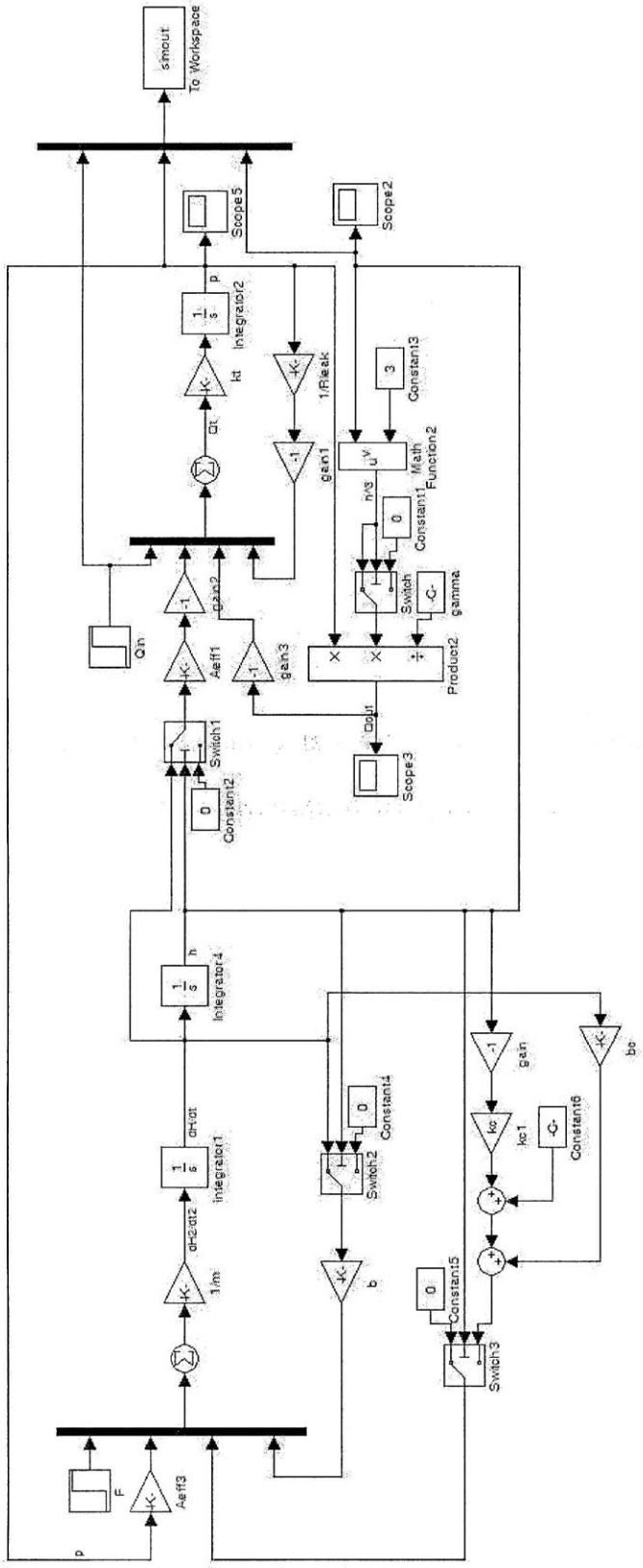

Figure 27: simulink model of hydrostatic bearing including pump internal leakage and elastic tubing

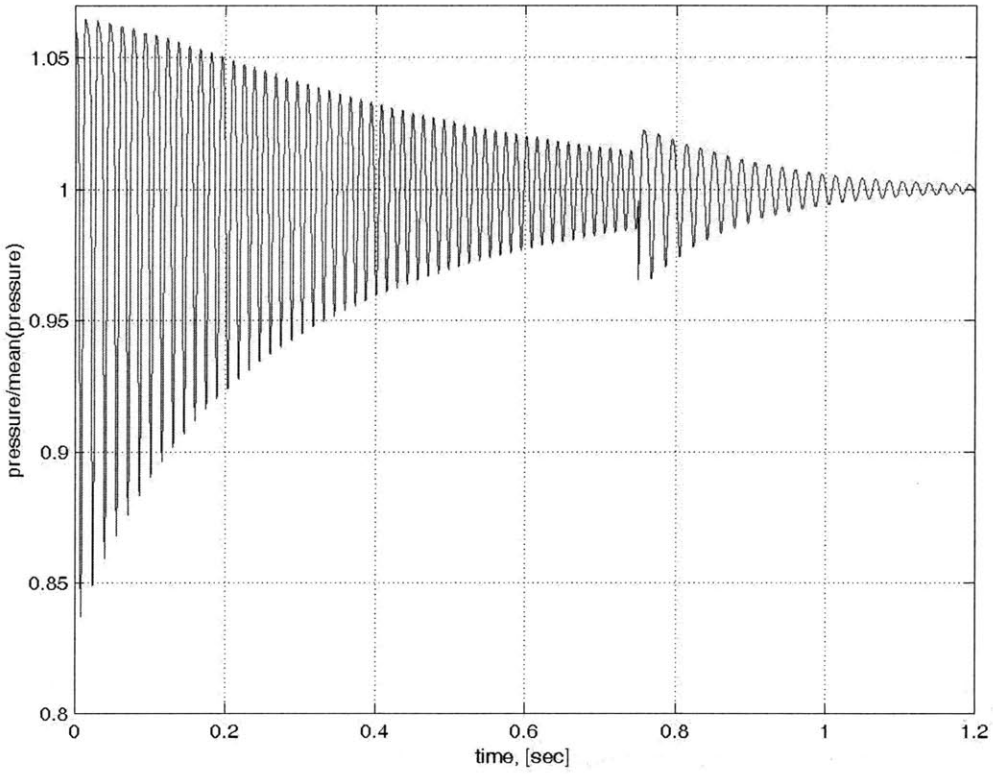

Figure 28: pressure response to flow step, model includes pump internal leakage and elastic tubing

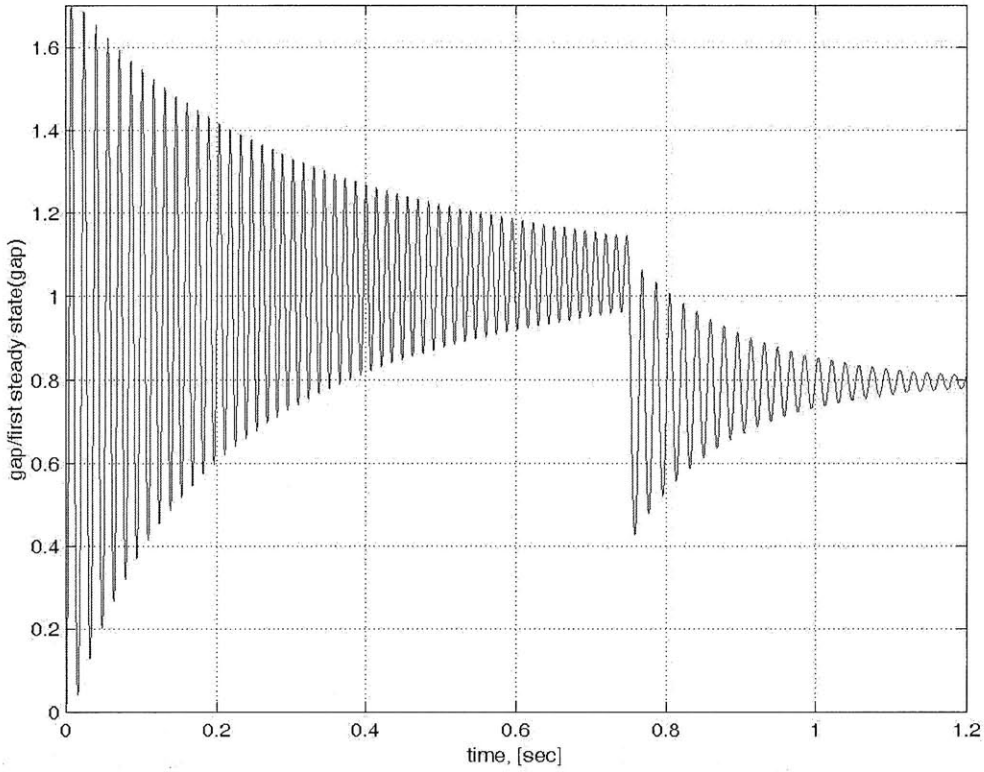

Figure 29: gap response to flow step, model includes pump internal leakage and elastic tubing

With sufficiently soft tubing the bearing can even limit cycle (Figure 30 and Figure 31) and in theory go unstable. In practice instability is not possible as long as the bearing gap can never become negative (infinitely stiff supporting structure with infinite damping).

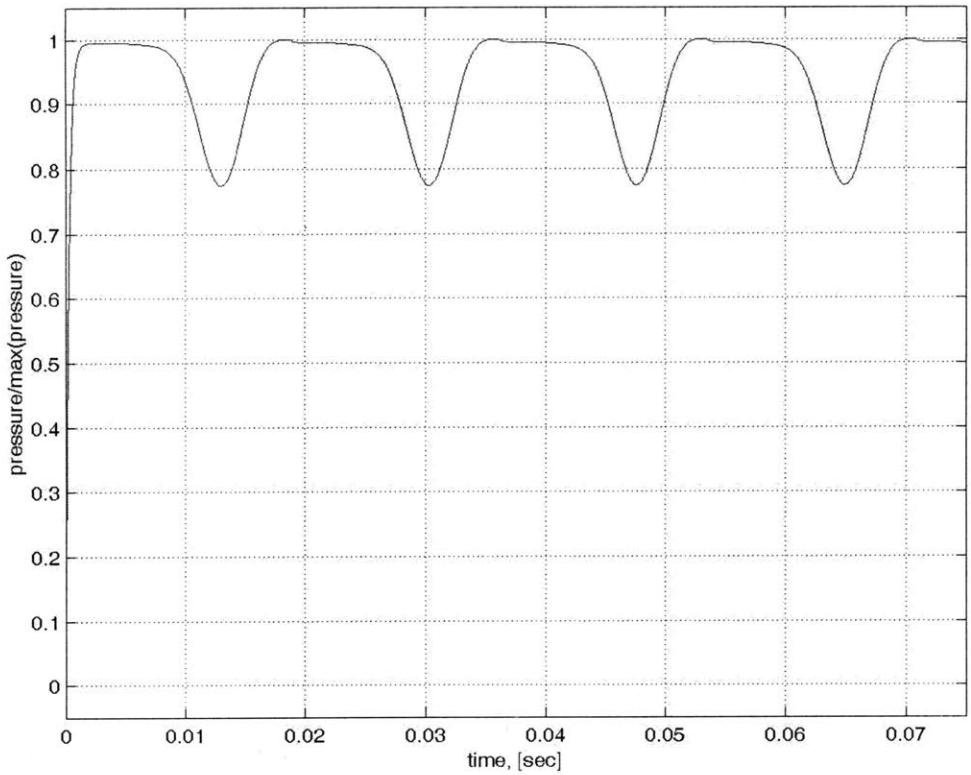

Figure 30: pressure response to flow step, model includes pump internal leakage and soft, elastic tubing

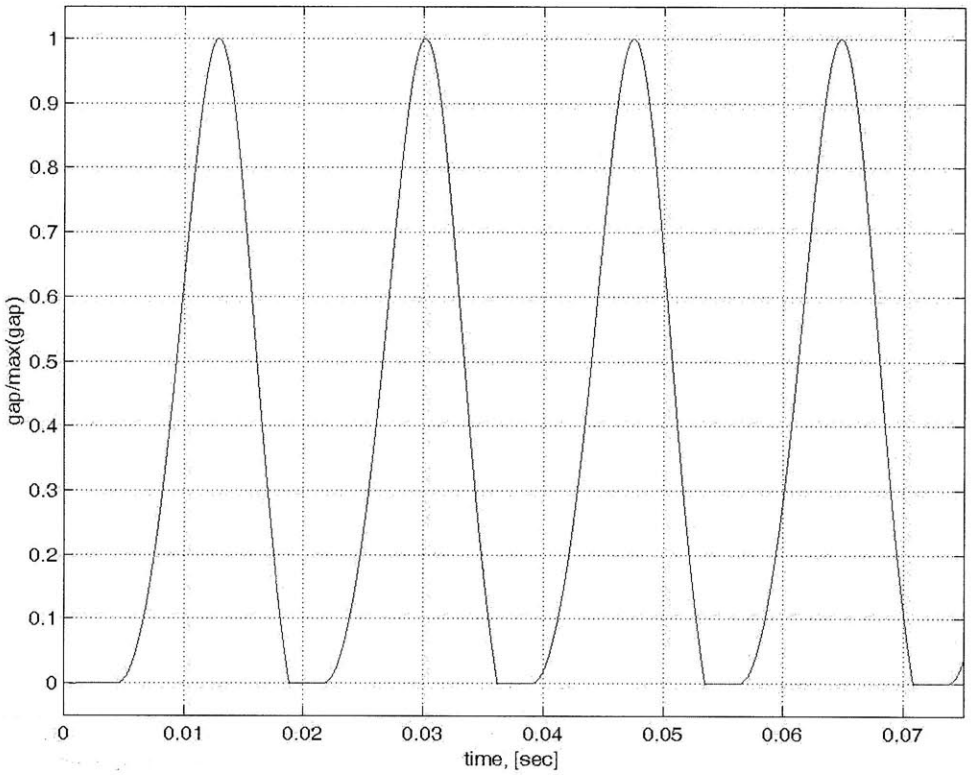

Figure 31: gap response to flow step, model includes pump internal leakage and soft, elastic tubing

However, if the supporting structure is not stiff enough and has low damping even instability becomes possible.

Despite its nonlinearity and the previously described potential for oscillation most appropriately designed hydrostatic bearings are over-damped and can, depending on the used pump and the pump dynamics, easily be controlled by a simple PI controller.

Chapter 4 presents the results of gap feedback in the context of a magnetically preloaded, direct supply, multi-pocket water hydrostatic thrust bearing. With the given bearing and supply system gap feedback enabled a control bandwidth of 10Hz. The major limiting factor in the control of this test bearing was the relatively cheap supply

system (high pump internal leakage). Chapter 3.4 presents a pump design that should overcome this limitation.

4 A Magnetically Preloaded, Direct Supply, Multi-Pocket Water-Hydrostatic Thrust Bearing

450mm silicon wafer grinding requires extremely stiff thrust bearings in the wheel spindle as well as the work spindle. To achieve a machine loop stiffness of 1kN/µm, the axial stiffness of every component must be well beyond 1kN/µm. Figure 7 suggests 3 to 4kN/µm for the work spindle thrust bearings. In order to achieve this stiffness at a bearing gap of ≥10µm either a minimum preload of 10kN or feedback control of the bearing gap is needed. Chapter 3.5 discusses different preload options. For space and cost reasons a combination of up to 4500N gravity and 6000N magnetic preload has been chosen for the presented thrust bearing. To further boost the stiffness to the required level, different feedback control algorithms, as discussed in chapter 3.7 have been tested.

4.1 A Permanent Magnet Preload Assembly

Chapter 3.5 introduced various preload methods for mechanical bearings and other applications. This chapter describes a permanent magnet assembly to preload rotating machine parts (e.g. a hydrostatic bearing) without mechanical contact. The presented magnetic preload device has been designed in cooperation with Professor Xiaodong Lu and Irfan Usman from the University of British Columbia.

The device consists of an axis-symmetric permanent magnet ring that has been magnetized in the axial direction and an axis-symmetric flux circuit that includes the preloaded, rotating machine part, Figure 32.

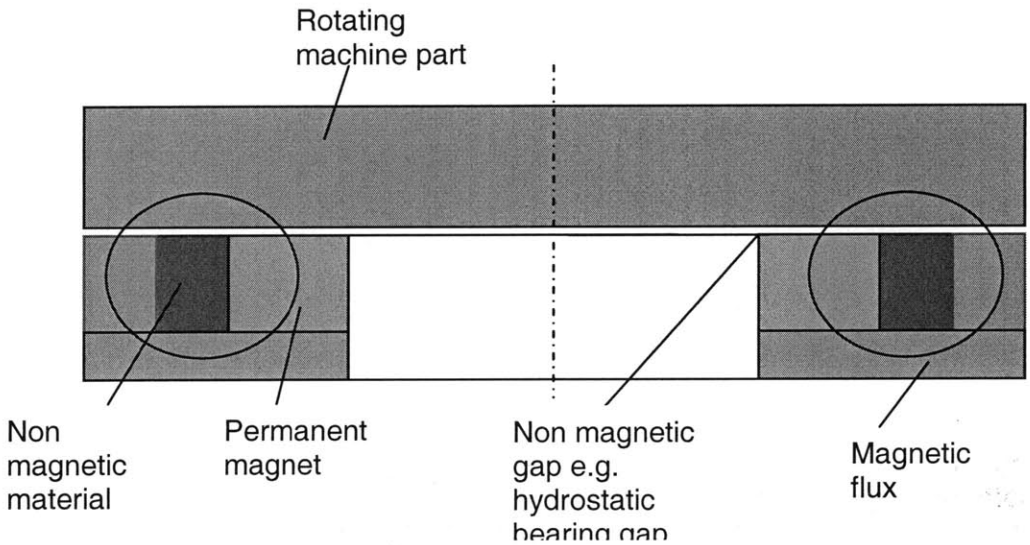

Figure 32: preload magnet assembly with simplified visualization of magnetic flux

The axial symmetry and axial magnetization minimize the flux change in the rotating machine part and therefore theoretically eliminate eddy-currents. Deviations from an ideal axially magnetized, axis symmetric design will create eddy currents. Examples of such deviations are:

- an uneven gap between the rotating machine part and the permanent magnet assembly due to bearing tilt or manufacturing tolerances

- a non-homogeneous, not perfectly axis-symmetric magnetization of the permanent magnet ring.

Eddy currents that are introduced in an area increment ΔA at a distance R from the axis of rotation, due to tilt by an angle Θ of the rotating part relative to the permanent magnet ring, are directly related to the flux change in the area increment:

$$\frac{\partial \phi}{\partial t} = \frac{\partial B}{\partial g}\frac{\partial g}{\partial t}\Delta A \tag{4.1-1}$$

$$\frac{\partial g}{\partial t} = \omega R \sin(\omega t)\sin(\theta) \tag{4.1-2}$$

$$g = g_0 - R\cos(\omega t)\sin(\theta) \tag{4.1-3}$$

Φ – magnetic flux

B – magnetic flux density

g – air gap

ΔA – area increment

ω – rotational speed

Θ – tilt angle

t – time

Consequently for small Θ eddy current generation grows linearly with tilt.

Generally a passive low eddy current, permanent magnet preload minimizes heat generation.

All parts that are within the magnetic circuit are made of soft magnetic materials such as pure iron, low carbon steel (e.g. 1010, 1018, 1020, 1117) or magnetic stainless steel (e.g. AISI 430).

In order to maximize preload high energy density NdFeB magnets have been used for the magnet ring. Figure 33 compares several typical magnet materials.

Magnet material	B_r, [T]	H_{ci}, [kA/m]	$(BH)_{max}$, [kJ/m3]	T_c, [degree C]
$Nd_2Fe_{14}B$ (sintered)	1.0-1.4	750-2000	200-440	310-400
$Nd_2Fe_{14}B$ (bonded)	0.6-0.7	600-1200	60-100	310-400
$SmCo_5$	0.8-1.1	600-2000	120-200	720
Sm(Co, Fe, Cu, $Zr)_7$ (sintered)	0.9-1.15	450-1300	150-240	800
AlNiCo (sintered)	0.6-1.4	275	10-88	700-860
Sr-ferrite (sintered)	0.2-0.4	100-300	10-40	450

Figure 33: magnet material comparison [19]

Ideally the magnet ring is made of one solid piece of magnet material that is magnetized axially and then mounted in the magnet assembly. However, in order to facilitate manufacturing and reduce cost the magnet ring was built of several smaller not magnetized segments. Subsequently this subassembly has been magnetized axially.

In order to prevent corrosion the magnet ring has been galvanized. However in corrosive environments galvanization will not suffice and further measures (non conductive coating, special magnet powder mix) must be taken. Experience has shown that it is highly recommendable to purchase magnets for use in corrosive environments from a technically experienced vendor [20].

Given that most magnetic materials are not very corrosion resistant (e.g. AISI 340) corrosion of all parts in the magnetic circuit in isolation and in combination with other

parts of a different material and thus with a different electro-negativity must be considered.

Figure 34 shows the permanent magnet preload assembly and the used materials.

Item Number	Material	Name
1	Stainless Steel 430	Outer Shield
2	Stainless Steel 430	Reinforcement Ring
3	N44SH	Magnet Ring
4	Stainless Steel 430	Inner Protection Ring

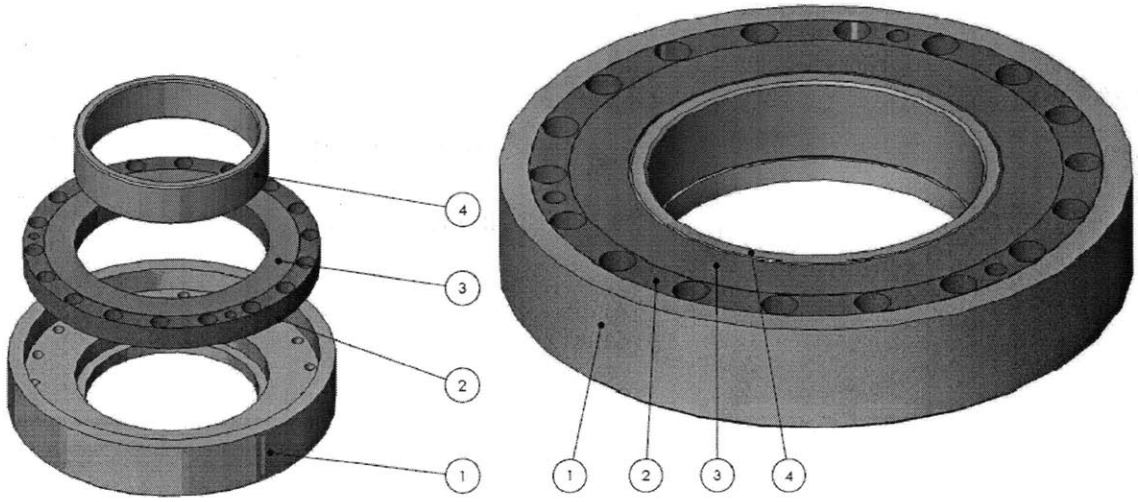

Figure 34: permanent magnet preload assembly

The following analytical model describes how the preload force can be approximately calculated for a core with relative permeability of μr and magnet remanence B_r. B_{g1} and B_{g2} are found via application of Ampere's law along curve c and Gauss' law that requires continuous flux along curve c.

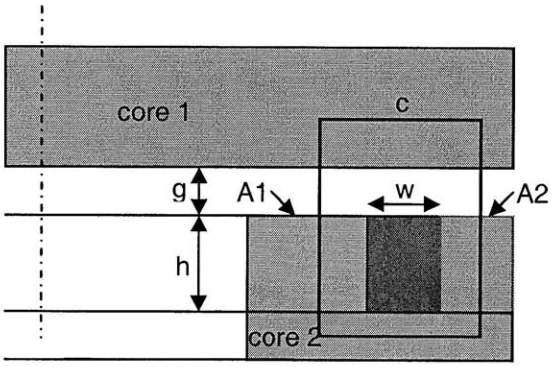

Figure 35: analytical model for preload force estimate

$$H_{g1}(h+g)+H_{c1}L_{c1}+H_{g2}g+H_{c2}(h+L_{c2})=H_m h \tag{4.1-4}$$

$$B_{g1}(h+g)+B_{g1}\frac{A_1}{A_2}g+B_{g1}\frac{A_1}{A_{c1}}\frac{L_{c1}}{\mu_{c1}}+B_{g1}\frac{A_1}{A_{c2}}\frac{h+L_{c2}}{\mu_{c2}}=\frac{B_r}{\mu_r}h \tag{4.1-5}$$

$$\text{assume: } A_1\approx A_{c1}\approx A_{c2};\mu_{c1}\approx\mu_{c2}\approx\mu_r;L_{c1}\approx L_{c2}\approx w \tag{4.1-6}$$

$$B_{g1}=\frac{B_r}{\mu_r}\frac{h}{(g+h+\frac{A_1}{A_2}g+\frac{2w+h}{\mu_r})} \tag{4.1-7}$$

$$B_{g2}=\frac{B_r}{\mu_r}\frac{h}{(g+h+\frac{A_1}{A_2}g+\frac{2w+h}{\mu_r})}\frac{A_1}{A_2} \tag{4.1-8}$$

$$F=\frac{{B_{g1}}^2}{2\mu_0}A_1+\frac{{B_{g2}}^2}{2\mu_0}A_2 \tag{4.1-9}$$

H – field strength

L_c – path length in core material

A – cross sectional area

M – permeability

4.1.1 Hydrostatic Thrust Bearing Experimental Setup

Figure 36: test setup for magnetically and gravity preloaded multi-pocket hydrostatic thrust bearing

Figure 36 shows the thrust bearing test setup that was used to determine the performance of a direct flow supplied, magnetically and gravity preloaded, multi-pocket thrust bearing. The radial bearing consists of a cartridge with two self centering "hydrobushings" as shown in Figure 37 [21].

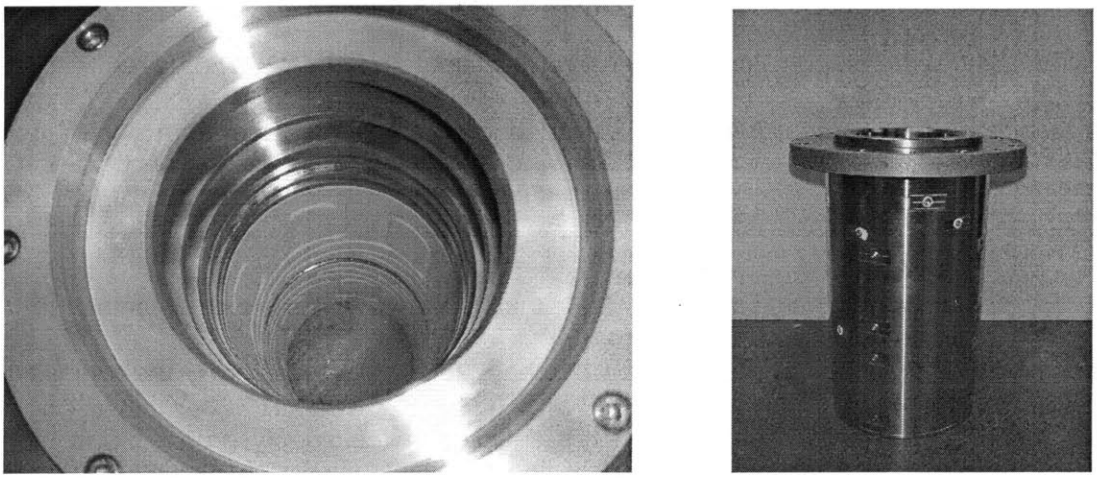

Figure 37: self centering "hydrobushing" cartridge

Each hydrobushing consists of several pockets which are supplied by separate supply grooves that start at a collection groove and spirals over an angle of ideally 180° along the circumference of the bushing to the corresponding pocket.

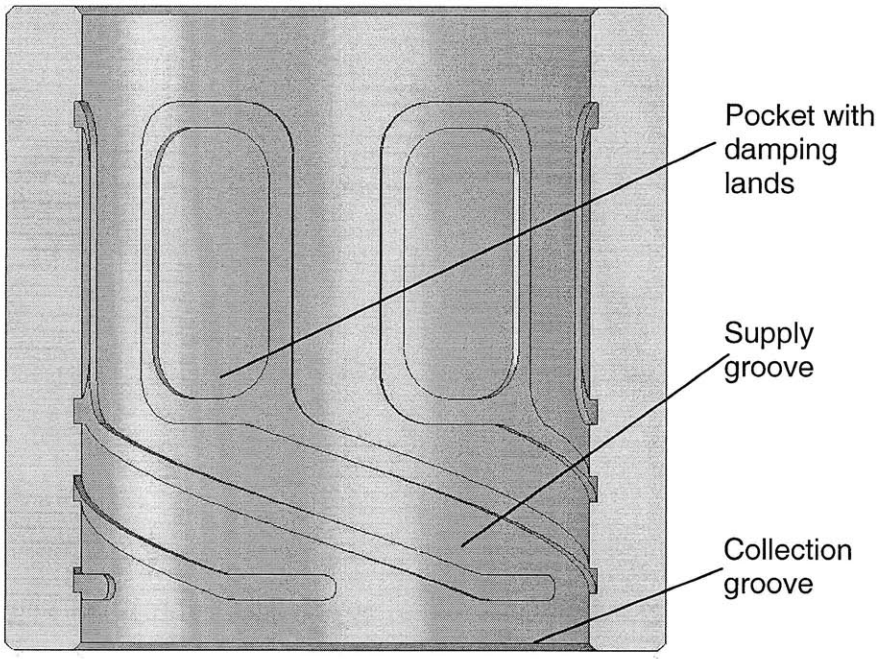

Figure 38: hydrobushing cross section

If the shaft is displaced it automatically narrows the fluid supply to the collection grooves on the bushing side that it displaces to. At the same time it opens up the supply on the other side. Since the supply lines spiral over an angle of ideally 180° around the circumference of the bushing, the pockets that counteract the displacement receive an increased fluid supply (increasing pressure) and a restoring (self-centering) force results.

Figure 39 shows the design spreadsheet that was used for dimensioning the hydrobushings. The efficiency (as defined by real radial stiffness / max. theoretically possible radial stiffness) is dependent on the spacing of the supply grooves and the angle by which they spiral around the circumference of the bushing. Experience has shown that for most bushings efficiencies between 15% and 25% are appropriate. For critical application FEA or a resistance network calculation should be used to more accurately estimate the efficiency.

n			2
diameter	[m,mm]	0.12	120.00
efficiency	%	25.00	
bushing length		0.17	167.00
supply spiral height		0.04	40.00
gap		0.00	15.00
pocket length	Lp	0.11	109.50
Aeff	[m^2, mm^2]	0.01	6880.09
ps	[N/m^2]	1500000.00	
k per bushing	[N/m, N/micron]	516006593.4	516.01
mu	[Nsec/m^2]	0.00089	
land width		0.0175	17.5
l		0.38	
Ro		1.18E+11	
flow per bushing	[m^3/sec, l/min]	1.27643E-05	0.77
Ao		5.65E-06	
u		2.26	
D		0.12	120.00
Al		0.01	
omega		261.80	2500
shear power per bushing	[W]	925.68	
pumping power per bushing	[W]	19.15	
Hp/Hfr		0.02	
radial load capacity per bushing	[N]	4927.5	

Figure 39: hydrobushing design spreadsheet

The axial bearing is built of an eight pocket hydrostatic thrust bearing which is preloaded with about 7.85kN of magnetic and gravity preload. The magnetic preload system is described in 4.1. Figure 40 shows the basic geometry of a rectangular hydrostatic bearing pocket.

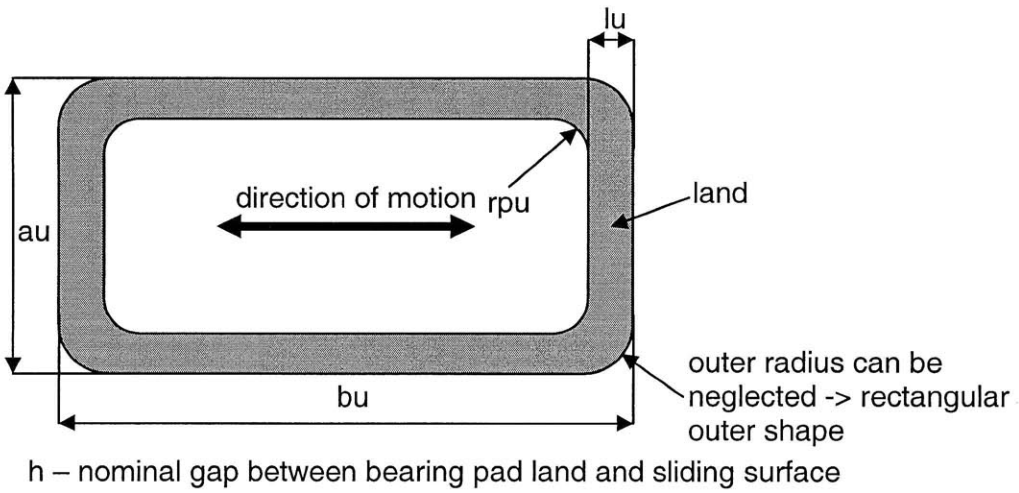

Figure 40: hydrostatic bearing rectangular pocket geometry

The actual, not quite rectangular pocket geometry can be approximated by a roughly equivalent rectangle, Figure 41.

Inputs (N, mm) in BOLD, Outpus in RED					
Bearing pads					
number of pads	n	**8**			
outer diameter of plate	Do(m, mm)	0.50	**496**		
inner pad radius	ri(m, mm)	0.11	**112**		
outer pad radius	ro(m, mm)	0.23	**234.0**		
pocket angle phi	phi(rad, degree)	0.58	**33.0**		
land width	lu (m, mm)	0.01	**14**		
pocket radius	rpu (m, mm)	0.01	**5**		
effective bearing area	Aeffu (mm^2, m^2)	18520	0.018520		
Nominal gap	h (microns, m)	**20**	0.000020		
Gap at maximum load	(microns)	10			
Preload					
Weight	(N)	**950**			
Preload by Magnets	(N)	**6000**			
Total preload force	Fmm(N)	6950.00			
Fluid					
Viscosity mu	(Nsec/m^2)	**0.00089**			
Density rho	(kg/m^3)	**997**			
specific heat	(joule/kgram °C)	**4186**			
apparent bulk modulus of lubricant (here water, approxim	Kla (N/m^2)	**2000000**			
System performance summary					
Stiffness					
Vertical	(N/micron)	1043			
Tilt	(N-m/microrad)				
Load capacity					
Minimum gap, h	(microns)	10			
Vertical	(N)	41569			
Vertical load capacity/pumping power	(N/W)	162752			
Pitch	(N-m)				
Fluid Supply					
Total (n pads) Q	(lpm, m^3/s)	0.327	5.44E-06		
Minimum pressure	(atm, kPa, psi)	0.47	47	7	
Minimum pump power (n pads)	(W)	0.26			
Max pressure	(atm, kPa, psi)	20.73	2,073	300	
Maximum pump power	(W)	11.29			
Maximum velocity (with no pre-feed)					
Avg. flow velocity out of pocket	(m/s)	0.01			
Max. velocity (p at leading edge becomes atmospheric)	(m/s)	34.98			

Figure 41: design spreadsheet for single sided hydrostatic thrust bearings

The bearing gap was measured by three capacitance probes that were mounted over the floating bearing plate via cantilevers as shown in Figure 42.

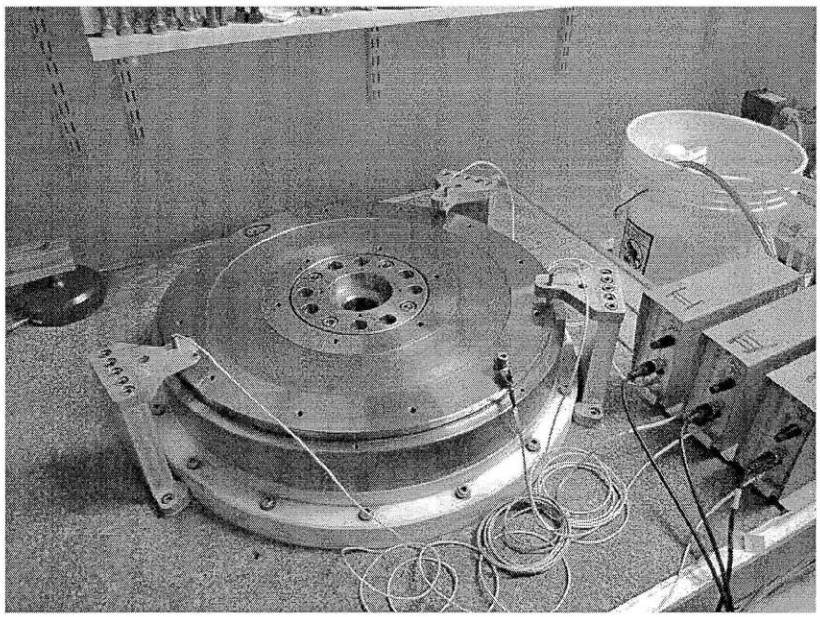

Figure 42: hydrostatic bearing test setup with capacitance probes for bearing gap measurement

Each of the eight thrust bearing pockets is supplied with water by a low cost miniature gear pump as shown in Figure 43.

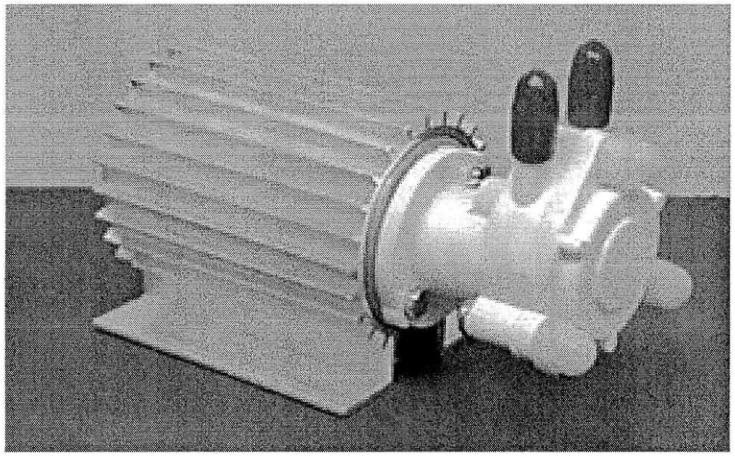

Figure 43: Greylor, low cost miniature gear pump

To accurately predict the stiffness of the bearing the pressure flow characteristics of the pumps need to be taken into account. The pressure flow characteristics of the used gear pump are shown in Figure 44 to Figure 46. The flow of the used gear pump is dependent

on the pressure (Figure 44) as well as on the pump speed (Figure 45). Figure 46 shows the dependence of the flow per revolution on the pressure for different pump speeds.

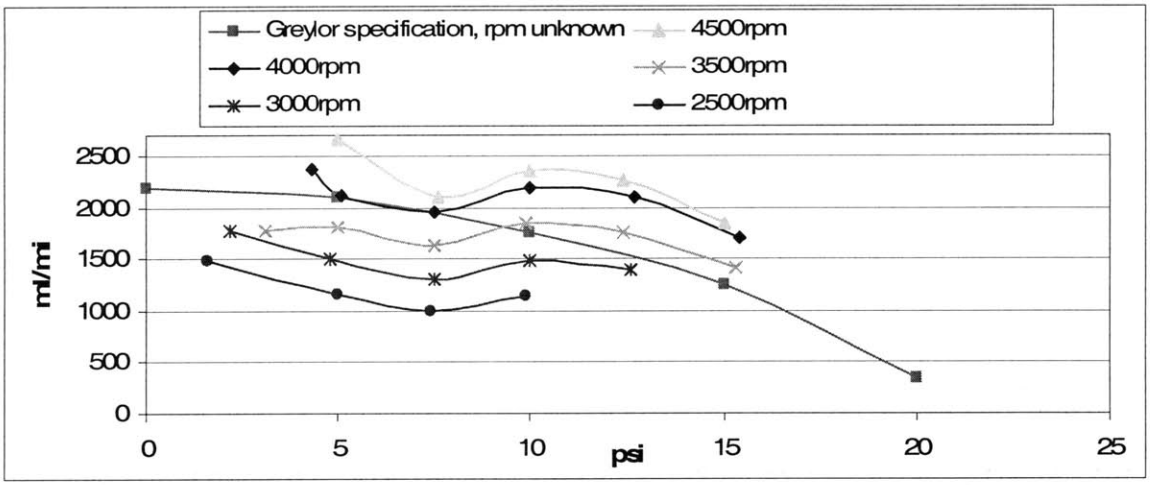

Figure 44: pressure flow dependence of the Greylor gear pump

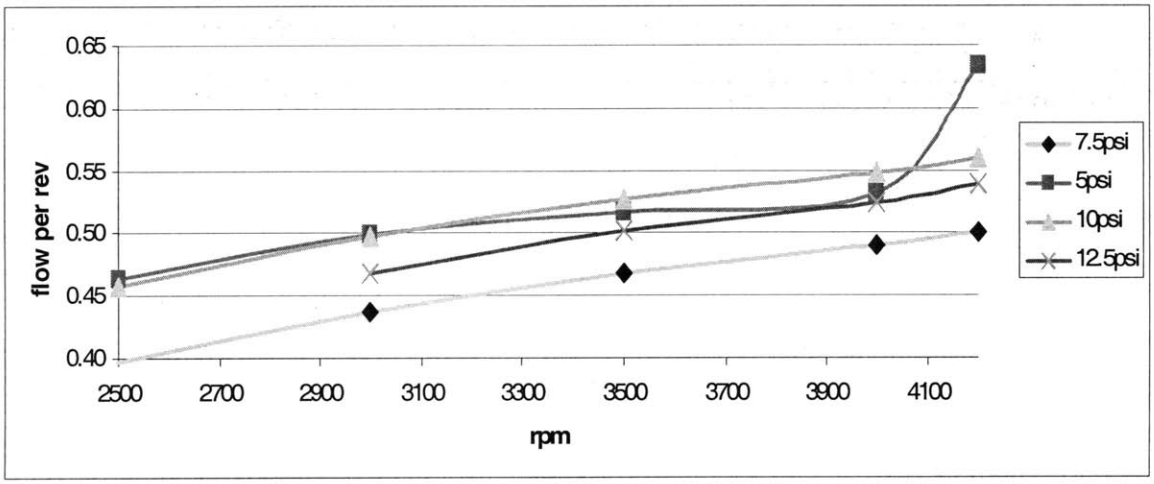

Figure 45: dependence of flow per revolution and pump speed

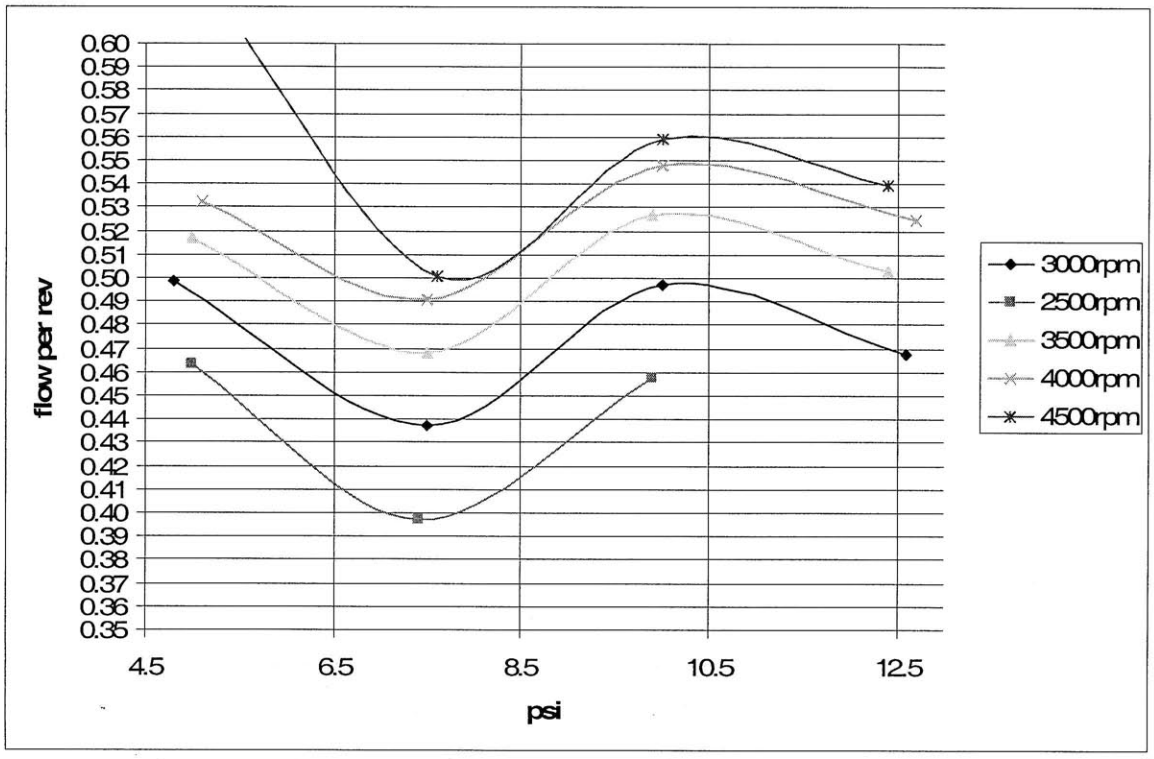

Figure 46: dependence of flow per revolution and pressure

Eqn. (4.1.1-7) describes a linearized, static, analytical model to predict the performance of a hydrostatic bearing.

$$R = \frac{p}{Q_{out}} = \frac{W}{AQ_{out}} \tag{4.1.1-1}$$

$$R = \frac{\gamma}{h^3} \tag{4.1.1-2}$$

$$h = \sqrt[3]{\frac{\gamma A Q_{out}}{W}} \tag{4.1.1-3}$$

$$\frac{\partial h}{\partial W} = \frac{1}{3}\frac{h}{W} \tag{4.1.1-4}$$

$$\frac{\partial h}{\partial Q_{out}} = \frac{1}{3}\frac{h}{Q_{out}} \tag{4.1.1-5}$$

$$h = h_0 + \left.\frac{\partial h}{\partial W}\right|_{W=W_0} \Delta W + \left.\frac{\partial h}{\partial Q_{out}}\right|_{Q_{out}=Q_{out\,0}} \Delta Q_{out} \tag{4.1.1-6}$$

$$h = h_0 + \frac{1}{3}\frac{\Delta W}{W_0}h_0 + \frac{1}{3}\frac{\Delta Q_{out}}{Q_{out\,0}}h_0 \tag{4.1.1-7}$$

The constant flow compliance (1/stiffness) of the bearing is described by the second term on the right side of eqn. (4.1.1-7). The third term describes the reaction of the bearing to flow changes. The static reaction of the bearing is therefore composed of the superposition of the constant flow response of the bearing and the reaction to a load induced flow change based on the pressure flow dependency of the used pumps.

If the bearing load is kept constant, flow change and gap change should be directly related.

$$\frac{Q_{out}}{Q_{out\,0}} = \left(\frac{h}{h_0}\right)^3 \tag{4.1.1-8}$$

Ideally the flow change should equal the change in pump speed which in a closed loop system corresponds to the change in control voltage (speed reference). For a given gap

change, Figure 47 and Figure 48 compare the necessary change in pump speed, the theoretical, expected flow change and the measured flow change. In Figure 47 all eight bearing pockets were in use. To preclude possible coupling effects between neighboring pockets, only four pockets were used in Figure 48 and the two neighbors of each of the four used pockets were shorted to atmospheric pressure. Generally, relatively small changes in pump speed create relatively high changes in flow. However, the measured flow changes were too small to explain the measured gap changes. The measured gap changes were confirmed by various measurements with different sensors (capacitance probes, eddy current probes, dial indicators). The discrepancy between flow change and pump speed change can be explained by the speed dependent flow per revolution of the used gear pumps. Apparently relatively small speed changes can create significantly higher flow changes. The difference between measured and expected flow change for a given gap change can only be explained by a gap offset. I.e. even when the bearing is not operated (pumps are not running) and the measured gap is zero (by definition), the outflow resistance is still finite or in other words there is still an effective bearing gap. Such a bearing gap offset would result if the two bearing surfaces were not sufficiently flat, such that there is an effective bearing gap even when the pumps are not running and the plates are sitting on top of one-another (in direct contact).

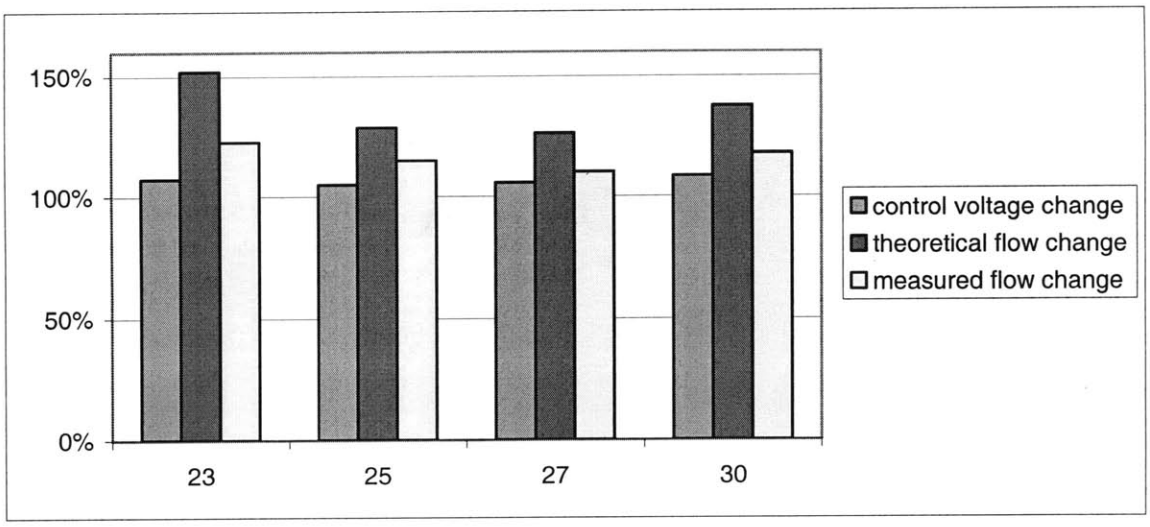

Figure 47: gap and flow change, starting at 20μm, all eight pumps/pockets in use

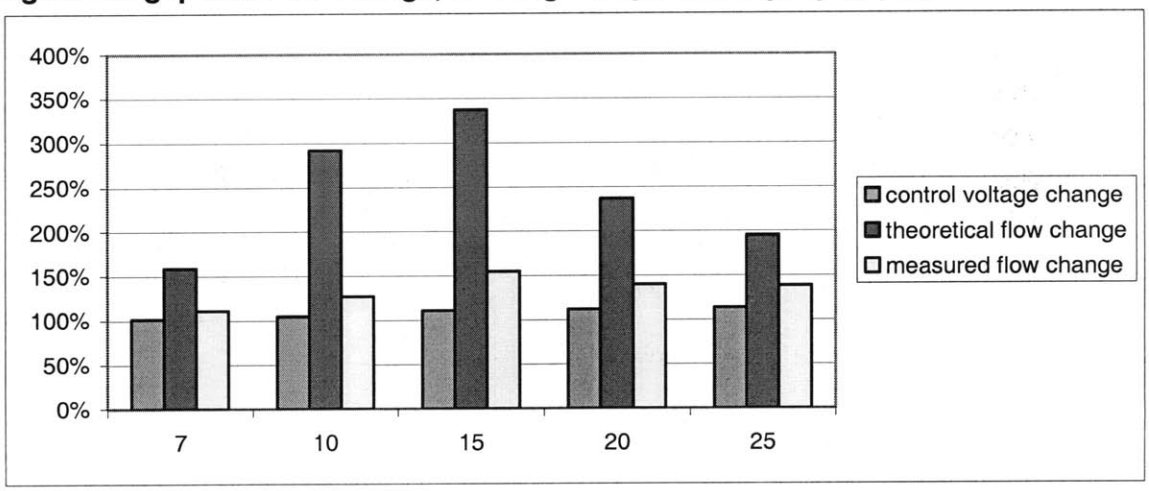

Figure 48: gap and flow change, starting at 6μm, only four pumps/pockets in use, every other pocket was shorted to zero pressure → no interaction between pockets, no coupling

Figure 49 and

Figure 50 depict the same data as Figure 47 and Figure 48 with an additional gap offset of 25μm.

$$\frac{Q_{out}}{Q_{out_0}} = \left(\frac{h+25}{h_0+25}\right)^3 \qquad (4.1.1\text{-}9)$$

With a gap offset of 25μm the measured and predicted flow increases coincide.

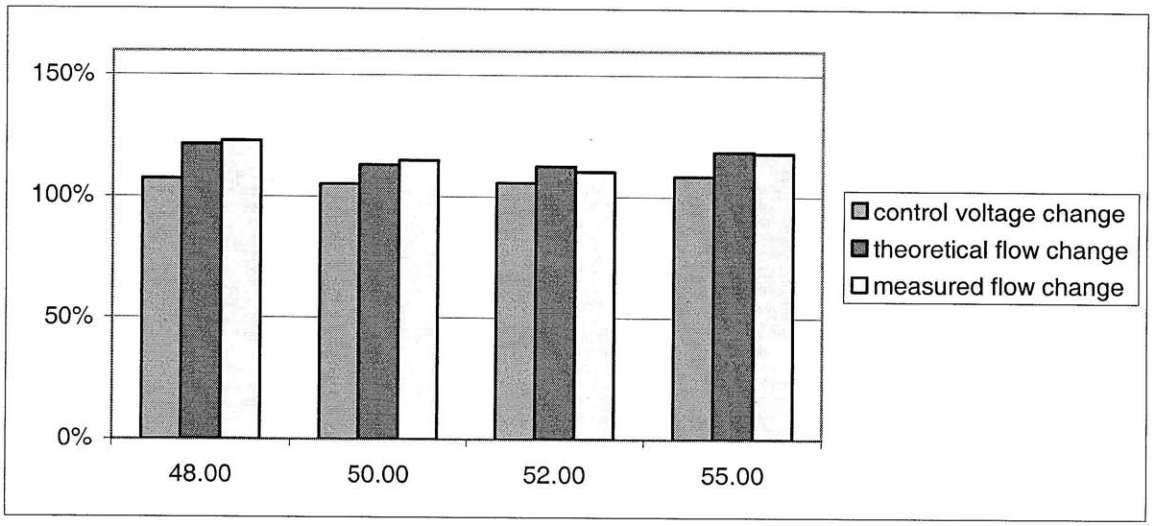

Figure 49: gap and flow change, starting at 20+25=45μm, all eight pumps/pockets in use

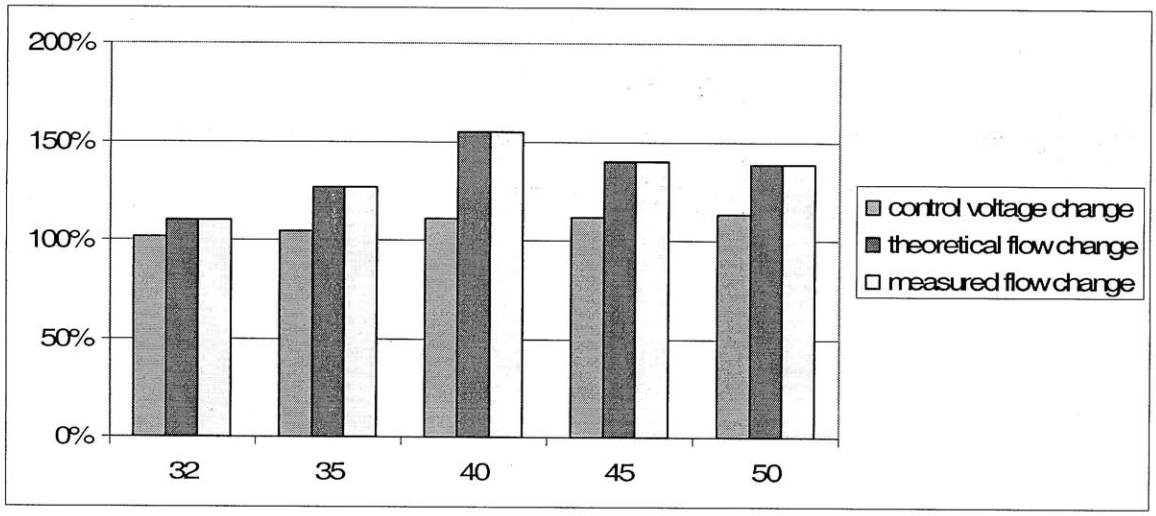

Figure 50: gap and flow change, starting at 6+25=31μm, only four pumps/pockets in use, every other pocket was shorted to zero pressure → no interaction between pockets, no coupling

Figure 51 shows the open loop response to of the hydrostatic thrust bearing four 68N load increases and four load decreases.

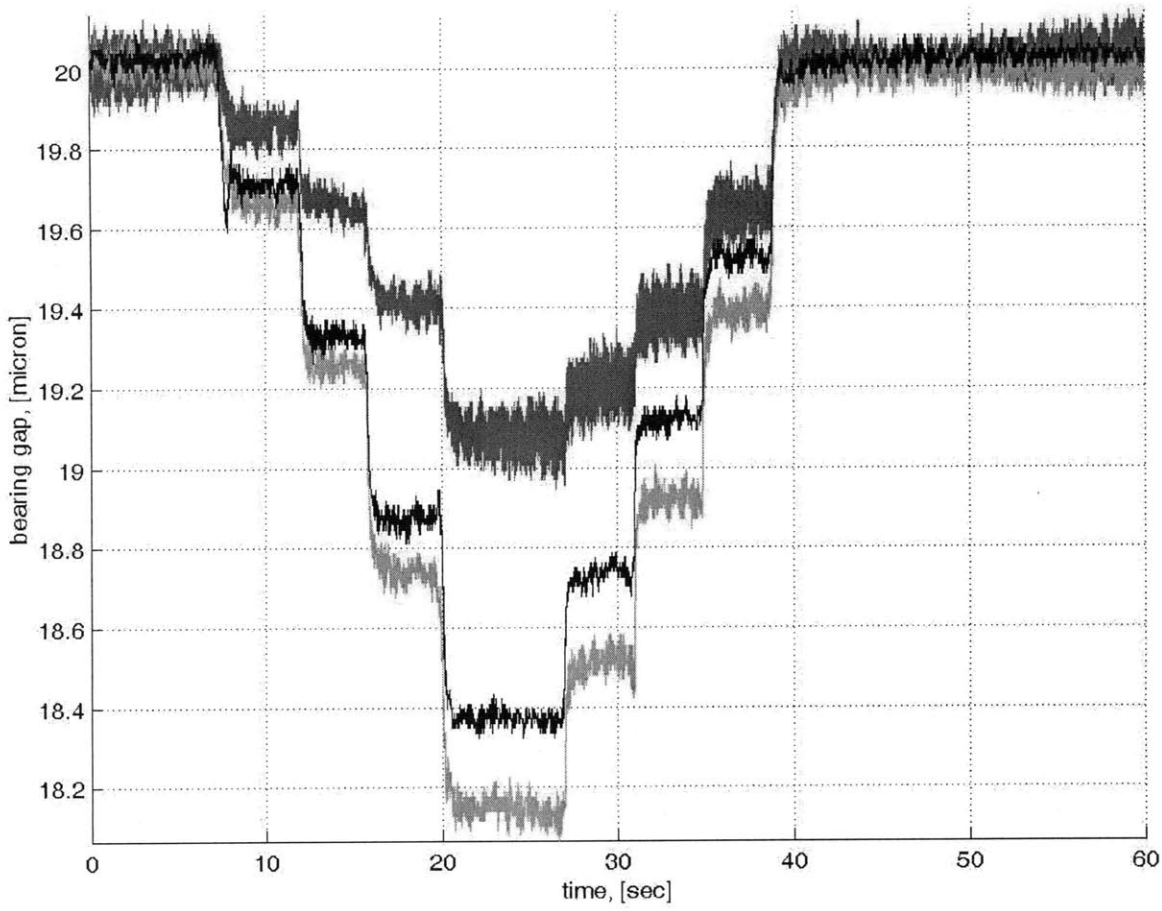

Figure 51: open loop response of eight pocket hydrostatic thrust bearing with 7kN preload to 68N load steps

Due to tilt of the floating bearing plate relative to the stationary part the three probes show a different measured gap. The overall stiffness of the bearing is approximately 200N/μm. The constant flow bearing stiffness at 20μm bearing gap and a preload of 7kN would be expected to be 1.2kN/μm - about five times higher. With 7kN preload and at a bearing gap of 20μm the constant flow compliance of the bearing would cause a displacement of 0.23μm. With an effective bearing area of 0.0185m2 and a load increase of 272N, the remaining 1.07μm correspond to a pressure dependent flow decrease of about 8%/psi. If an a gap offset of 25μm is included in the calculation a load induced flow decrease of 2%/psi would be sufficient to explain the low measured

stiffness. Figure 52 and Figure 53 shows a more detailed model that explains the comparatively low measured stiffness.

A	B	C	D	E	F	G
effect of bearing tilt when the bearing is run in open loop mode is not included in this calculation. However, bearing tilt (as observed in various measurements) might explain the small difference between the theoretical "resulting apparent stiffness" and the measured stiffness						
effective bearing area	[m^2]	0.01852				
measured open loop stiffness						
load increase	[N]	272				
gap change	[micron]	1.3				
stiffness	[N/micron]	209.23				
constant flow stiffness						
preload	[N]	7850				
gap	[micron]	20				
surface tolerance	[micron]	0				
effective gap	[micron]	20				
stiffness	[N/micron]	1177.50				
resulting displacement	[micron]	0.23				
flow stiffness						
remaining displacement	[micron]	1.07				
nominal gap	[micron]	20				
required flow change	[%/Pa]	0.00109%				
required flow change	[%/psi]	8%				

Figure 52: hydrostatic bearing compliance budget with zero gap offset

effect of bearing tilt when the bearing is run in open loop mode is not included in this calculation. However, bearing tilt (as observed in various measurements) might explain the small difference between the theoretical "resulting apparent stiffness" and the measured stiffness		
effective bearing area	[m^2]	**0.01852**
measured open loop stiffness		
load increase	[N]	**272**
gap change	[micron]	**1.3**
stiffness	[N/micron]	209.23
constant flow stiffness		
preload	[N]	**7850**
gap	[micron]	**20**
surface tolerance	[micron]	**25**
effective gap	[micron]	45
stiffness	[N/micron]	523.33
resulting displacement	[micron]	0.52
flow stiffness		
remaining displacement	[micron]	0.78
nominal gap	[micron]	45
required flow change	[%/Pa]	0.00035%
required flow change	[%/psi]	2%

Figure 53: hydrostatic bearing compliance budget with 25μm gap offset

In order to boost the stiffness better pumps (real constant flow), feedback control or both are necessary. Chapter 3.7 introduced model based pressure feedback and direct gap feedback as two strategies to control the bearing gap. Due to the poor pump performance (flow per revolution depends on pump speed as well as pressure) a model based pressure feedback loop could not significantly improve the dynamic performance of the bearing. The main problem was that a sufficiently accurate pump model to estimate the flow based on the pump speed and pocket pressure could not be established. Another problem was that the bearing had more pockets (eight) than necessary (three). Consequently, a balanced bearing could be achieved by infinitely many combinations of pump speeds and pump flows. E.g. all pumps are producing the same flow and support the same load or only three pumps carry the entire load while the

other pumps are not running/producing any pressure. Therefore a controller had to be found that automatically finds a solution that evenly distributes the required pumping power over all eight pumps. Ultimately this could be achieved by adjusting the speed of one pump, based on the pressure in the pocket that is supplied by this pump as well as the pressure of the two neighboring pockets (weighted average control). However, due to the previously mentioned pump performance limitations a sufficiently good dynamic control of the bearing gap in the presence of load changes could not be achieved.

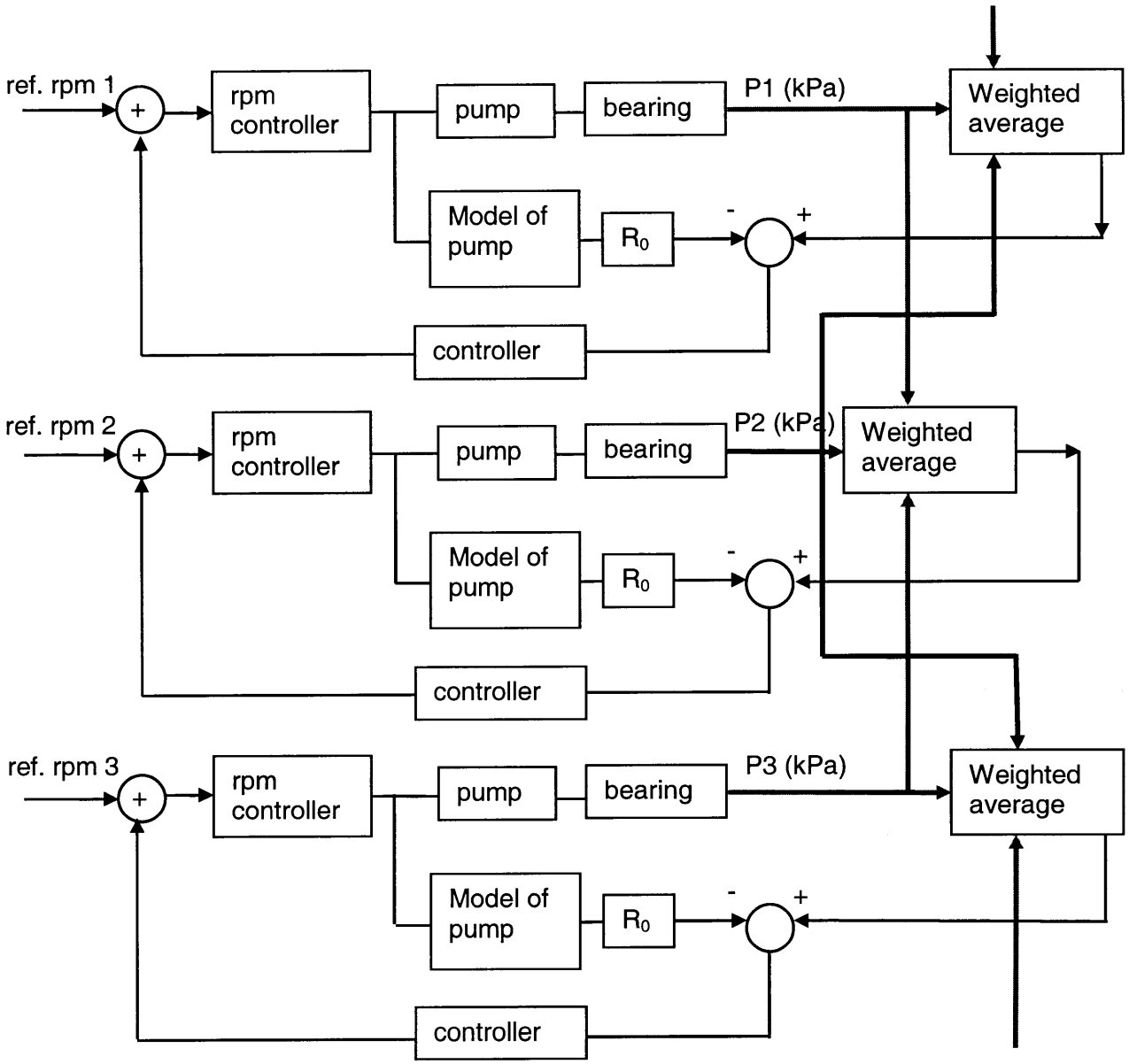

Figure 54: model based pressure feedback control, block diagram

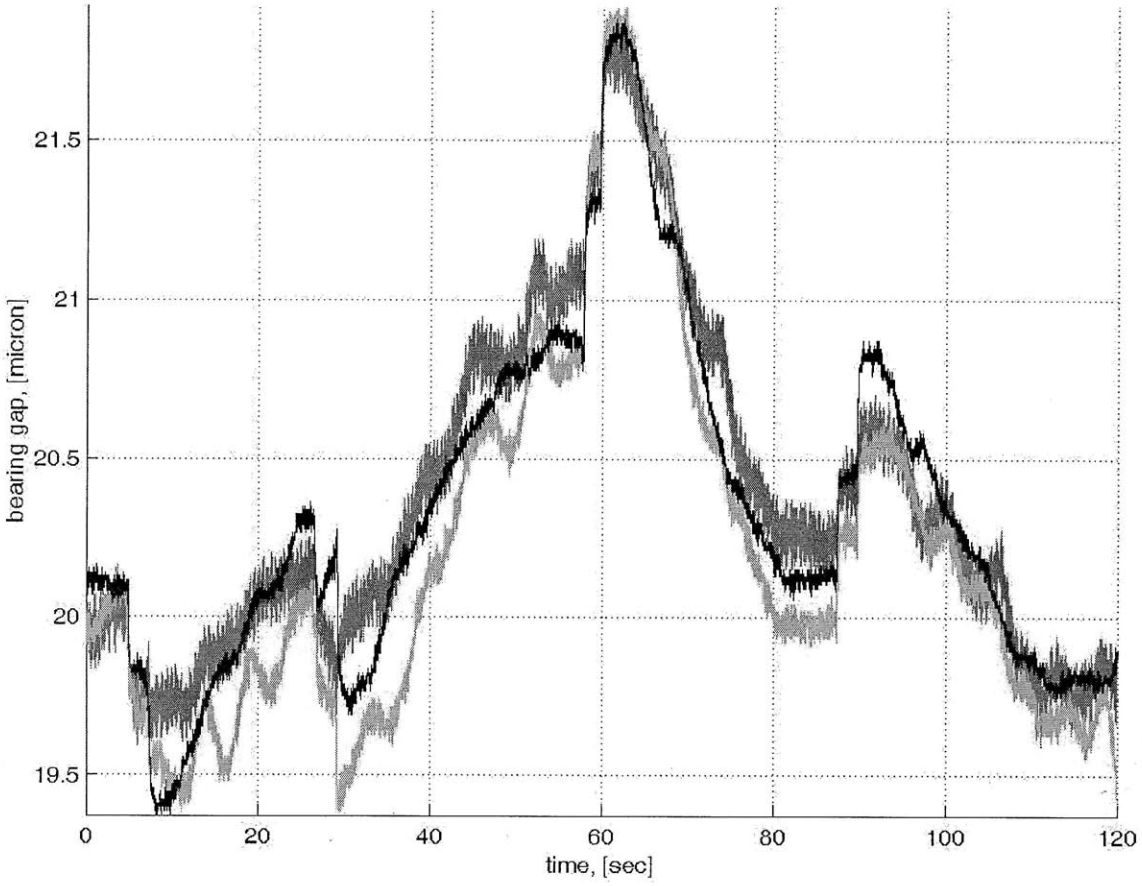

Figure 55: model based pressure feedback control, 68N load steps

Even though pump performance also limits the achievable bandwidth and influences the noise level of a gap feedback controlled bearing, gap feedback does not suffer from model inaccuracies and therefore provides an easy way to increase the static and dynamic stiffness of a hydrostatic bearing. Even though the bearing is a nonlinear dynamic system (see chapter 3.7), its dynamic behavior for small gap changes is roughly linear. Figure 56 shows the open loop response of the hydrostatic thrust bearing with the average velocity reference voltage of all eight pumps as input and the average bearing gap as measured by the three capacitance probes as output.

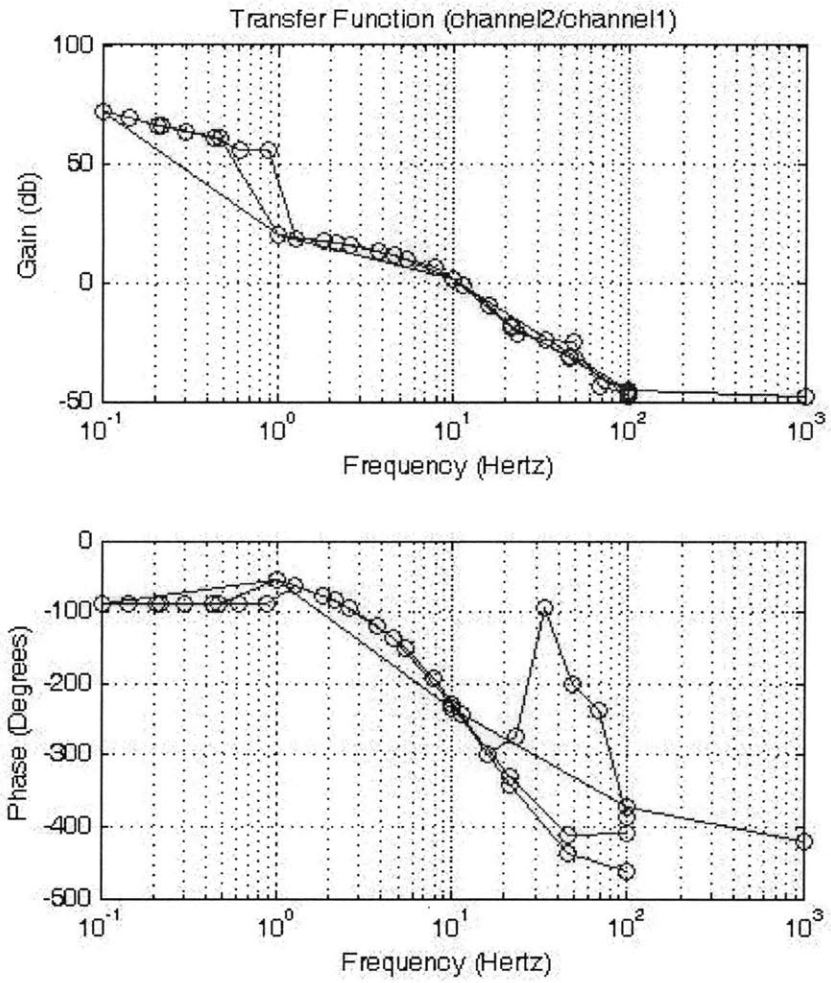

Figure 56: open loop frequency response of hydrostatic thrust bearing (bearing gap/average pump speed reference voltage)

Based on the frequency response a simple PI controller was developed. Figure 57 shows the algorithm that was used to control the speed of the eight pumps based on the measurement of the three capacitance probes. Each sensor controls the pocket that has the highest impact on the sensor output and its two immediate neighbors. The two neighbors receive the control input of the main pocket multiplied with a pocket gain. The pocket gain that is linked to each pocket is proportional to the impact that each pocket has on the corresponding sensor i.e. the higher the impact, the higher the gain. If one pocket influences several sensors, ideally all sensors should be linked back to the pocket via a controller and a pocket gain. The sum of all pocket gains that are

associated with one pocket should never be bigger than a predetermined value that corresponds to a pocket that only influences one sensor.

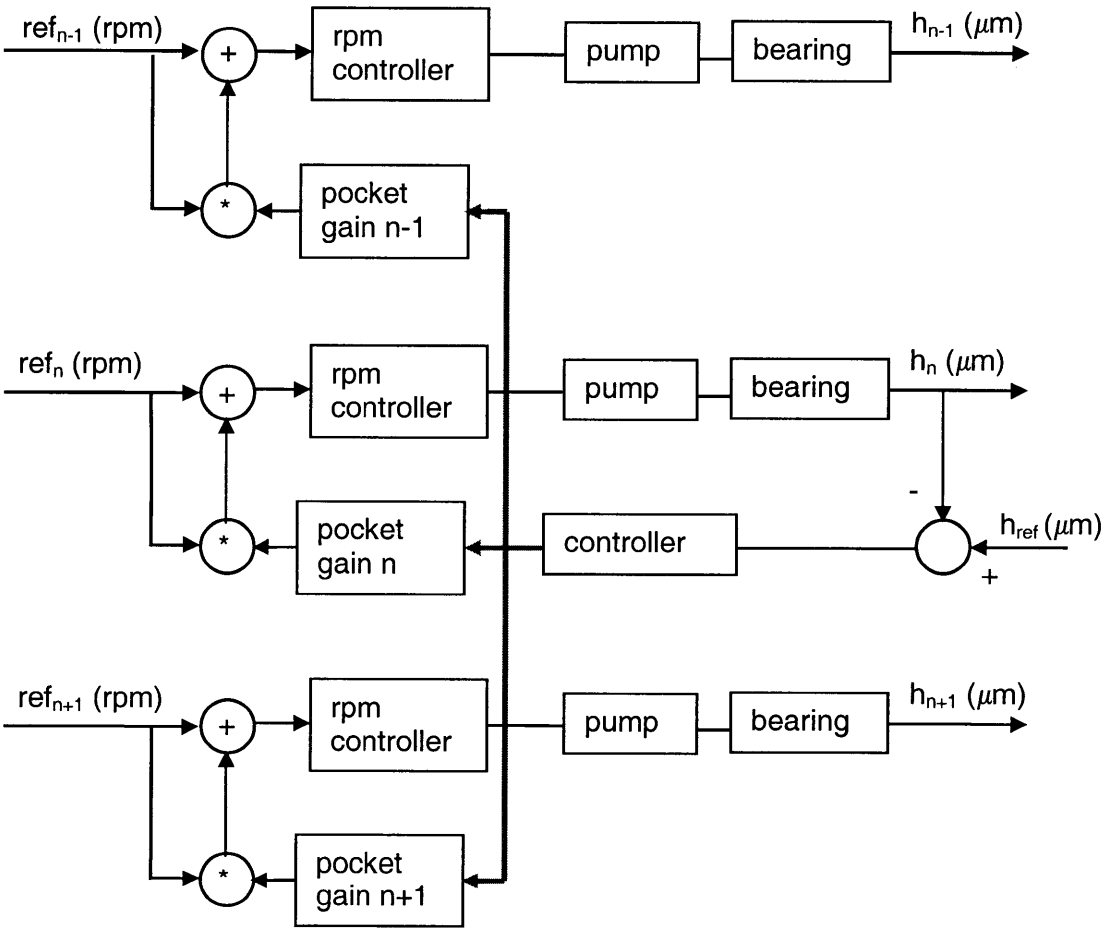

Figure 57: gap feedback control algorithm, one sensor controls multiple pockets

Figure 58 shows the response of the thrust bearing to four 68N load increases followed by four 68N load decreases.

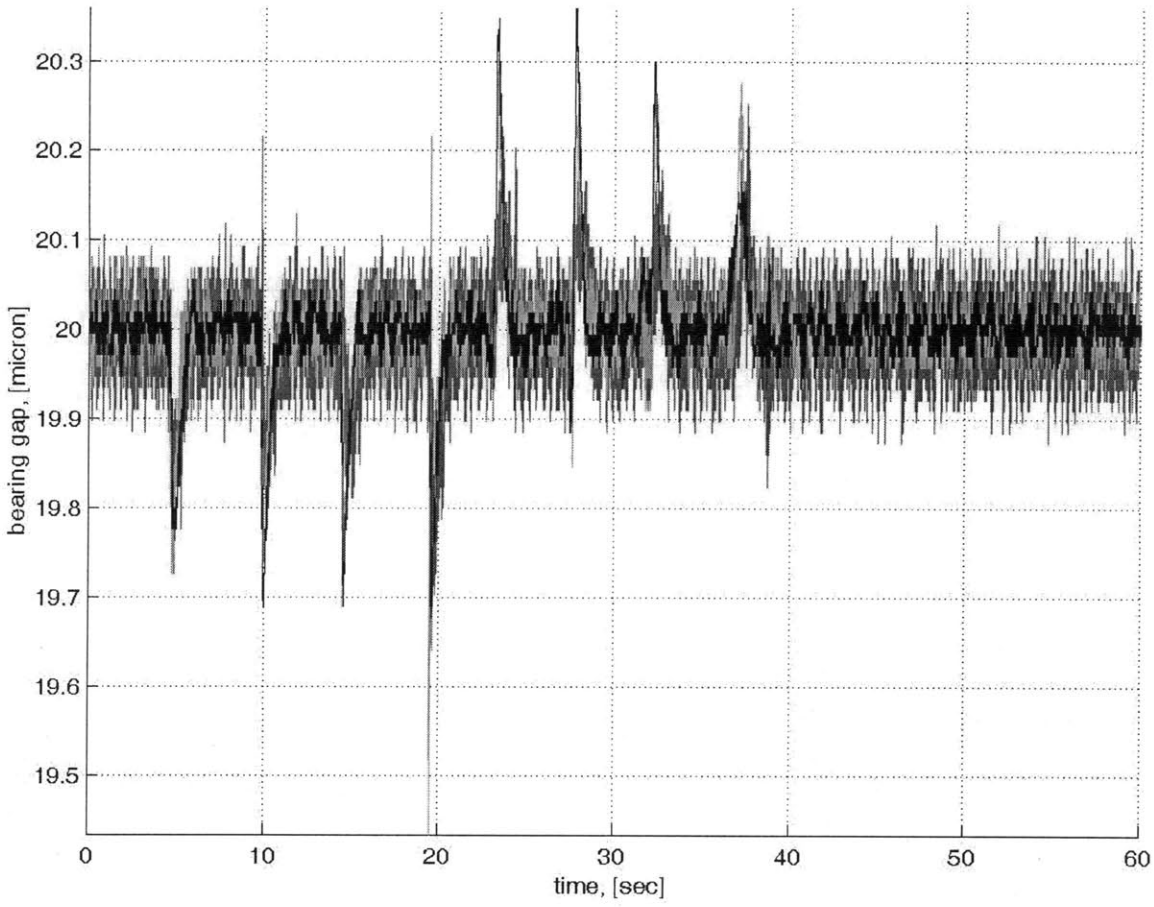

Figure 58: gap feedback control of the hydrostatic thrust bearing, 68N load steps

One performance limitation in the recorded step response is the noise level of +/-0.1μm

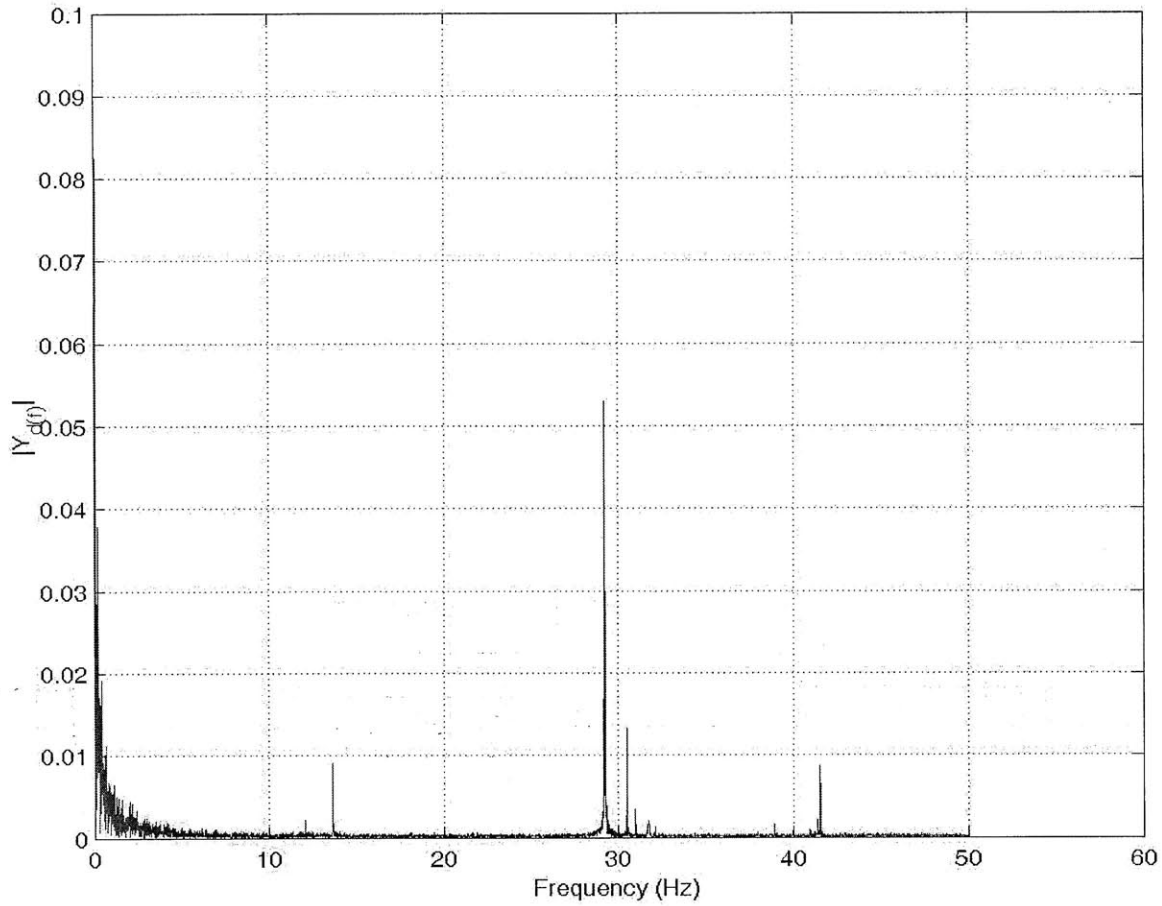

Figure 59: bearing noise frequency spectrum

To prevent significant error motion through pressure fluctuation either specially designed filters or accumulators can be added in the supply line. However, any of these elements will further complicate the dynamic response of the bearing or lower the bearing stiffness. A better approach would be to use a pump that by design has sufficiently low pressure fluctuations, see Chapter 3.3.

4.2 Conclusion and Outlook

The design of a magnetically and gravity preloaded, multi-pocket hydrostatic thrust bearing was presented. The static stiffness of the bearing was significantly below the theoretical bearing stiffness. A pressure dependent fluid supply (pumps) as well as insufficiently flat bearing surfaces could be identified as the core reasons for the lower than expected stiffness.

Different control algorithms were tested to increase the stiffness and improve the dynamic behavior of the thrust bearing. Gap feedback turned out to be a very promising approach to control the bearing gap. Due to the pressure dependent and time changing performance of the used low cost gear pumps model based pressure feedback could not yield performance improvements.

Pump induced gap vibrations were another undesired problem that was caused by the used gear pump.

The design of a better performing, pressure independent, constant flow and low flow fluctuation supply pump will be subject to future work. Most likely this pump is going to be built of a large volume piston.

After remachining the bearing plate and with a more appropriate constant flow pump, the theory described in this chapter should form the basis for a functioning model based pressure feedback control of the bearing.

Last but not least the material combination of rare earth permanent magnet material and stainless steel bearing plate needs to be examined closer. To prevent slow corrosion of the permanent magnets and steel plate the two parts might have to be separated

electrically by the use of appropriate coatings. Alternatively the steel plate can be replaced by a ceramic plate with a steel insert that is well sealed of the bearing fluid and electrically isolated such that there is no conductive connection between the steel insert and the permanent magnets.

5 Height Adjustable Kinematic Couplings as a Novel Element in the Design of Stiff Machine Tools with a Tight Structural Loop

A machine's achievable manufacturing speed, accuracy and repeatability are often limited by the stiffness of its structural loop. Increasing the machine stiffness by making it bigger is costly and often violates space constraints for footprint of the machine. Therefore it is generally desirable to keep the length of the structural loop at a minimum. However, compact machine designs can create a challenge for requirements such as access to the machine, tool, work-piece, or for maintenance or work-piece handling aspects.

This chapter presents a design method and kinematic coupling element to achieve a compact structural loop that can be opened, closed, and adjusted between machining cycles, yet accurately aligned and locked and fine adjusted during machining cycles. For this, machine elements that combine high stiffness, high repeatability, and adjustability are needed. In instrument applications that also require high repeatability, it is common to use a kinematic coupling with up to six degrees of freedom [22, 23, 24, 25, 26]. Very high rigidity kinematic couplings can be used to minimize the structural loop of multi-axis precision grinding machines while reducing machine cost and complexity.

Kinematic couplings are exact constraint interfaces that provide only as many constraints as degrees of freedom that need to be restrained. As an exact constraint device, high load and stiffness capable kinematic couplings inherently provide repeatable opening and closing. Repeatability of (+/-0.25μm) has been reported in instrument applications [27, 28, 29, 30, 31]. The stiffness of the coupling scales with the applied preload ^1/3 and therefore contact stresses grow faster than the achievable stiffness. Consequently in order to maximize the coupling stiffness, especially in high cycle applications, corrosion free, high strength contact materials (ceramics) should be used. We have noted that to obtain very high stiffness, very high preload forces are required and thus by providing the ability to servo control the preload force, we can take advantage of the simple relation $F=k*\Delta$; by servo controlling the preload force, small controllable elastic deformations of the coupling can in theory be used to adjust height and tilt of the coupling with nanometer resolution.

The presented height and tilt adjustable three-V-groove canoe-ball kinematic coupling design allows for repeatable opening and closing of the coupling interface as well as nano-, micro- and macro- height and tilt adjustability. This coupling was created to enable machine tools to attain an extremely tight structural loop. Repeatable opening and closing of the coupling allows access to an otherwise very compact and possibly difficult to access machining area. Macro (mm) height adjust of the coupling allows for different tool geometries. Micro and nano (μm, nm) adjustments enable tool wear compensation as well as micro/nano positioning of the tool relative to the work-piece. Preload is achieved using ballscrews that pass through the center of the coupling, and load washers enable servo control of the preload force. At a preload of 26kN the coupling achieves a stiffness of 7N/nm at the coupling interface. By varying the preload

on the coupling by +/- 10%, in-process nm to μm height and tilt adjustment at >95% of the nominal stiffness is possible.

When under light or no preload each canoe-ball interface can be adjusted over a range of 10mm using a wedge mechanism, which, controlled by a separate screw actuator, changes the effective width of the V-groove.

While static friction between the elements prevents back-driving the system and thus helps to maintain high stiffness without having to power the screw, mm height adjustment is only possible under significantly decreased preload, and thus stiffness, and is considered a set-up change operation.

Furthermore the preload ballscrews can be long and hence when reversed, they can open the machine up by separating the coupling elements and thus raising one part of the machine with respect to the other to gain free access to the workspace.

5.1 Kinematic Wedge Couplings

By combining a conventional kinematic coupling with a wedge mechanism, an ultra stiff coupling with 8mm of height adjustment has been realized as shown in Figure 61. The mechanism consists of three male, ceramic "canoe balls", with effective Hertzian contact radii of 500 mm, that each make point contact with each of two tapered wedge-shaped ceramic blocks.

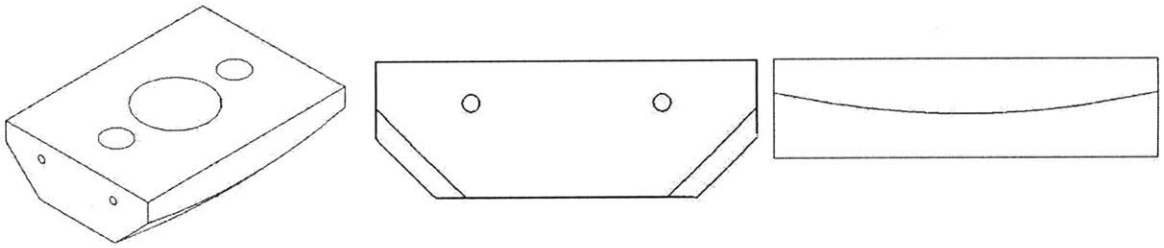

Figure 60: male canoe ball vee

The two wedges slide within a stainless steel female tapered V. Moving the two wedges relative to the V and hence also the canoe ball changes the effective width of the V and consequently the vertical position of the canoe ball also changes. The wedges also act as a non-back-driveable transmission element between their axial motion and the vertical motion of the canoe ball. The entire mechanism is shown in Figure 60.

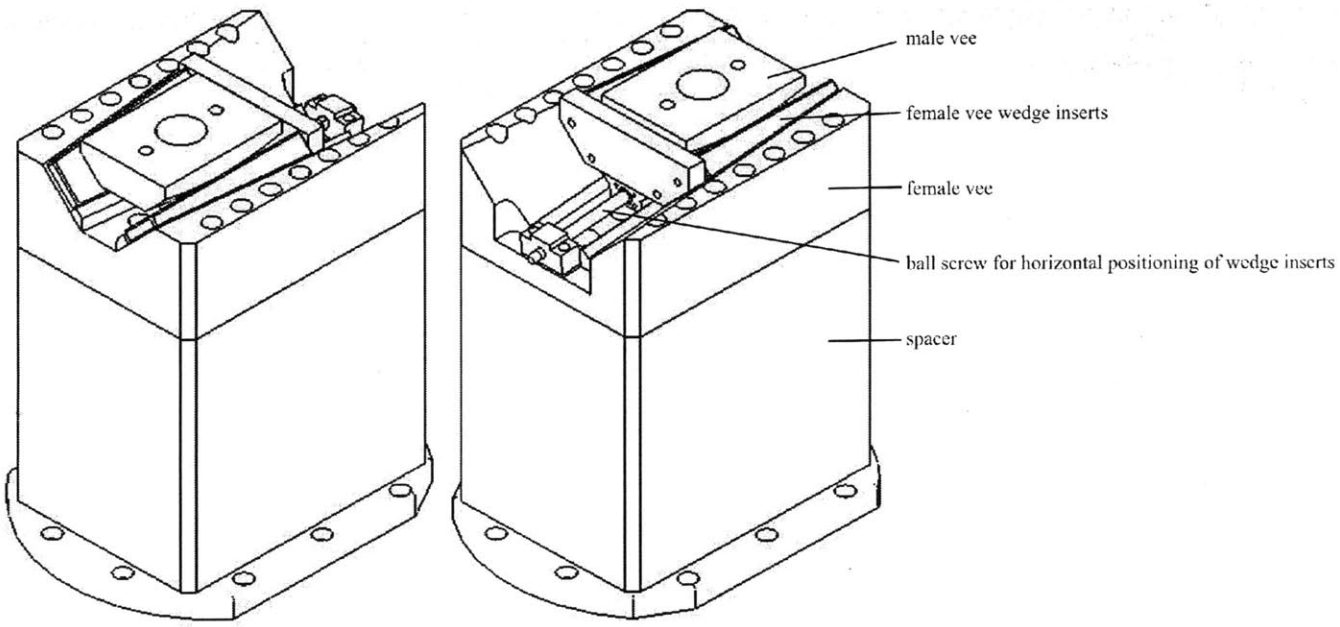

Figure 61: height adjustable kinematic coupling

By varying the preload of the coupling by up to +/- 10% it is also possible to use the large but finite stiffness of the kinematic couplings for in-process nm-resolution height and tilt adjustment at >95% of the nominal stiffness. The presented coupling was

designed for a nominal preload of 30kN and a nominal stiffness of 6.8kN/μm, using the spreadsheet shown in Figure 62.

Metric units only! Enters numbers in **BOLD**, Results in RED					**Material properties**	
Standard 120 degree equal size groove coupling? (contact forces are inclined at 45 to the XY plane. For non standard designs, enter geometry after results section)				TRUE	*User defined material*	*aluminum*
					Yield stress	
System geometry (XY plane is assumed to contain the ball centers)					plastic	3.45E+07
Dbeq (mm) =	0	Equivalent diameter ball to contact the groove at the same points			RC 62 Steel	1.72E+09
Rbminor (mm) =	500	"Ball" minor radius			CARBIDE	3.50E+10
Rbmajor (mm) =	500	"Ball" major radius			user defined	2.76E+08
Rgroove (mm) =	1.00E+10	Groove radius (negative for a trough)			*Elastic modulus*	
Costheta =	TRUE	Is ball major radius along groove axis?			plastic	2.07E+09
Dcoupling (mm) =	1000	Coupling diameter			RC 62 Steel	2.04E+11
Fpreload (N) =	-30,000.00	Preload force over each ball			CARBIDE	4.15E+11
Xerr (mm) =	0.0	X location of error reporting			user defined	6.80E+10
Yerr (mm) =	0.0	Y location of error reporting			*Poisson ratio*	
Zerr (mm) =	0.0	Z location of error reporting			plastic	0.20
Auto select material values (enter *other_4* to the right)					RC 62 Steel	0.29
Matlabball =	3	Enter 1 for plastic, 2 for steel, 3 for carbide, 4 for user defined, 5			CARBIDE	0.21
Matlabgroove =	3	where each ball and groove is defined individually			user defined	0.29
Min. yield strength (Pa, psi)		3.50E+10	5,072,464			
Largest contact ellipse major diameter (mm)		6.663				
Largest contact ellipse major diameter (mm)		6.653				
Largest contact stress ratio		0.016	Hertz shear stress/tensile yield/2			
RMS applied force F (N)	1					
RMS deflection at F (micron)	0.000					
RMS stiffness (N/micron)	6,832	2,277				

Figure 62: kinematic coupling design spreadsheet [1]

For the sake of simplicity the load displacement behavior of the coupling can be locally linearized. Based on this linear model a decrease of the coupling preload from 30kN to 27kN predicts a displacement of 0.4μm. The measured load displacement behaviour of the coupling at different preloads is discussed later.

Combining a kinematic coupling and a wedge mechanism enables mm height adjustment during set-up, prior to machining to accommodate for gross tool or work piece thickness variations. The slope angle of the wedge should be chosen shallow enough to prevent sliding of the wedge when the preload is applied (self-locking friction). In the current design the slope angle has been chosen at 4.04º such that a 1:10 horizontal to vertical displacement transmission ratio was achieved i.e. 80mm of

[1] www.kinematiccouplings.org

horizontal travel yields 8mm of height adjustment. The coefficient of friction of silicon carbide on itself is 0.7. tan(4.04º)<0.7 2 → therefore the height adjust of the coupling is self-locking under preload.

Due to static friction between the wedges and the steel vee as well as between the wedges and the canoe ball, accurate coarse control of the coupling height via a wedge mechanism is only possible under low (close to zero) preload. Therefore the stiffness of the coupling interface during mm-level height adjustment is essentially on the order of the preload mechanism's stiffness. However, this is acceptable as the coupling is not meant for in process mm height adjustments.

Depending on the horizontal to vertical motion transmission ratio, most of the load that resists motion of the wedges is caused by friction. This load will result in an axial error in the (horizontal) positioning of the wedge inserts and correspondingly a friction and preload dependent height error in the coupling. Consequently, for a given acceptable height error, during mm-level height adjustment, the coupling preload should not exceed a critical value.

$$\delta_x = \frac{F_x}{k_x} \approx \frac{F_x L}{AE} \tag{5.1-1}$$

$$\delta_\theta = \frac{T_x}{k_\theta} \approx \frac{T_x L}{GJ} \tag{5.1-2}$$

$$\delta_{xt} = \delta_x + p_{\theta x}\delta_\theta \tag{5.1-3}$$

$$\delta_y = \delta_{xt} r_{xy} \tag{5.1-4}$$

---

[2] NIST Property Data Summaries, Sintered Silicon Carbide, http://www.ceramics.nist.gov/srd/summary/scdscs.htm

$$F_x = \frac{F_p}{r_{xy}} + (\mu_1 + \mu_2)F_p \tag{5.1-5}$$

$$T_x = F_x p_{\theta x} \tag{5.1-6}$$

δ_x – axial error in positioning of wedge inserts

δ_Θ – torsional error in positioning of wedge inserts

δ_{xt} – total axial error in positioning of wedge inserts

δ_y – resulting coupling height error due to wedge motion

k_x –axial stiffness of wedge positioning screw

k_Θ – torsional stiffness of wedge positioning screw

F_p –preload force

F_x –axial force acting on wedge positioning screw

T_x – torque acting on wedge positioning screw

$p_{\Theta x}$ – lead of wedge positioning screw

r_{xy} – horizontal to vertical motion transmission ratio

L – length of wedge positioning screw

A – cross-sectional area of wedge positioning screw

E – young's modulus of wedge positioning screw

G – shear modulus of wedge positioning screw

J – second moment of area of wedge positioning screw

The coupling height is changed by repositioning the wedge inserts while the preload is controlled through a preload mechanism. When the wedges are repositioned to increase the coupling height, the preload mechanism has to open in order to maintain a constant preload. If the total axial error in the positioning of the wedge inserts under preload is big enough, slipping of the wedges can cause a sudden increase in preload and coupling

height. This can complicate or even prevent an accurate height adjustment of the coupling under preload.

When the wedges are repositioned to decrease the coupling height, the preload mechanism has to close in order to maintain a constant preload. If the total axial error in the positioning of the wedge inserts is big enough, a sudden breaking of friction can cause a sudden decrease in preload and coupling height, before the preload control can react.

Following this train of thought, a maximum acceptable wedge positioning error can be defined based on an acceptable preload variation. The preload variation causes a height tracking error at the Hertz contact interface. This tracking error is not to be confused with the previously mentioned resulting coupling height error due to the wedge motion. Other criteria might require a lower acceptable error.

$$\delta_y \leq \frac{\Delta F_p}{k_p} \tag{5.1-7}$$

$$\delta_h = \frac{\Delta F_p}{k_c} \tag{5.1-8}$$

k_p – stiffness of preload mechanism e.g. preload screw

k_c – Hertz contact pair stiffness =1/3 of coupling stiffness

ΔF_p – acceptable preload variation during positioning of the wedge inserts due to stick slip

δ_h – height tracking error due to deformation at Hertz contact interface

Consequently, a low axial stiffness of the preload mechanism, a high stiffness of the wedge positioning mechanism and a high coupling stiffness are actually desirable with respect to height changes of the coupling under preload. The total stiffness of the

kinematic coupling is determined by summing the stiffness of the preload mechanism and the Hertz contacts, where the Hertz contact stiffness usually clearly dominates the stiffness of the preload mechanism. Therefore, if the coupling has been dimensioned properly, lowering the stiffness of the preload mechanism does not significantly impact the overall coupling stiffness.

In the case of non-back drivable preload mechanisms any change in preload due to wedge motion, requires active compensation by repositioning the mechanism. E,g, in the case of a DC motor actuated, non-back drivable preload mechanism, an increase in preload due to wedge motion requires a temporary reversal of the motor current in order to reposition the mechanism and thus maintain a constant preload. With a back drivable mechanism the preload can usually be controlled independent of position. A back drivable mechanism can be repositioned by the moving wedges, while a near constant preload is maintained (neglecting friction in the mechanism). In the case of a DC motor actuated, back drivable preload mechanism, an increase in preload due to wedge motion does not require a drastic change in the motor current. Obviously, from a controls point of view, a non-back drivable mechanism is the more difficult choice. On the other hand a non-back-drivable mechanism can passively maintain a certain preload whereas a back drivable mechanism requires permanent actuation.

5.2 Experimental System

The test system for the height adjustable wedge kinematic coupling as shown in Figure 63 uses only one height adjustable contact pair. The other two contact pairs are not height adjustable. The height adjustable contact pair is preloaded by a three phase electric motor and a ball screw that is actuated through a non-back driveable harmonic

drive (1:100 transmission ratio). The non-adjustable contact pairs are manually preloaded via a lead screw. The test system was built at the scale of a grinding machine in which the adjustable kinematic coupling is to be used. When the coupling interface is tilted the preload screws will be slightly bent. This bending changes the preload at the contact pairs. In order to prevent significant bending in the structure the test setup had to be designed such that the stiffness of its structure dominates the stiffness of the preload screws – as is the case in the real machine. The preload force on the adjustable contact pair was measured by four force transducers [3] that were positioned in between the ballscrew nut and the test setup structure. The preload was determined by adding the forces measured by each transducer – transducers act as parallel springs. The deformation at the two contact points was calculated based on a measurement taken by two Lion Precision capacitance probes as well as based on the preload screw encoder read-out. The probes were mounted to the female steel vee, while the probe target was mounted to the male vee. Two probes are needed in order to compensate for Abbe effects and to determine the real deformation at the contact points rather than the displacement between the probes and the target, as illustrated in Figure 64.

[3] Futek CSG 110

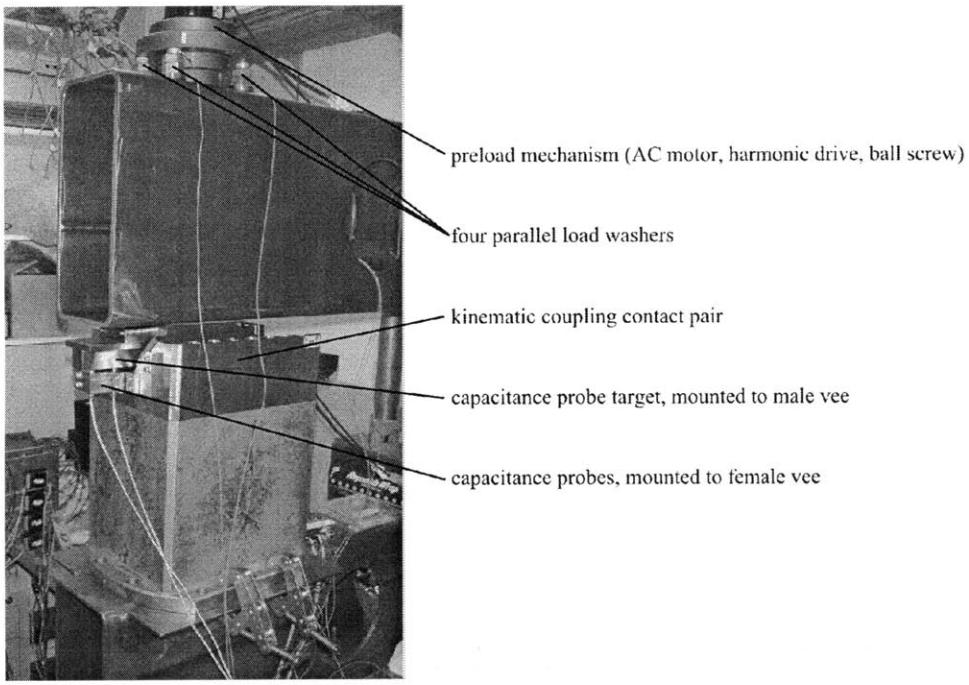

Figure 63: adjustable kinematic coupling test system

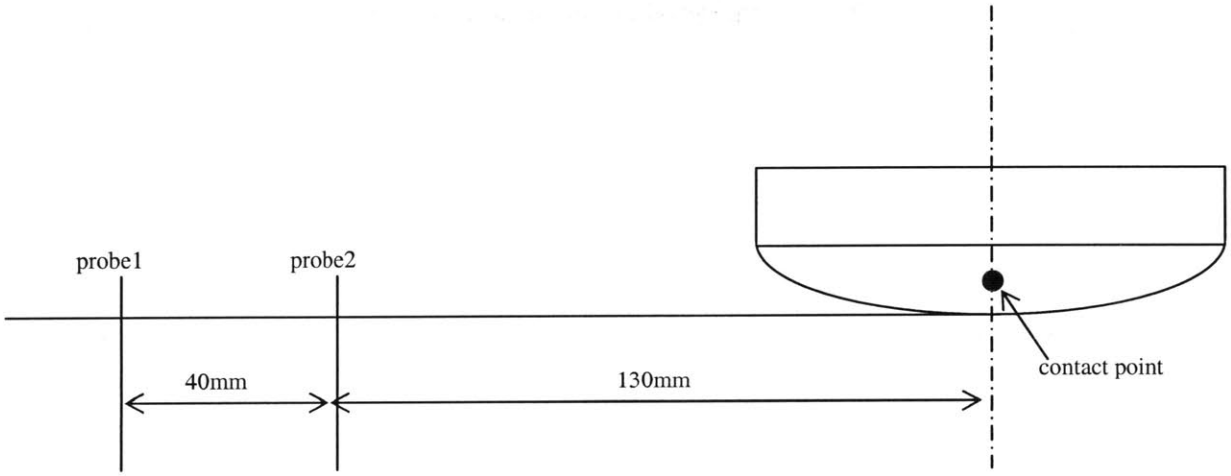

Figure 64: kinematic coupling sensor placement

$$m=(d_2-d_1)/40 \quad (5.2\text{-}1)$$

$$d_{contact}=d_2+m*130 \quad (5.2\text{-}2)$$

m – slope

d_1 – distance to target as measured by probe 1

d_2 distance to target as measured by probe 2

$d_{contact}$ – deformation at contact point

The preload-ball-screw-encoder was used to monitor the coupling height over a range of motion that exceeded the range of the capacitance probes. However, this method was limited to a height resolution of 3μm.

5.3 Measurement Results: Repeatability

In order to determine its repeatability, the coupling was opened, closed and preloaded up to ten times. When the coupling was "opened" the canoe ball had no contact with the female vee. This experiment was repeated at different preloads. In all cases a repeatability of better 1micron was achieved. Figure 65 shows the results of the measurement for preloads of 2kN and 10kN.

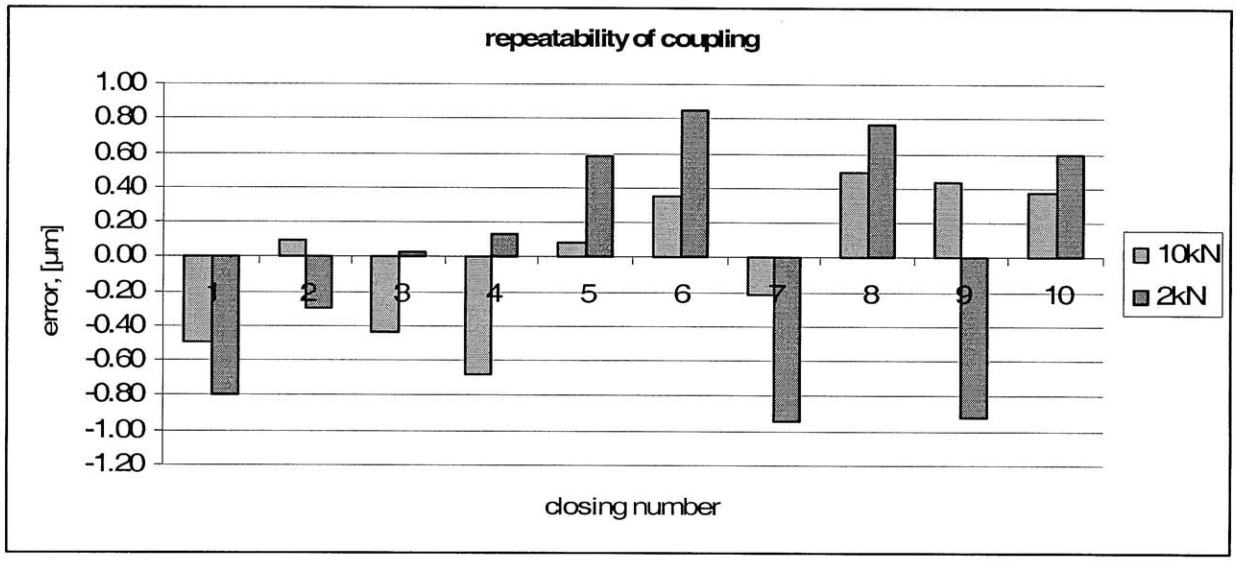

Figure 65: Closing-Repeatability of tested contact pair

5.4 Measurement Results: Adjustability

In order to measure the horizontal to vertical motion transmission ratio of the height adjustment, the position of the wedges and the preload were controlled in closed loop. The coupling contact pair was opened, the wedge was positioned horizontally, the coupling contact pair was closed again and a defined preload was applied. Then the resulting height was measured by:

the encoder of the preload ball screw. The horizontal motion of the wedge was about 10mm.

the capacitance probes. The horizontal motion of the wedge was about 275µm.

Figure 66 shows the 10:1 horizontal to vertical motion transmission ratio as measured at nine points, over >10mm of horizontal motion under different preloads. Figure 67 shows the height error as compared to the theoretical height given by a 10:1 transmission ratio. The average height errors as well as the min to max spread, as indicated by the error

bars, are below the resolution limit of the preload screw encoder (3μm) and therefore as expected.

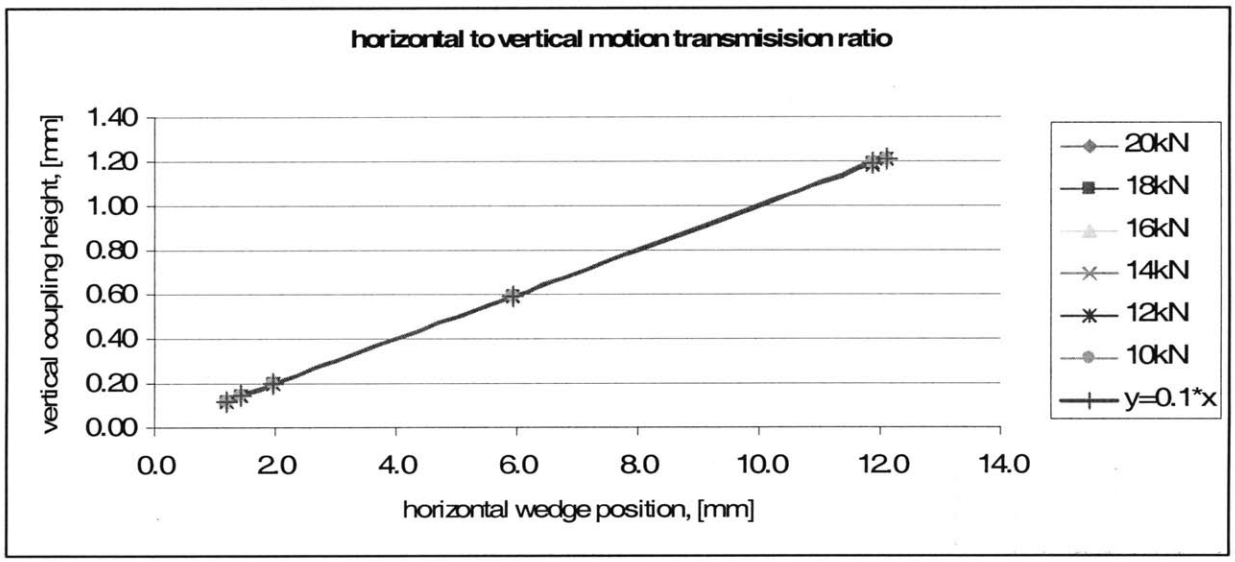

Figure 66: horizontal to vertical motion wedge transmission ratio

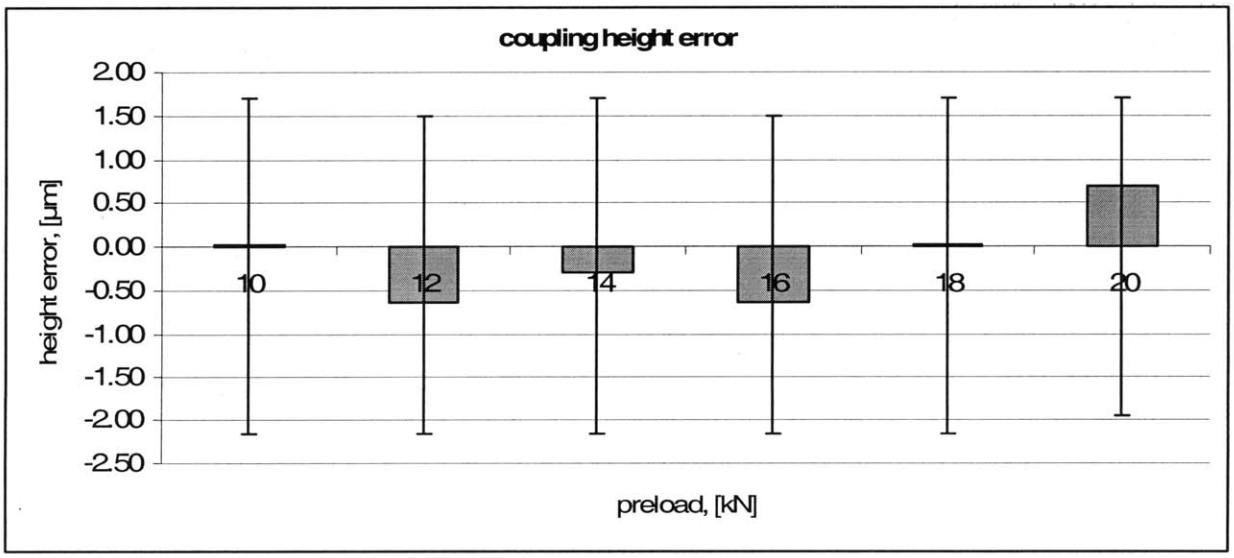

Figure 67: coupling height error in wedge transmission ratio measurement (average, max and min error)

Figure 68 shows the 10:1 horizontal to vertical motion transmission ratio as measured at eight points, over >250μm of horizontal motion under a preload of 10kN. Figure 69 shows the height error as compared to the theoretical height given by a 10:1

transmission ratio. The height errors were slightly more than +/-1µm and thus close to the repeatability of the coupling as shown in Figure 65.

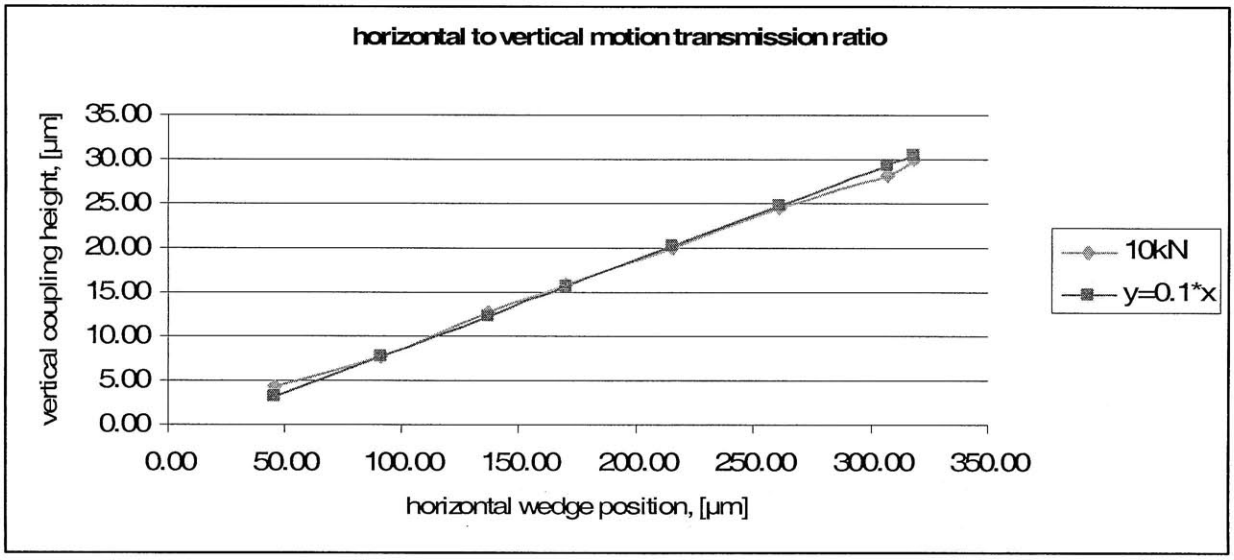

Figure 68: horizontal to vertical motion wedge transmission ratio

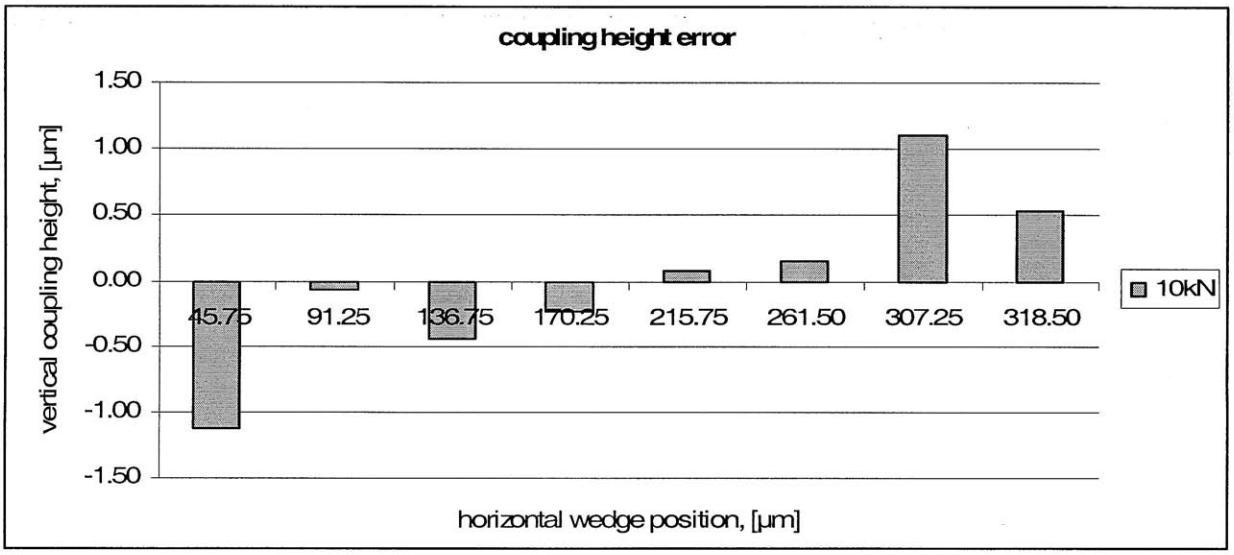

Figure 69: coupling height error in wedge transmission ratio measurement

5.5 Measurement Results: Stiffness

Figure 64Figure 71The load displacement behavior of the tested coupling contact pair was measured by applying a sinusoidal load variation centered at 18kN, 22kN and 26kN

applied preload. The displacement at the contact points was measured using the two capacitance probes. Based on the capacitance probe's measurements the displacement at the contact points was calculated according to the formula given in Figure 64.

For more accurate evaluation of the coupling stiffness as well as easier visualization the load displacement data, as shown in Figure 70, was filtered using a Butterworth low pass filter. This explains why the data does not follow a sinusoid at the beginning and end of the data array. The sinusoidal raw data is plotted in Figure 71. To illustrate repeatability of the measurement Figure 70 and Figure 71 each show three load and three displacement measurements Figure 70 and Figure 71 each show three load and three displacement measurements. Figure 70 and Figure 71 demonstrate how the coupling can be used as micro height and tilt positioning device. Centered at 26kN, the preload was varied by +/- 4kN or roughly 15% which resulted in a micro height adjustment range of +/-1.7μm.

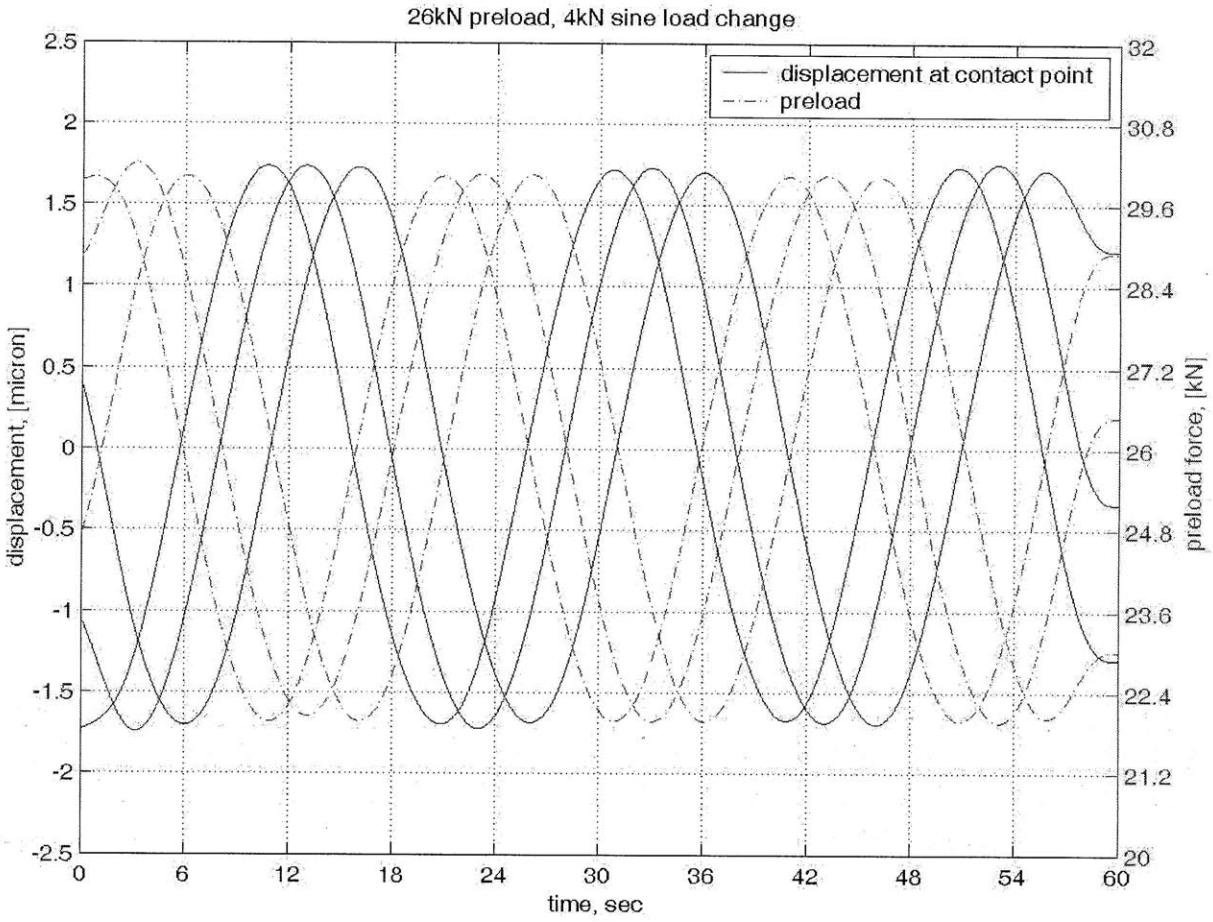

Figure 70: filtered load and displacement behaviour of tested kinematic coupling contact pair, 26kN

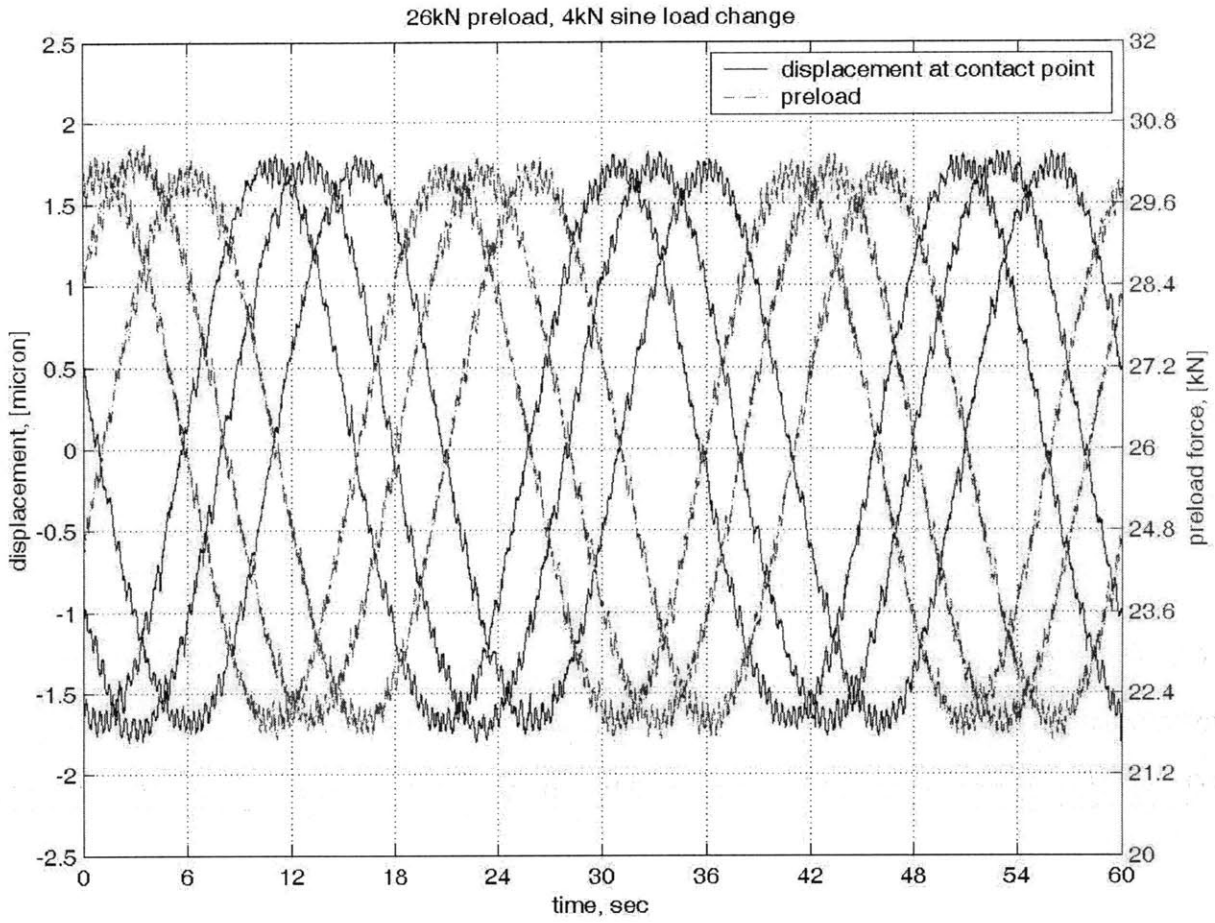

Figure 71: raw data of load and displacement behaviour of tested kinematic coupling contact pair, 26kN

Figure 72 to Figure 75 illustrate the load and displacement behaviour of the coupling at 18kN and 22kN preload. At lower preload the coupling stiffness is reduced and therefore a wider range of height adjustability range becomes possible. At an average preload of 18kN, +/-4kN or 22.2% load variation, results in +/-2.3µm of height adjustment. With a preload range of 14kN to 30kN per contact pair each contact pair's height can be adjusted by up to 8.2µm while maintaining a minimum stiffness of 1.6kN/µm per contact pair or 4.7kN/µm coupling stiffness. Theoretically, by extending the preload range from 6kN to 35kN per contact pair, a height adjustment of up to 14.4µm at the price of a coupling stiffness of ≥4kN/µm can be achieved. Further reducing the lower preload limit will increase the range of adjustability, however by also lowering the lowest coupling

stiffness. For this coupling the preload should not be increased beyond 35kN per contact pair. Accidental loading of the coupling with 40kN per contact pair caused structural failure of the SiC ceramic canoe ball; thus illustrating the care with which these types of elements must be used.

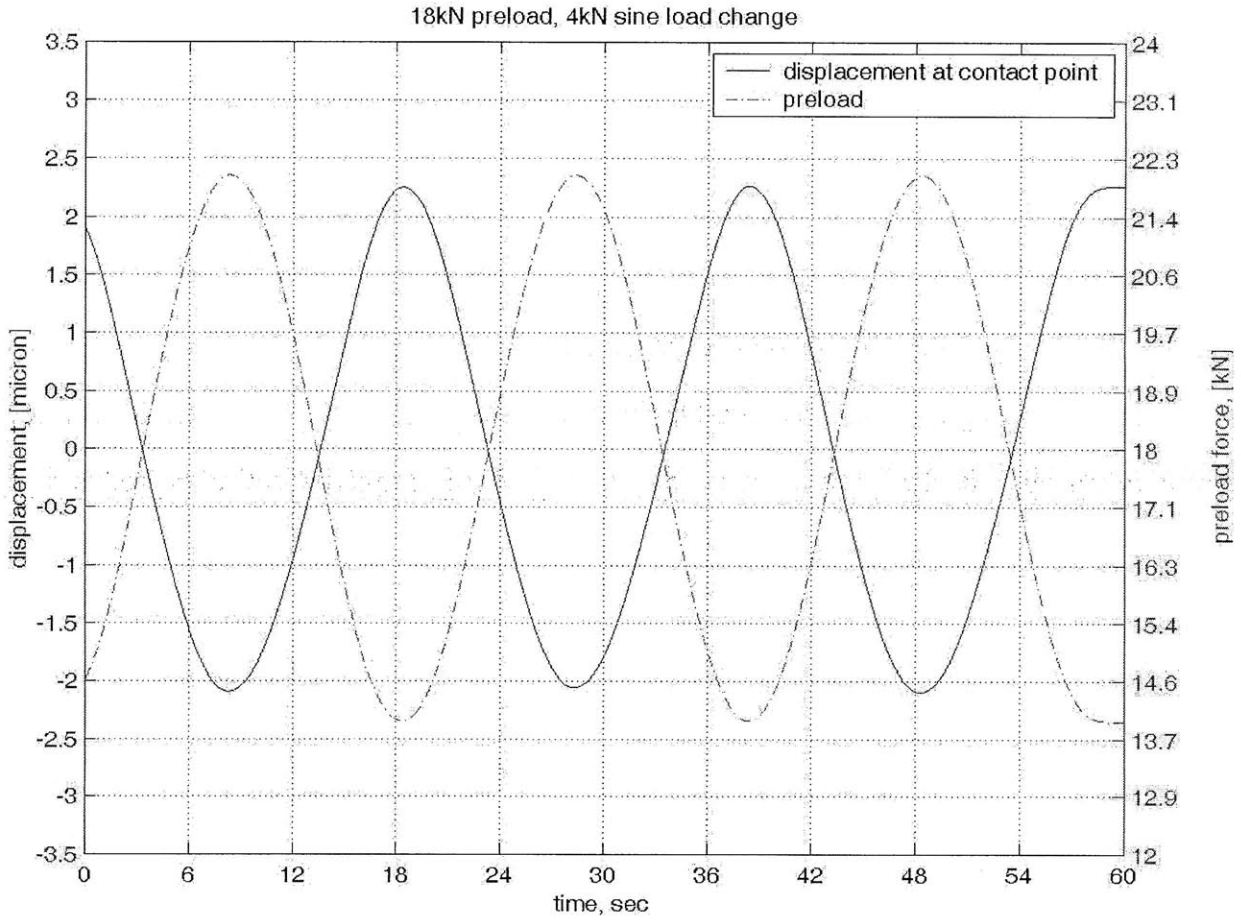

Figure 72: filtered load and displacement behaviour of tested kinematic coupling contact pair, 18kN

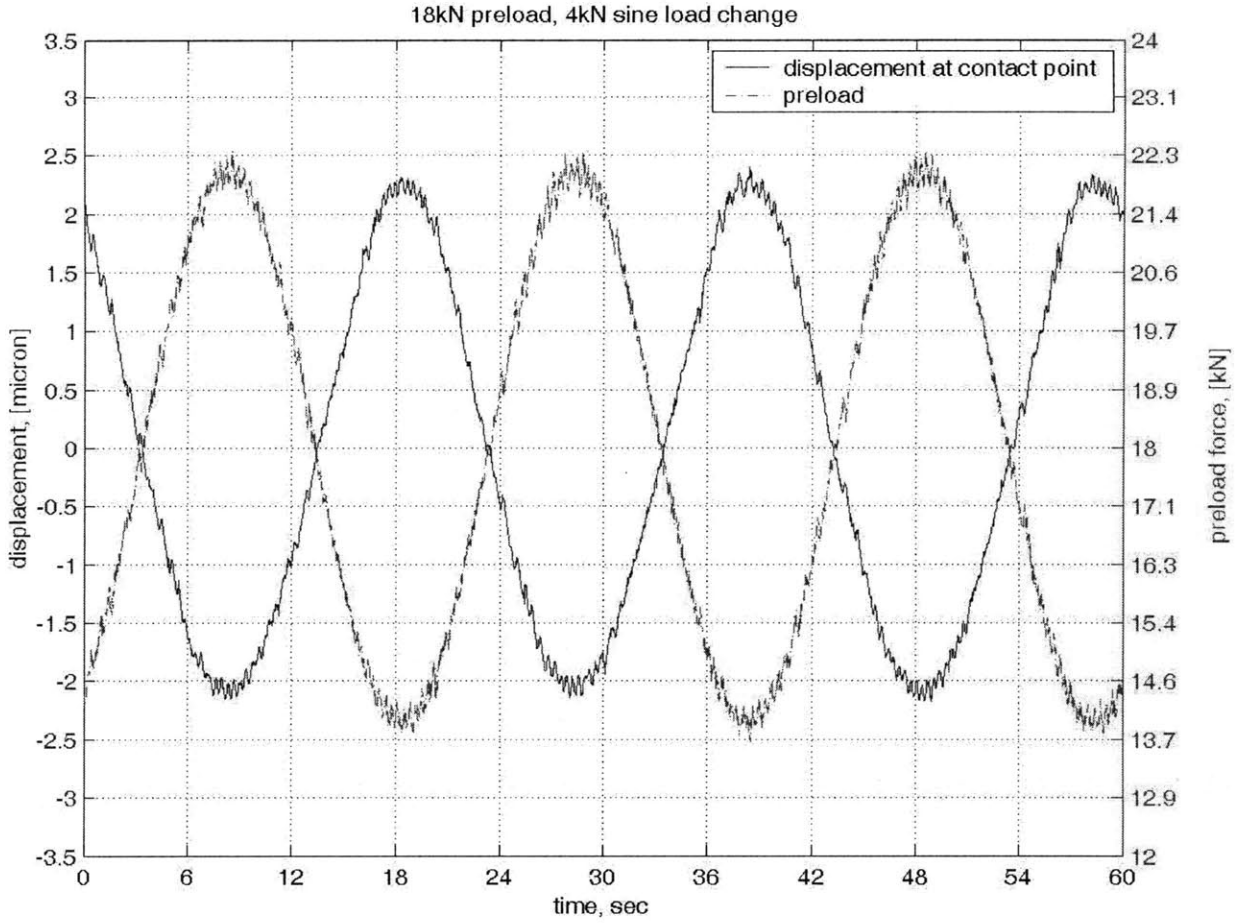

Figure 73: raw data of load and displacement behaviour of tested kinematic coupling contact pair, 18kN

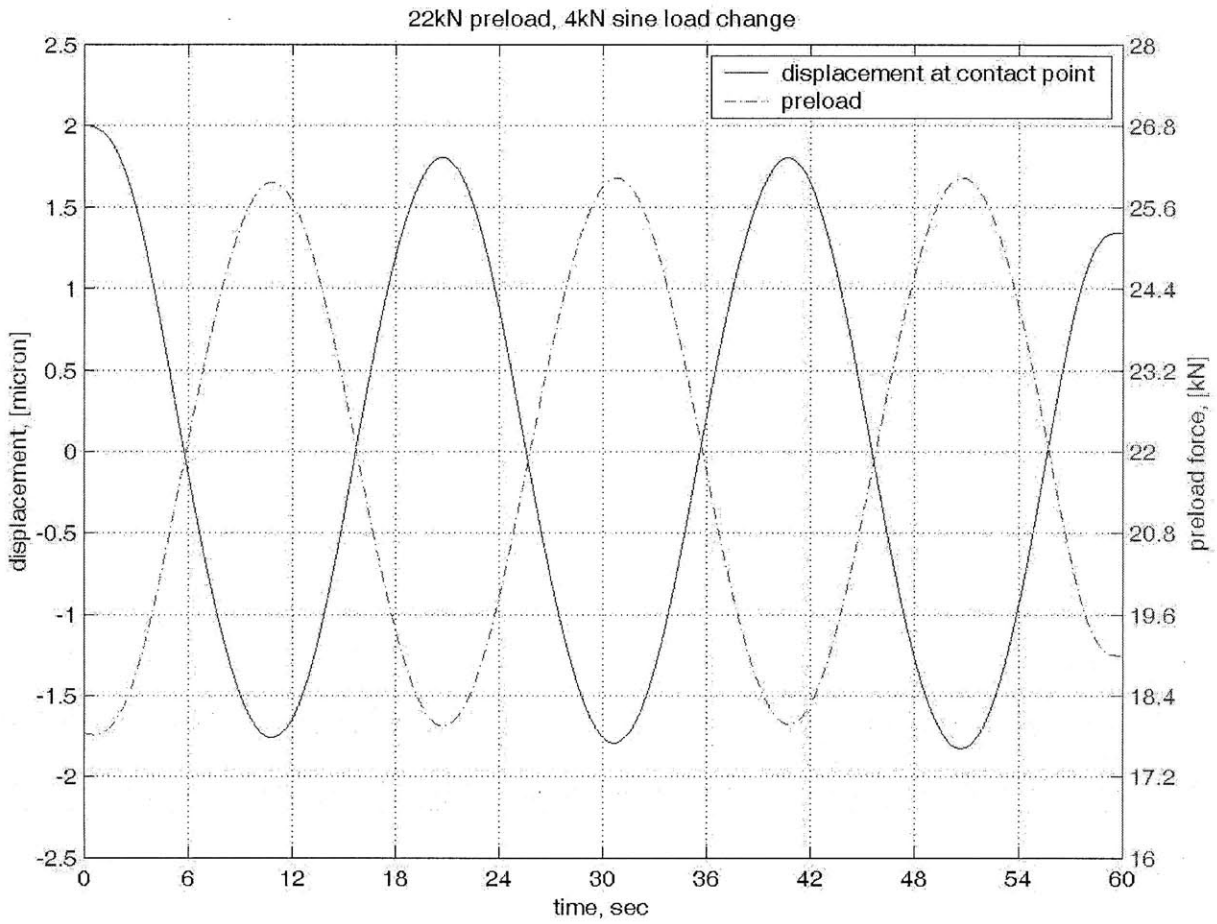

Figure 74: filtered load and displacement behaviour of tested kinematic coupling contact pair, 22kN

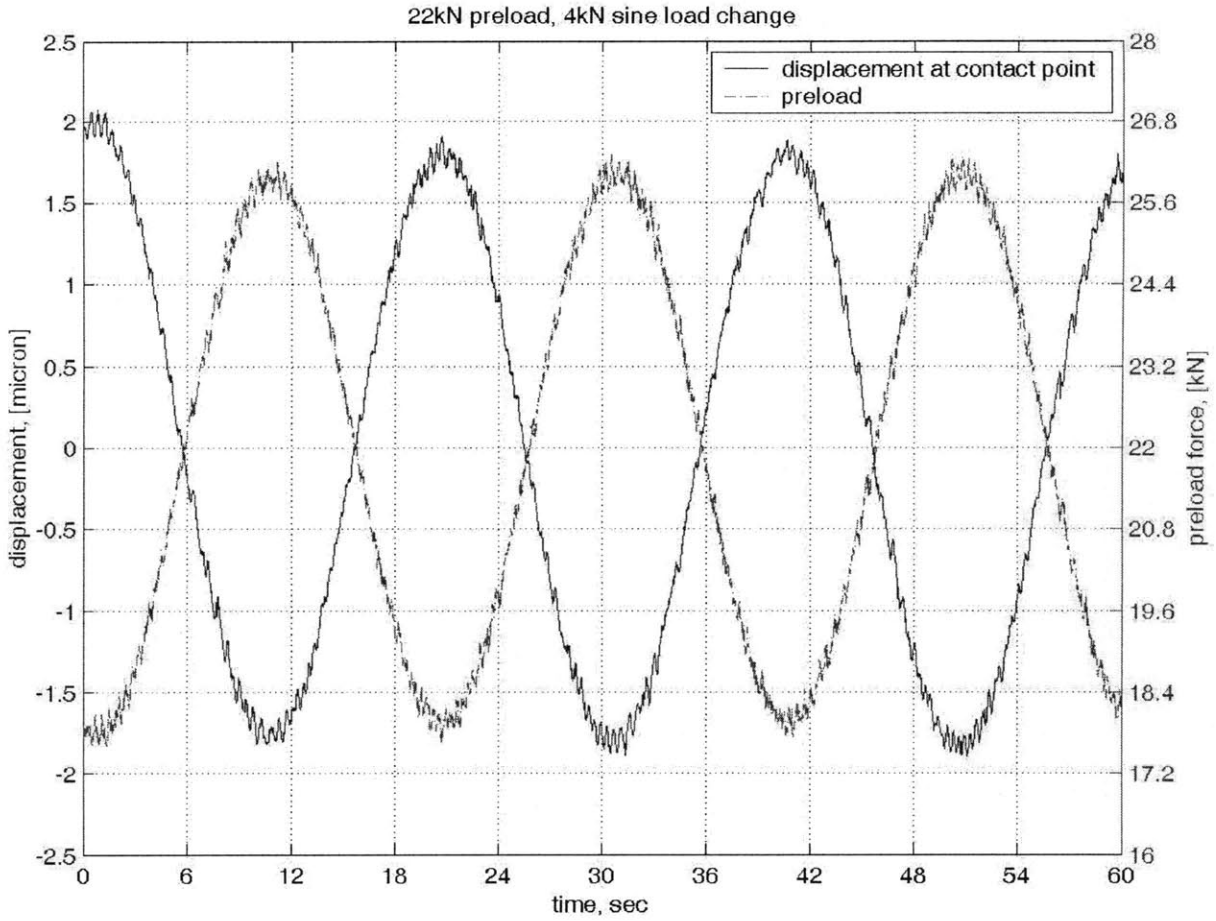

Figure 75: raw data of load and displacement behaviour of tested kinematic coupling contact pair, 22kN

The load-displacement behavior of the coupling as measured in the previously described experiment is plotted in Figure 76 to Figure 78. In order to eliminate the effects of the Butterworth low pass filtering the data has been truncated to a little more than one load-sinus-period taken out of the centre of the data array. It is important to note that with increasing preload the load displacement curve becomes a hysteresis loop. This shows an increasing effect of friction that results of the male vee getting more and more deformed, and pushed into/clamped in the female vee. When the coupling is used in micro positioning mode this friction-effect might cause problems in the dynamic control of the coupling height. Depending on the applied preload the width of the hysteresis loop

might limit the accuracy of the coupling height adjust to less than 0.1 and up to 0.4µm. However, this remains to be examined in future research.

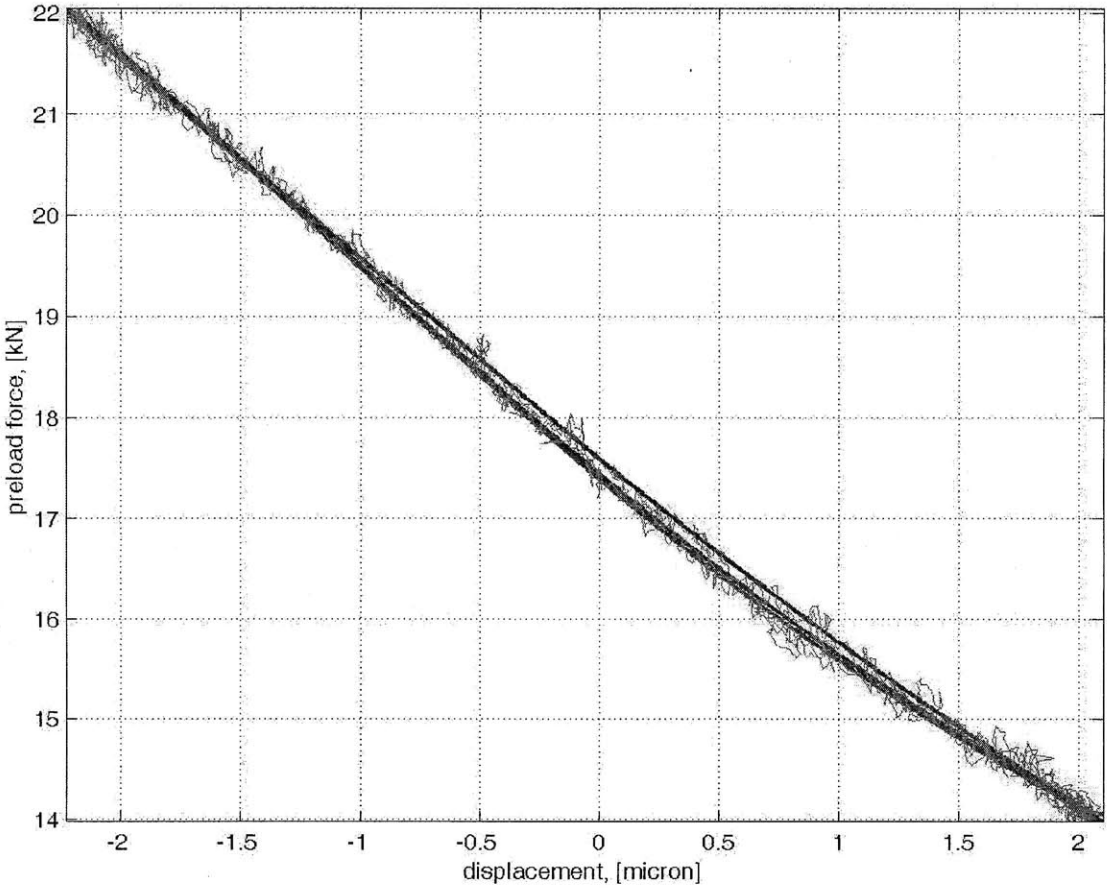

Figure 76: load displacement curve of tested kinematic coupling contact pair, 18kN; raw data and filtered data

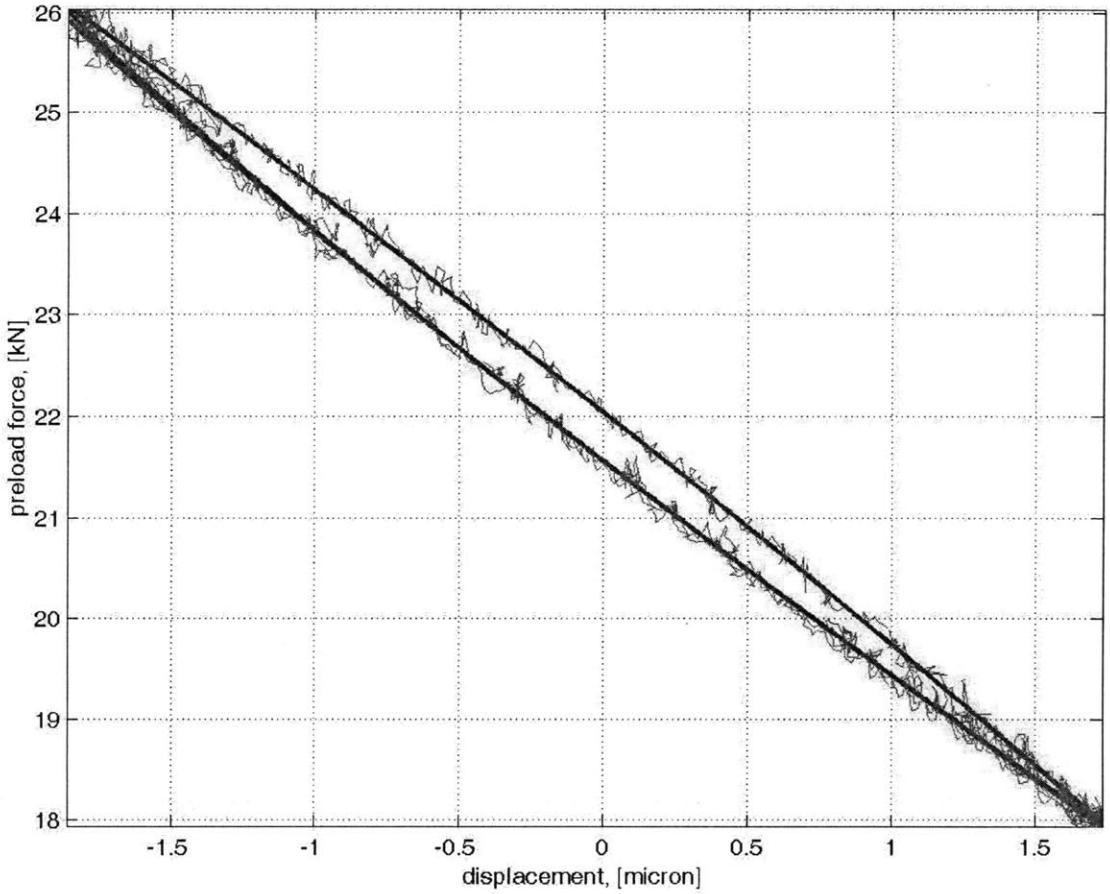

Figure 77: load displacement curve of tested kinematic coupling contact pair, 22kN; raw data and filtered data

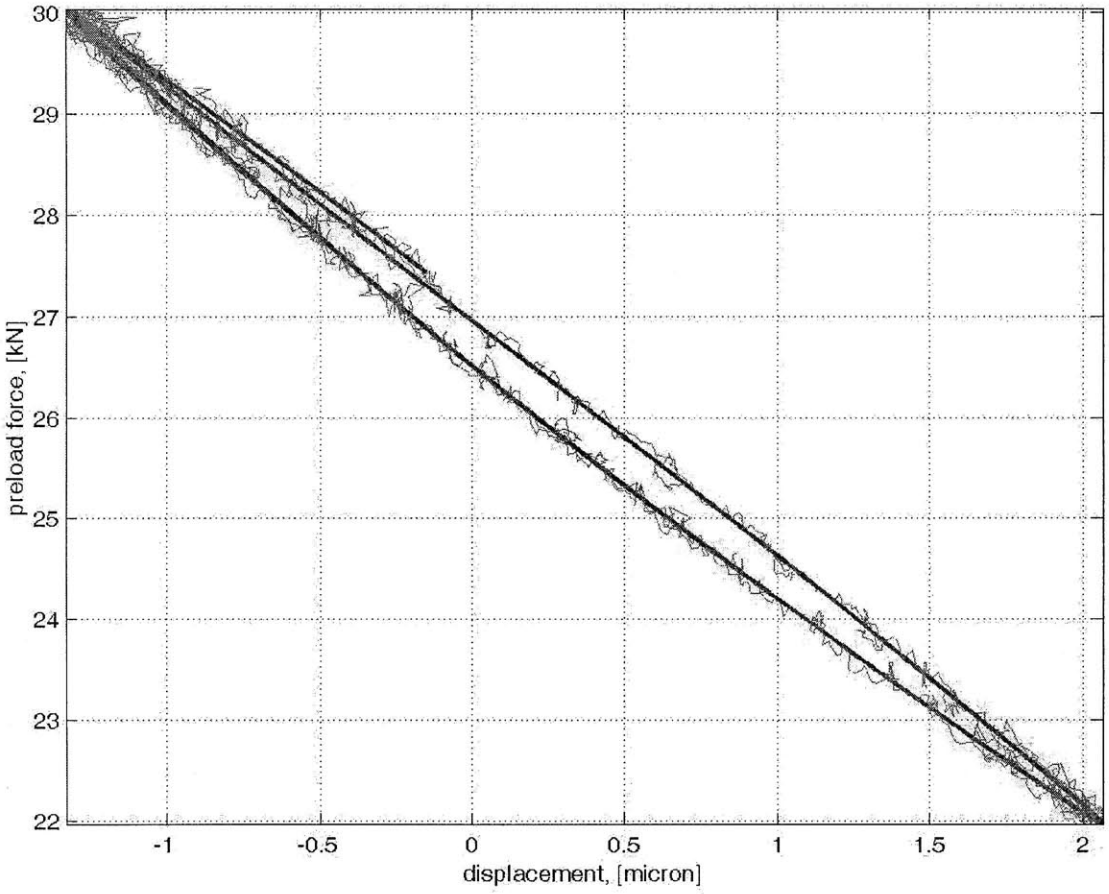

Figure 78: load displacement curve of tested kinematic coupling contact pair, 26kN; raw data and filtered data

At 26kN preload per contact pair a stiffness of 2.37kN/µm was measured. For three equal contact pairs this amounts to 7.1kN/µm at the coupling interface. The designed nominal allowable preload per contact pair is 35kN. Therefore, the following scaling law predicts a theoretical maximum stiffness of up to 7.8kN/µm – this theoretical, scaled stiffness remains to be confirmed by tests [4].

[4] A servo error occurred and the silicon carbide canoe broke when subjected to an unintentional loading with 40kN per coupling pair.

$$k = k_0 (\frac{W}{W_0})^{\frac{1}{3}} \quad (5.5\text{-}1)$$

k_0 – measured stiffness

W_0 – preload at measured stiffness

W – theoretical preload

k – scaled stiffness at preload W

Figure 79 shows the measured and theoretical stiffness of one contact pair at 18kN, 22kN and 26kN preload. The measured coupling stiffness is within 96% to 109% of the predicted stiffness. The theoretical stiffness was computed based on a Silicon Carbide Young's modulus of 415kPa and a Poisson Ratio of 0.21. The measured stiffness is generally higher than the predicted stiffness. Furthermore the prediction error increases with increasing preload. Friction – as shown in Figure 76 to Figure 78 is assumed to be the main contributor to the prediction error. The effect of friction on the performance of kinematic couplings has been examined by Layton Hale [32].

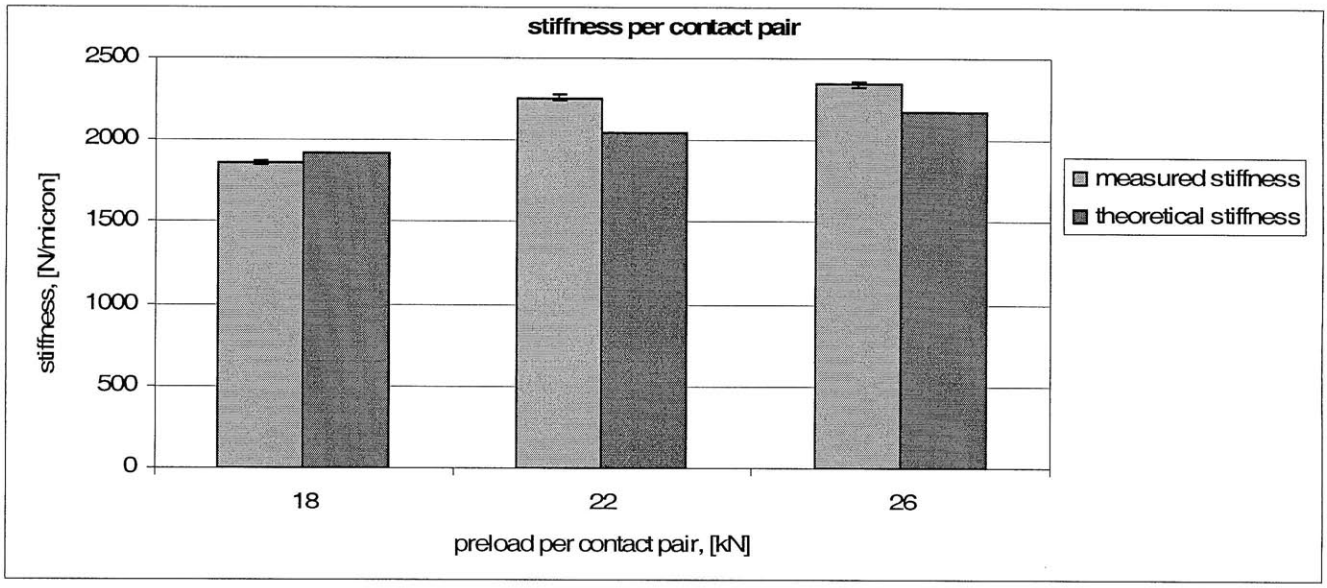

Figure 79: measured versus theoretical stiffness per contact pair

5.6 Conclusion and Outlook

A more compact, closed structural loop machine can be designed using an adjustable kinematic coupling [5], where the distance between the mating elements can be changed by a servo-controlled wedge element. This kinematic coupling mechanism provides increased stiffness as compared to a large, open structural loop machine tool with multiple stacked axes that can each move by a small amount.

The adjustable kinematic coupling mechanism that has been presented achieves a stiffness exceeding 7kN/µm. The wedge kinematic coupling design in combination with preload control enables fine in-process height adjustment with a range of up to 8.2µm at each contact pair while maintaining a coupling stiffness (three contact pairs) of ≥4.7kN/µm. At this point the height adjustment resolution is limited to +/-1µm - primarily due to noise in the preload control which was caused by friction in the preload

[5] AKC appears to be an appropriate TLA for this new type of kinematic coupling, but this TLA is already used by the American Kennel Club, and hence suggestions for an appropriate TLA for the adjustable kinematic coupling would be welcomed.

mechanism and at the Hertz contact interface. Theoretically up to 14µm of height adjustability at each contact pair can be achieved while maintaining a stiffness of ≥4kN/µm. It was shown that especially at high preloads (≥18kN per contact pair) friction between the canoe balls and the vees is a significant factor in the coupling performance. The impact of friction on this coupling remains to be examined in more detail.

For lower stiffness applications, friction based limitations on the coupling performance with respect to positioning resolution and accuracy can be entirely eliminated by using aerostatic or hydrostatic kinematic couplings [33]. Figure 80 illustrates one concept for such an aerostatic, adjustable kinematic coupling with an aerostatic bearing at each surface interface. For increased stiffness the bearings at interfaces that don't experience any relative motion at a given point of time can be shut off. E.g. when the wedges don't need to be repositioned, the aerostatic bearing between the wedges and the female vee can be switched off.

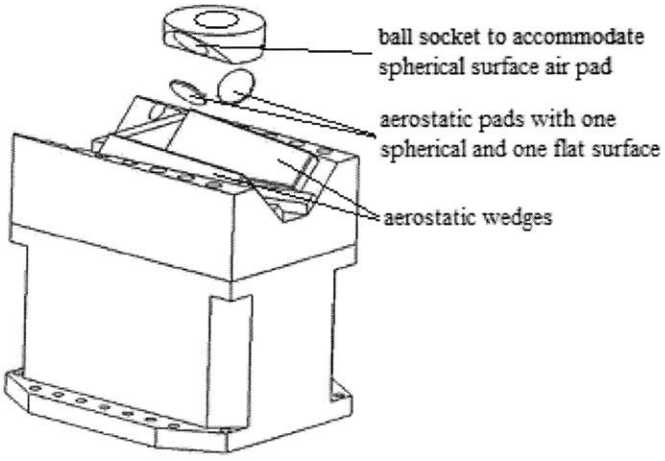

Figure 80: adjustable, aerostatic kinematic coupling contact pair

If a preload mechanism that goes through the center of the male vee is used – such as the ball screw in the presented design - mounting or removing the male vee is only

possible when the preload mechanism is removed. Depending on the machine design this can require taking apart the entire machine (i.e. remove upper half that is supported by the coupling). A split male vee design similar to the one shown in Figure 81 can solve this small but potentially undesirable problem.

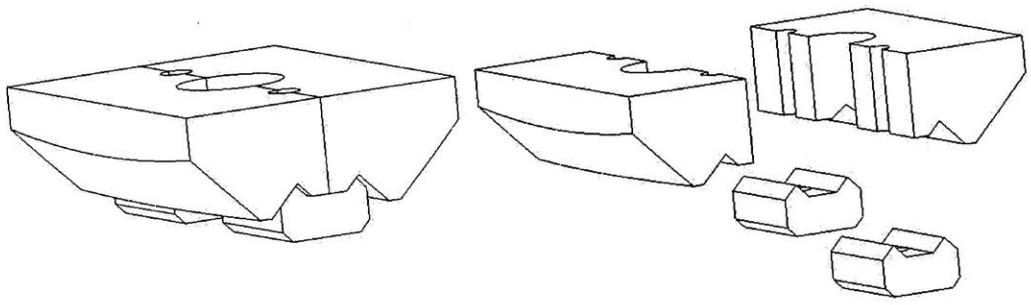

Figure 81: four part canoe ball vee

6 Case Study: A Prototype Machine Concept for Grinding 450mm Silicon Wafers

Chapter 2 deribes the stiffness and error motion requirements for grinding 450mm Silicon Wafers. Chapter 3, 4 and 5 describe hydrostatic bearings and an adjustable kinematic coupling as key elements to the design of machines with an extremely high static and dynamic stiffness. This chapter presents the design of a prototype 450mm Silicon Wafer grinder. Besides a required static stiffness of 1000N/µm, the machine design had to provide:

Work spindle:

- rotational speed of 10 to 500 rpm
- torque of 63Nm
- 500 mm table diameter
- 450mm wafer diameter

Wheel spindle:

- rotational speed of 2500rpm
- 45Nm torque, 11kW net spindle power
- two axes tilt adjust (+/-250μm over 500mm)
- +/-2mm of in process axial stroke
- 8mm of axial adjust to compensate for different wheel geometries or wheel wear
- Rapid feed-rate of 150mm/min
- Feed-rate 1 to 999 μm/min
- 500mm cup wheel for grinding
- Work spindle to wheel spindle axis offset of 249mm

Furthermore it was necessary for the wheel spindle to be able to rise by 300mm relative to the work spindle for wheel changes. There was no error motion or dynamic stiffness requirement for this first generation machine prototype. However, future generation

prototypes will have to meet additional requirements with respect to maximum allowable error motion and minimum required dynamic stiffness, see chapter 2.

Figure 82 to Figure 85 show four face grinding machine concepts. In most of the presented designs the work and wheel spindle are interchangeable. Most of the machines are shown as cantilever based concepts. Other structural concepts (such as bridge type machines) that result in the same motions (degrees of freedom) are not considered separately. In the first and third design the work spindle has no translational degree of freedom. When the tool or the machine part needs to be taken out of the machine the wheel spindle can be moved out of the way. An equivalent design can be implemented with the wheel spindle being movable and the work spindle being fixed. A common design that is similar to Figure 82 are "double-sided large area grinders", where the wafer is supported between two coaxially mounted grinding wheels, Figure 83. "Double-sided large area grinders", have delivered promising results with respect to achievable surface quality and are therefore considered one of the most promising future silicon wafer grinding machine designs [3].

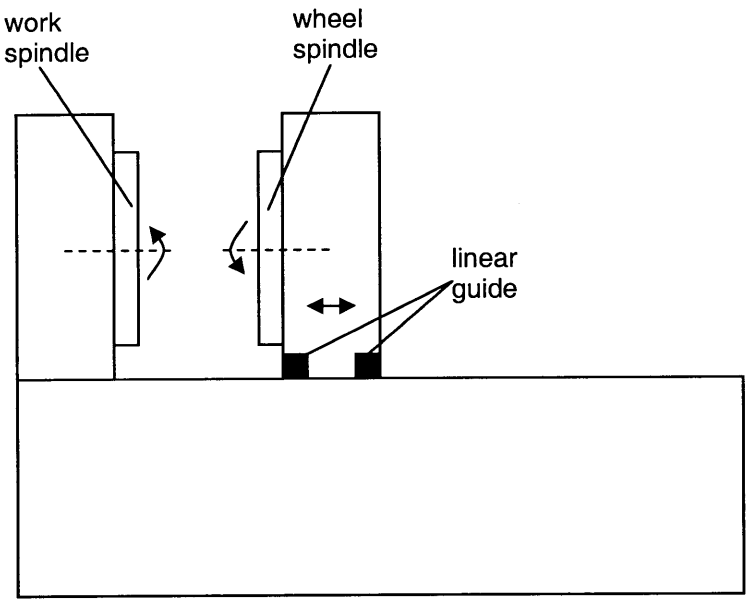

Figure 82: horizontal single axis machine design

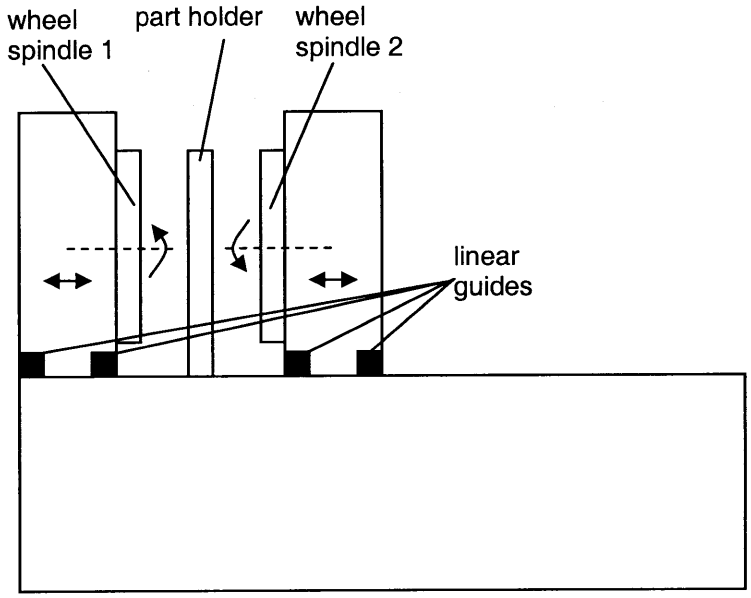

Figure 83: Double-sided large area grinder

Figure 84 is similar to what is known as "chuck based single-side grinding machine", where the grinding wheel axis of rotation and the work table axis of rotation are offset by about half a wafer diameter. Chuck based machine designs are to be optimized with respect to achievable total thickness variation and sub surface damage values.

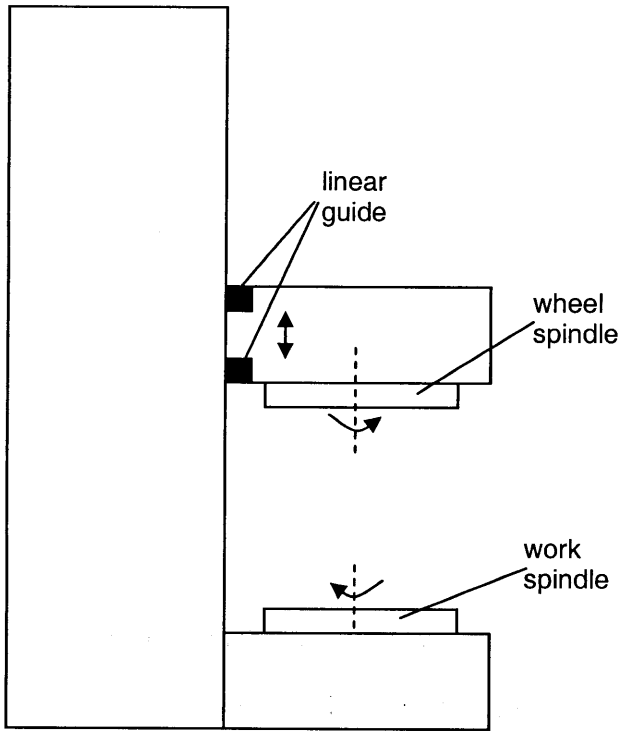

Figure 84: vertical single axis machine design

Figure 85 shows a two axis machine design, where the work spindle can be moved out of the way for tool or part changes. In this design the wheel spindle only requires short stroke motion that is big enough to process the part. However, another axis of motion is required in order to move the work spindle out of the grinding zone.

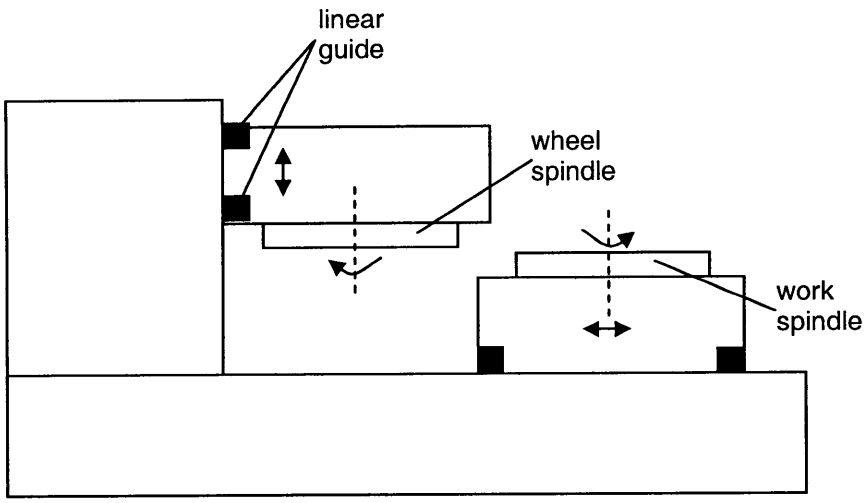

Figure 85: horizontal two axis machine design

All of the presented machine designs share the disadvantage of using large motion bearings as part of the machine's structural loop. In order to maximize machine stiffness, minimize error motions while grinding and reduce the cost of the machine, it is desirable to lock all non essential axis of motion during the grinding process i.e. while grinding only the wheel spindle and work spindle rotation as well as the feed axis should be engaged as part of the machine's structural loop. To disengage/lock all non essential axis of motion a repeatable and stiff locking mechanism or interface is needed. To compensate for wear e.g. in the grinding wheel, this interface needs to be adjustable to some degree. Height adjustable kinematic couplings as described in chapter 5 provide such an interface. With kinematic couplings the machine design of Figure 84 converts into the machine design depicted in Figure 86 and Figure 87.

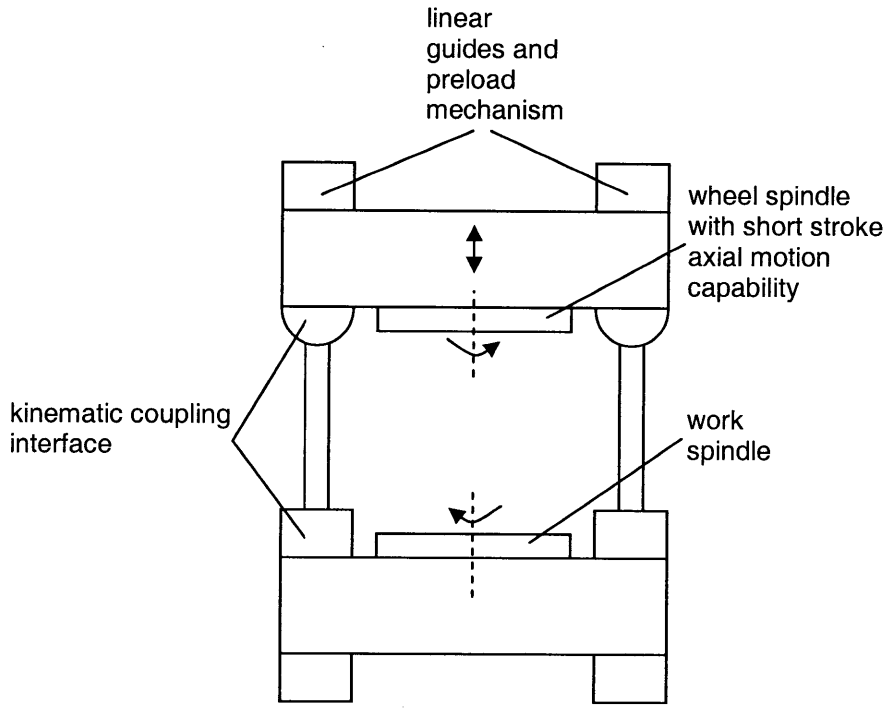

Figure 86: short structural loop kinematic coupling machine design in open configuration

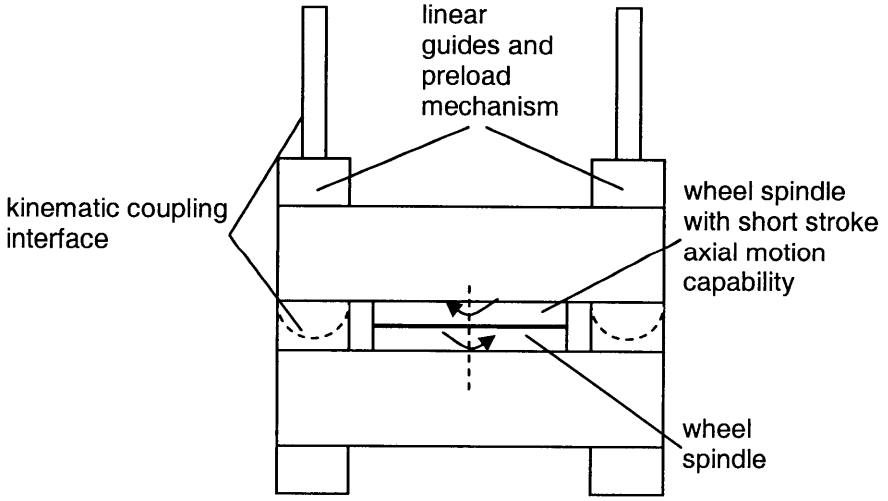

Figure 87: short structural loop kinematic coupling machine design in closed configuration

The machine concept of Figure 86 and Figure 87 reduces the number of moving components and thus potential error sources to a minimum while also allowing for an extremely compact structural loop and thus optimal stiffness. The closed machine

configuration only requires rotation of the wheel spindle and work spindle as well as short stroke axial feeding of the grinding wheel to process the part.

Chapter 3 compares different bearing choices with respect to their use in high required stiffness machinery. Generally speaking, appropriately dimensioned hydrostatic bearings are the top bearing choice where high stiffness, small error motions (smoothness of motion) and minimum wear / process contamination are required. However, a hydrostatic bearing can not provide mm-range axial motion, as it is mandatory for a grinding wheel spindle. A magnetically levitated axial bearing provides high precision which usually comes at the price of low force output and consequently low dynamic stiffness at the order of several hundreds N/µm. Special care must be taken with respect to the dynamic stiffness of electro magnetic spindles to make them useable for future Silicon Wafer grinding machines successful.

The requirements listed at the beginning of this chapter were resolved in a highly compact design (short structural loop) that comprises a fully hydrostatic work spindle with an actively controlled thrust bearing and self compensating hydrostatic radial bearings, an electro-magnetically levitated as well as vertically adjustable wheel spindle (electro magnetic thrust bearing) with self compensating hydrostatic radial bearings and an height adjustable kinematic coupling interface to repeatably open and close the machine by 300mm with the required 8mm of vertical adjust in the closed configuration. Figure 88 shows the machine without the wheel spindle in its open configuration. Figure 89 shows the machine including the wheel spindle in its closed configuration. Figure 90 illustrates the machine in a simplified exploded view.

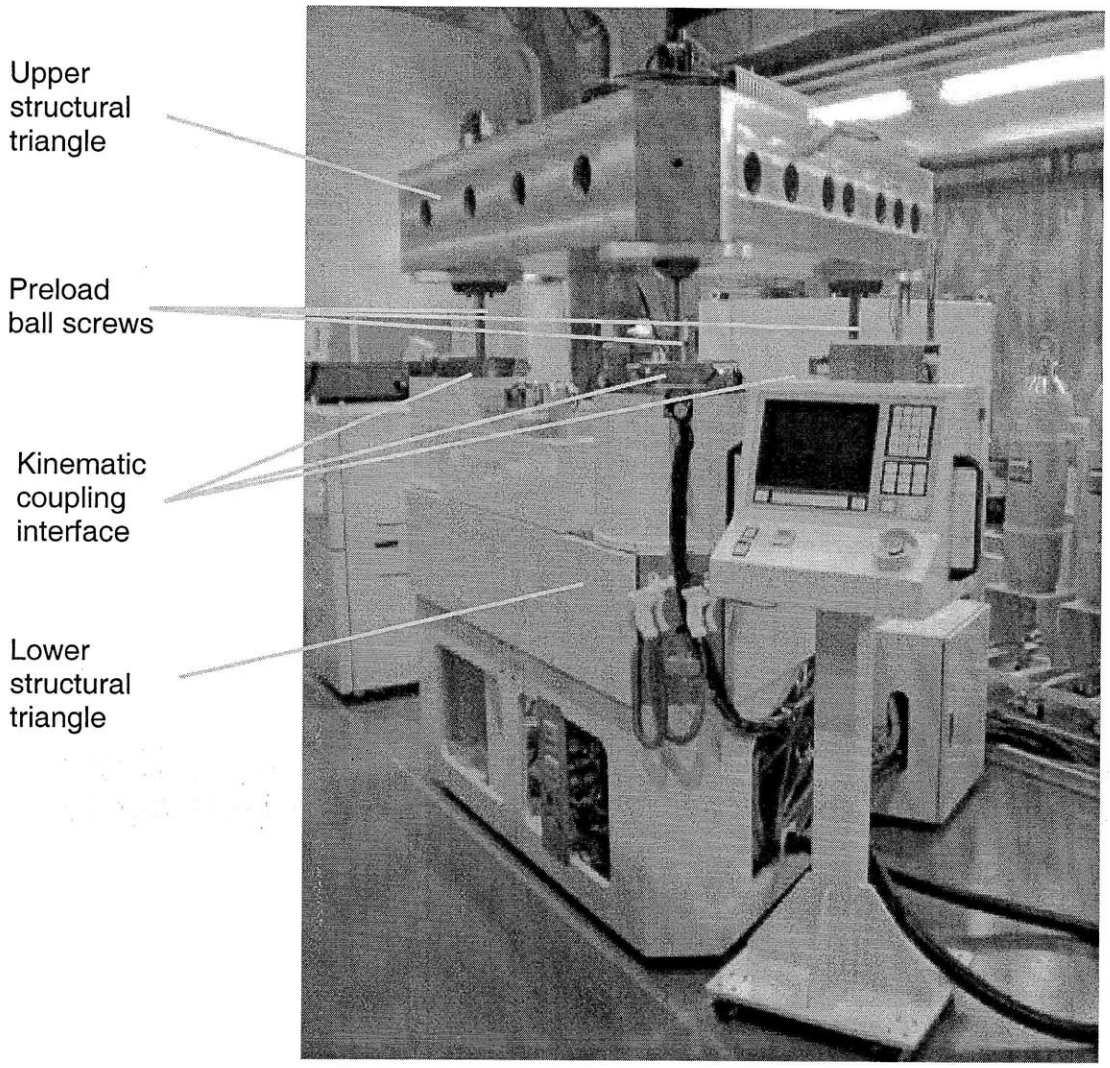

Figure 88: grinding machine prototype without wheel spindle in open configuration

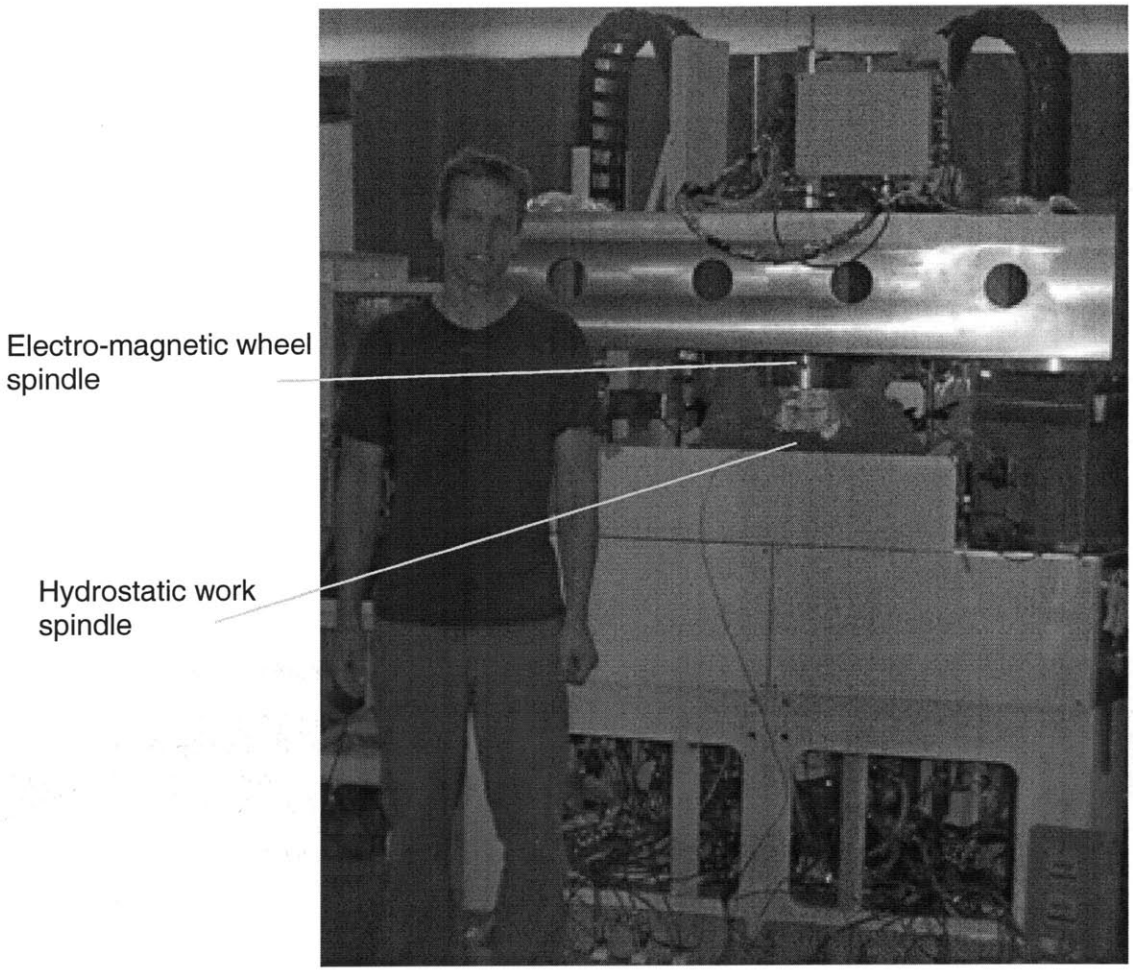

Figure 89: grinding machine prototype with wheel spindle in closed configuration

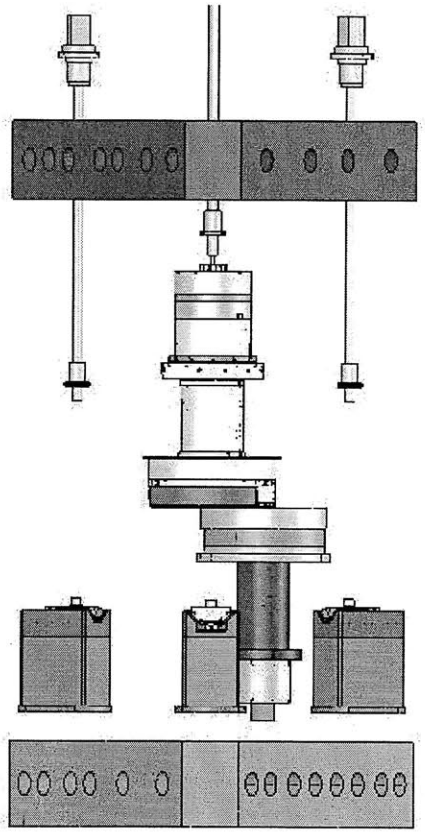

Figure 90: grinding machine prototype exploded view

6.1 Wheel Spindle

The wheel spindle was uses an electro-magnetic levitation bearing with +/-2mm of total axial travel and two self compensating hydrostatic radial bearings that are similar to the radial bearings described in chapter 4.1.1. The heat produced by the winding of the electro-magnetic levitation bearing is controlled through a water cooling circuit that runs through the spindle housing.

Figure 91, Figure 92 depict the wheel spindle.

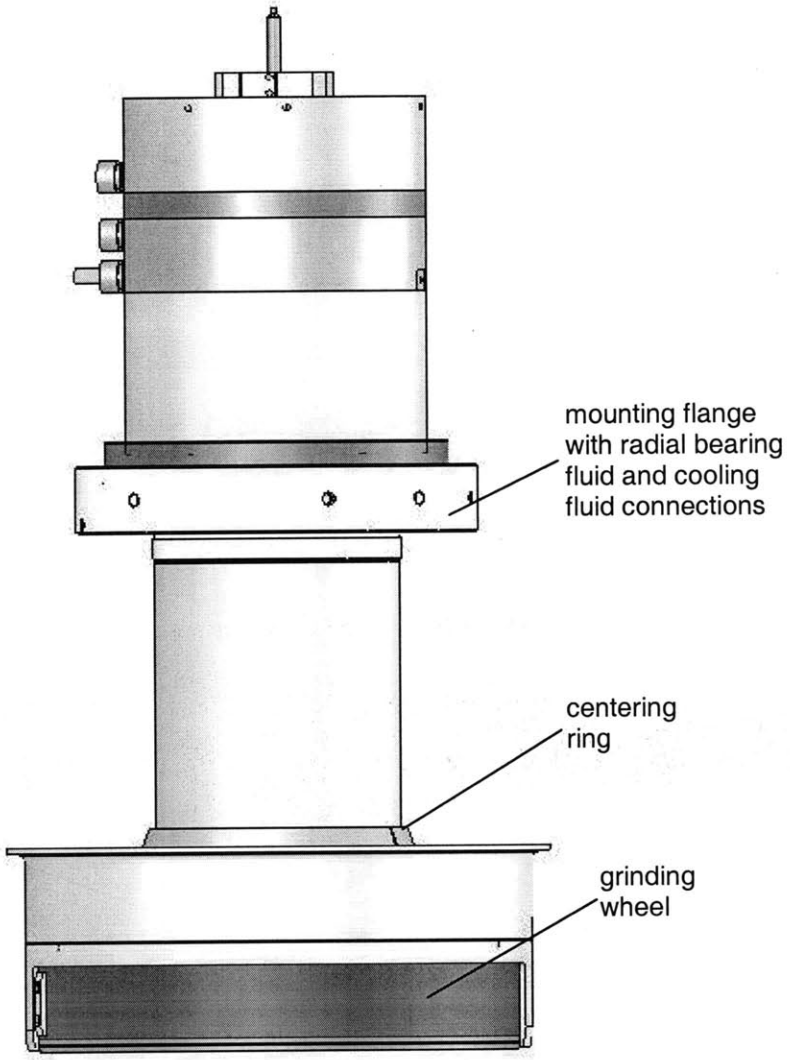

Figure 91: magnetic levitation wheel spindle

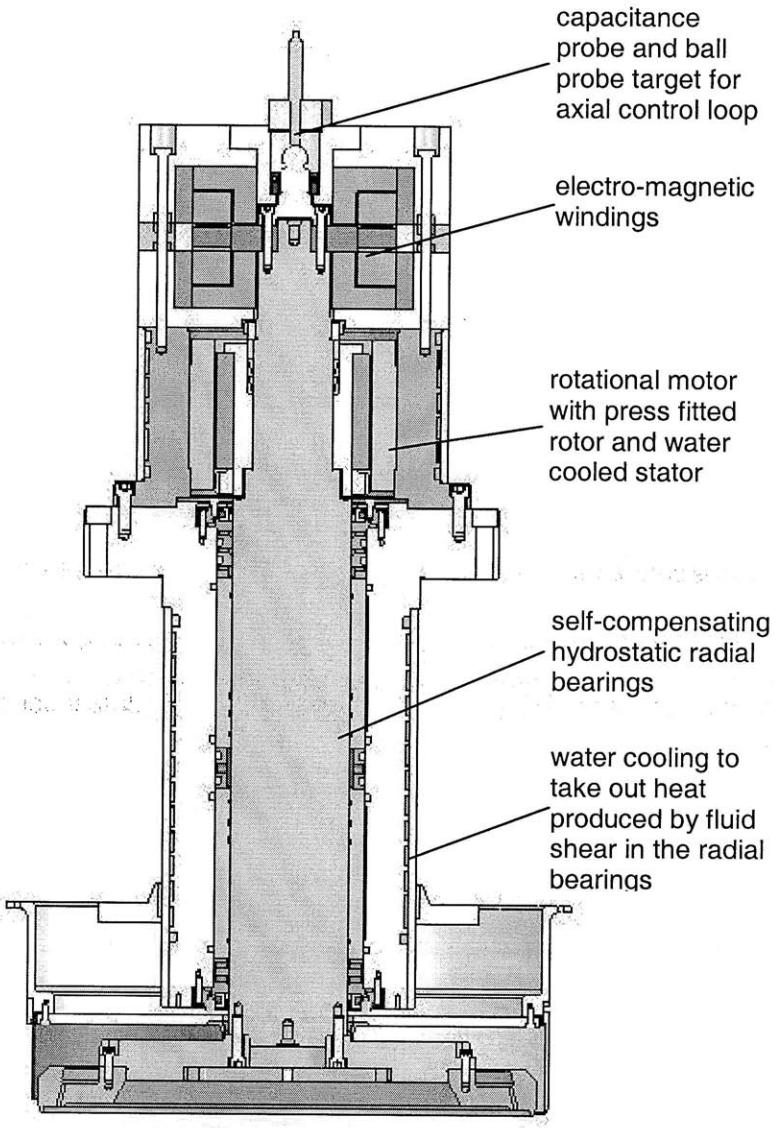

Figure 92: cross section of magnetic levitation wheel spindle

The wheel spindle was designed in close cooperation with the Professur Xiaodong Lu's mechatronics research group at the University of British Columbia.

For more details the reader is referred to Matthew Paone's master thesis, which is available at the University of British Columbia as well as the work done by Professor Xiaodong Lu (University of British Columbia).

6.2 Work spindle

Chapter 4 gives a detailed description of the work spindle. The machine prototype uses an identical spindle consisting of an eight pocket hydrostatic thrust bearing with aluminum oxide and stainless steel bearing plates. This material combination prevents cold welding if the bearing should run dry – which should never happen. A combination of permanent magnets and gravity provide over 7000N of bearing preload and therefore a constant flow stiffness of about 1000N/μm at a bearing gap of 20μm. The work table is centered by two self-compensating hydrostatic radial bearings.

6.3 Structure

The machine structure is composed of the bottom and top triangle as well as the structural parts of the kinematic coupling. To maximize stiffness and minimize manufacturing cost all structural parts have been designed as casting parts. This is rather common for big machinery. Each triangle accommodates either the wheel or the work spindle. The two structural triangles are clamped together via the kinematic coupling interface. The three preload screws of the kinematic coupling are positioned at the corners of the structural triangles. A cross section of the bottom triangle which accommodates the work spindle is shown in Figure 93. Figure 94 shows an FEA of the bottom triangle under 1000N load. Figure 95 shows a cross section of the top triangle, which holds the wheel spindle. An FEA of the top triangle under 1000N load is depicted

in Figure 96. In order to meet the stiffness requirement of Figure 7, the top and bottom triangle were designed for 6.5N/nm.

Figure 97 illustrates the kinematic coupling spacer (see chapter 5) and Figure 98 shows an FEA of the spacer. The stiffness of this part is well beyond 15N/nm. In addition three kinematic coupling contact pairs and thus spacers are in parallel which triples the overall stiffness of the spacer elements. Consequently the spacer elements are stiff enough to not significantly decrease the overall machine stiffness.

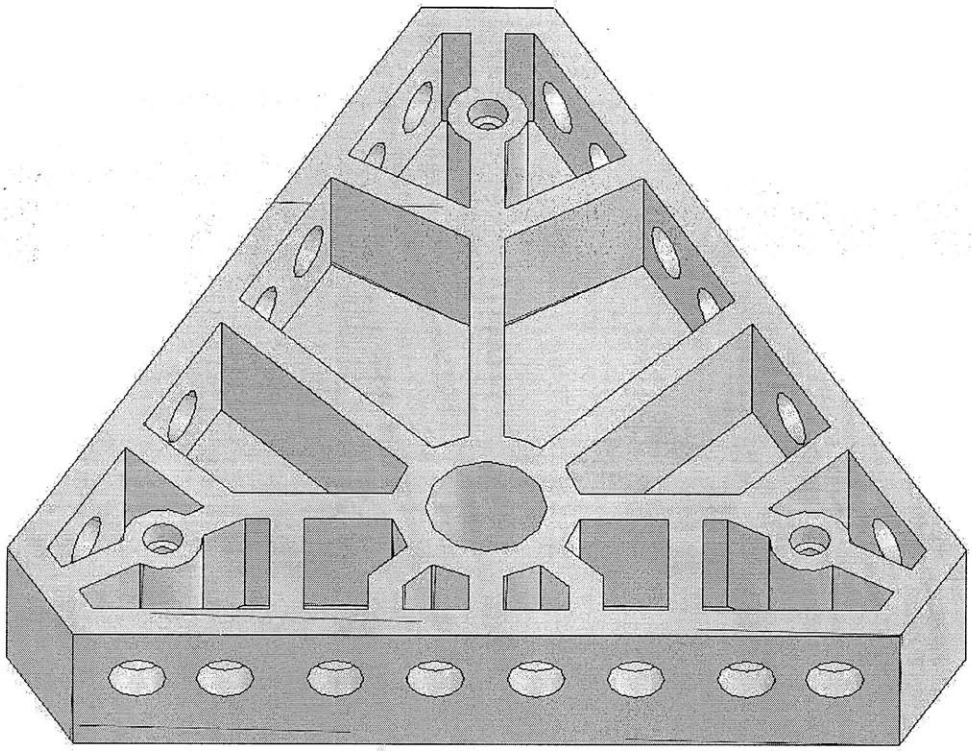

Figure 93: Bottom triangle cross-section

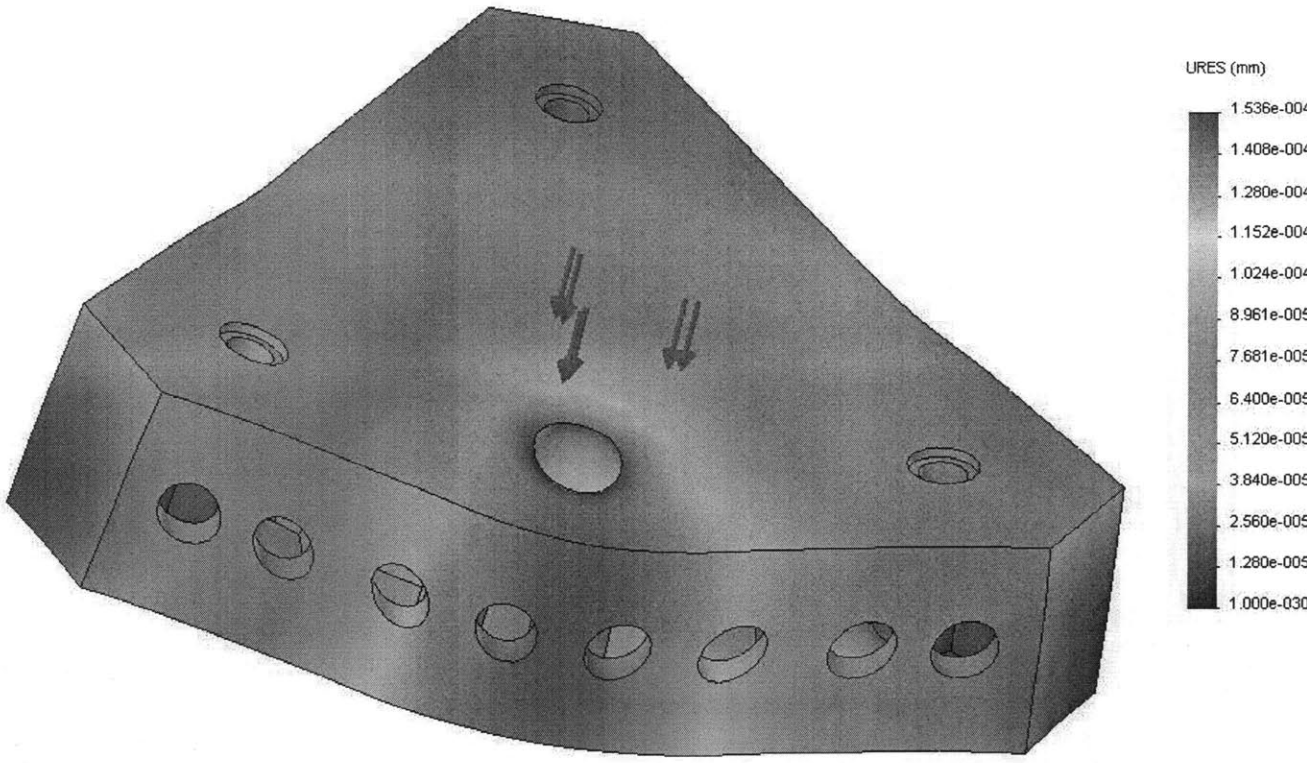

Figure 94: Bottom triangle displacement FEA under 1000N load

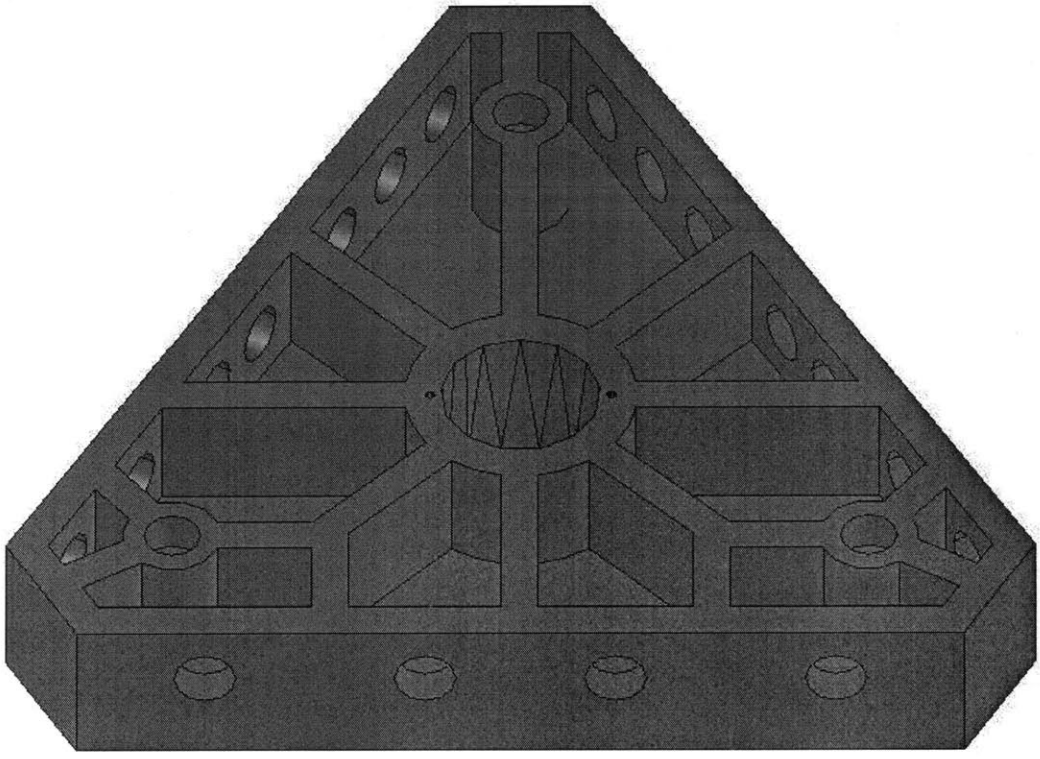

Figure 95: Top triangle cross-section

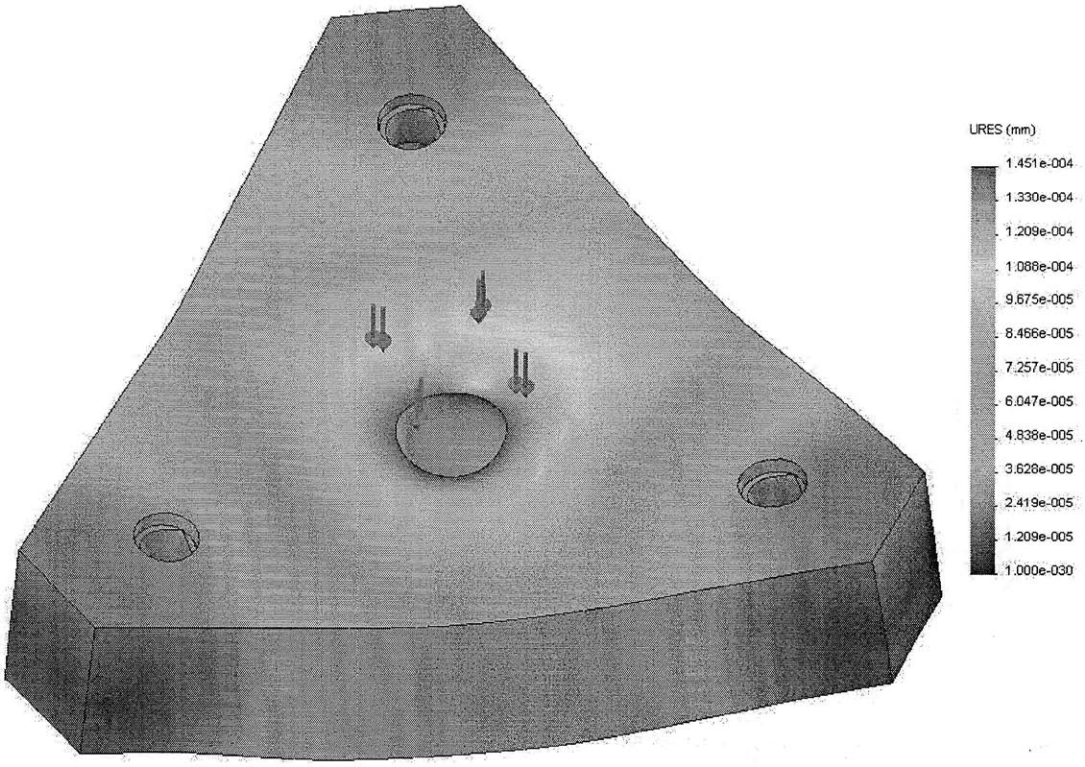

Figure 96: Top triangle displacement FEA under 1000N of load

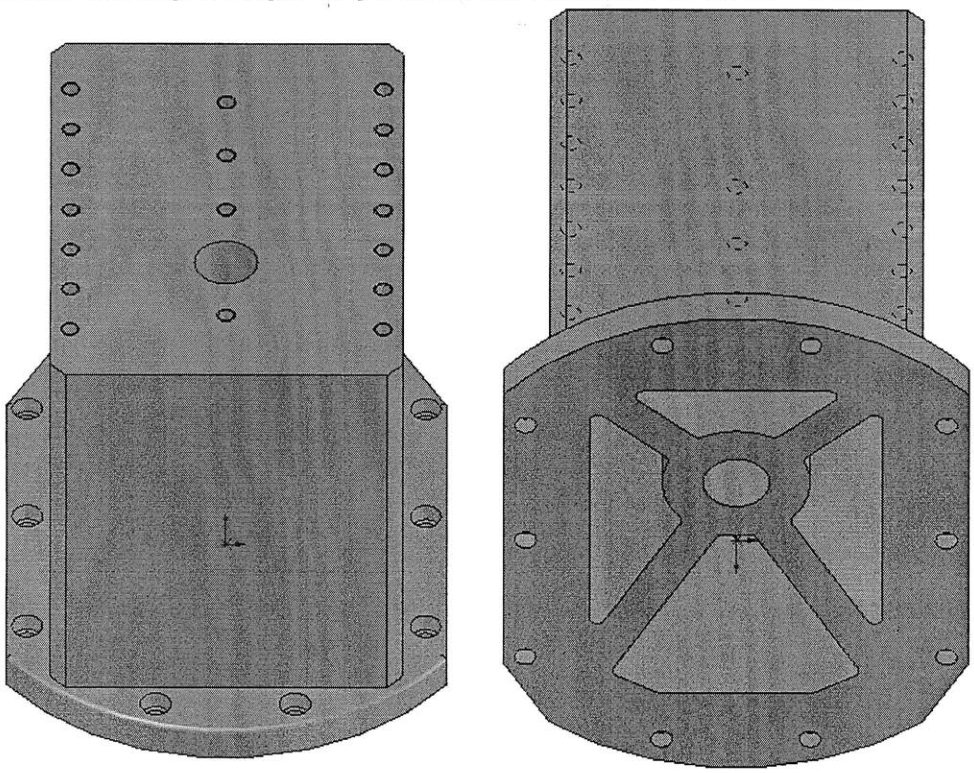

Figure 97: kinematic coupling spacer

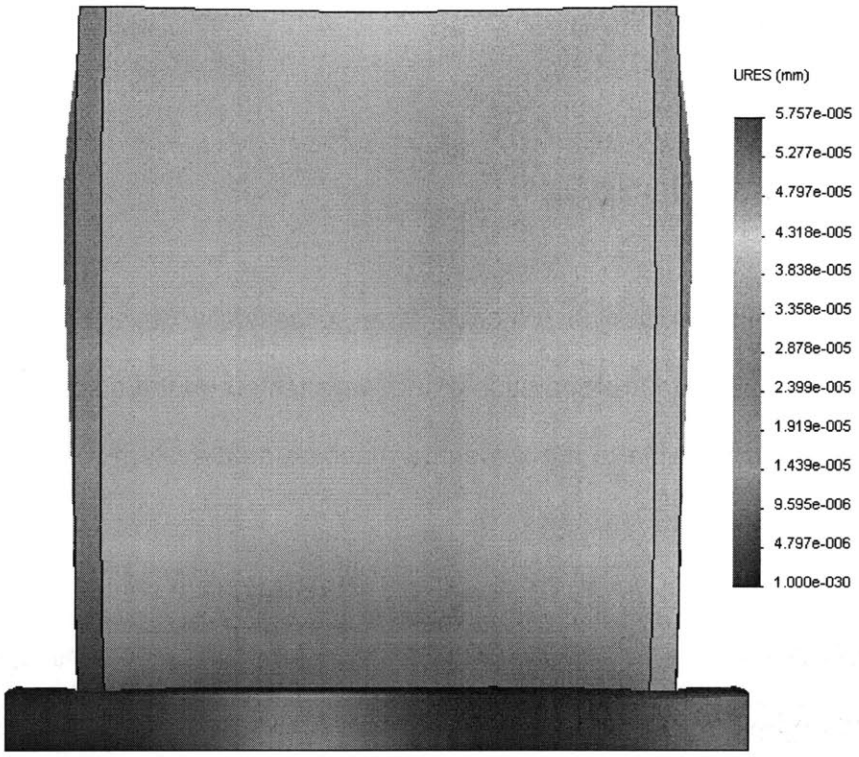

Figure 98: kinematic coupling spacer FEA under 1000N of load

6.4 Solution for Wheel Change

Chapter 5 describes a height adjustable kinematic coupling for use in machine tools with high required stiffness and small error motions. As mentioned at the beginning of chapter 6 a high machine stiffness and small error motions usually coincide with a tight structural loop and few moving components. The machine concept shown in Figure 86 and Figure 87 enables a very compact machine design with a minimum number of moving components.

The kinematic coupling can be opened and closed with high repeatability. In the open configuration the coupling stiffness is made up of the stiffness of the preload mechanism and there is plenty of room for exchanging the grinding wheel or handling the part (wafer). When the coupling is engaged and the machine is working the high kinematic

coupling stiffness (Hertz contact stiffness + preload mechanism stiffness) allows for a very high machining accuracy.

6.5 Conclusions and Outlook

A 450mm Silicon Wafer grinding machine prototype was successfully developed and built. All components of the machine are operational and were tested on the component level. However, it was not yet possible to run the entire machine as a system while test grinding a Silicon Wafer.

While reducing mechanical complexity the proposed design enables an extremely compact machine with a loop stiffness that is two to three times higher than the loop stiffness of common present tool machines.

7 Future Work

In the previous chapters feedback controlled hydrostatic bearings and adjustable kinematic couplings were described as essential elements for the design of future precision machine tools with high required loop stiffness. It was shown how a high machine stiffness is one necessary key to grinding of 450mm diameter Silicon wafers. In Chapter 6 a 450mm Silicon Wafer grinding machine prototype, which incorporates hydrostatic bearings and adjustable kinematic couplings as core functional elements, was presented. The testing of the functional groups of this machine prototype as well as their integration in the machine prototype have proven the potential of the proposed design, but have also revealed several weaknesses on the component level. Future work to eliminate these weaknesses will be essential to make the overall machine design successful. The following paragraphs list suggestions for future improvements.

7.1 Hydrostatic Thrust Bearing

The main limiting factor on the open and closed loop, static and dynamic performance, stiffness and load carrying capacity of the presented magnetically preloaded multi-pocket thrust bearing was the relatively supply system. The used low cost gear pumps were not able to produce a sufficiently pressure independent flow. It was shown that the pump flow per revolution does not only change with applied pressure but also with pump speed. These pump limitations are the main reason for a lower than expected stiffness and load carrying capacity. Furthermore the pump internal leakage (from the high pressure side back to the low pressure side limits the bandwidth of the feedback controlled bearing to load or flow changes.

In order to overcome these limitations it will be necessary to use a pump with an ideally pressure and pump speed independent output flow per revolution or linear displacement increment (real fixed displacement). A pump design that seems rather promising in this respect is a double-acting, large volume piston pump that can supply the bearing over a given duration before it needs to switch direction. The combination of two or more out of phase double-acting piston could even allow continuous operation of the bearing as long as the pressure fluctuations caused by valve switching can be minimized sufficiently.

Alternatively a high flow bearing could be design that can be supplied by a much stronger pump. Consequently load changes would not affect the supply flow by the same % as in the case of a minimum flow bearing. However, this solution can bring up other interesting challenges in the dynamic behavior and control of the bearing.

Besides a constant, pressure and pump speed independent flow per displacement increment an ideal pump should also keep pressure and flow fluctuations to a minimum.

Depending on the bearing damping, the stiffness of the used tubing as well as the inertia of the supported machine parts (floating parts) pressure fluctuations that exceed a certain limit frequency will not affect the bearing anymore (low pass filtering characteristics of bearing and supply system).

In addition to challenges that are related to the supply system, a closer look might have to be taken at the magnetic preload system. Small magnetization tolerances between the magnet elements of the preload magnet ring cause slight eddy currents in the supported steel part. A more uniform magnetization of the magnet ring should eliminate this problem. Furthermore it was noticed that the magnet as well as the supported steel part tend to slowly corrode over time (if tap water is used as bearing fluid). The real machine uses de-ionized water and therefore corrosion might not occur. However, a closer look at possible material combination (rare earth magnet + magnetic stainless steel) with respect to differences in material electro-negativity should be taken. Furthermore high quality magnet powders (lowest possible Neodymium part) as well as coatings are very promising approaches to corrosion prevention.

7.2 Dynamic stiffness of electro magnetic wheel spindle

First tests of the electro-magnetic wheel-spindle at the University of British Columbia have been very promising with respect to accuracy and range of the required +/-2mm of axial adjustment as well as control bandwidth. However, future grinding tests might show the need for a higher dynamic stiffness.

7.3 Kinematic coupling preload control

The adjustable kinematic coupling provides a slightly higher stiffness than was predicted and required. In future designs it might be worthwhile to explore designs that allow for in process (under preload) μm and potentially mm height adjustment. In order to achieve this, it will be necessary to minimize friction at the coupling interface as well as in the preload system.

For applications with a lower required coupling stiffness, an exact constraint aerostatic bearing design can be used to replace the current canoe-ball / vee wedge design.

In order to achieve height adjust under preload, in addition to being low friction and potentially back-drivable, the preload mechanism should also have a rather low stiffness. A low stiffness of the preload mechanism will not substantially decrease the stiffness of the coupling. For this reason a servo-valve controlled, pneumatic piston might be an ideal preload solution for kinematic couplings that also need to be adjustable under load.

Appendix A: Other Machine Designs

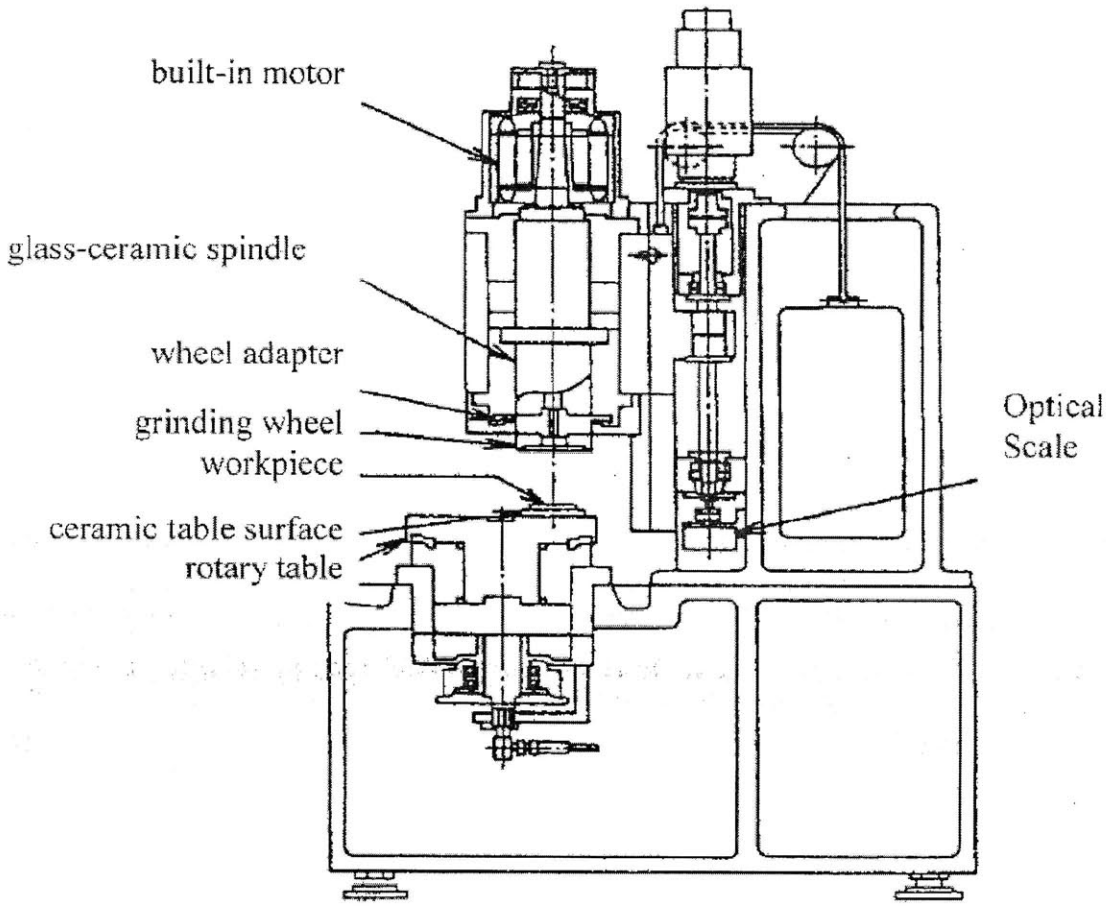

Figure A 1: Focus on thermal stability, glass-ceramic (Zerodur®) spindle, hydrostatic oil bearings for high stiffness and damping, [34]

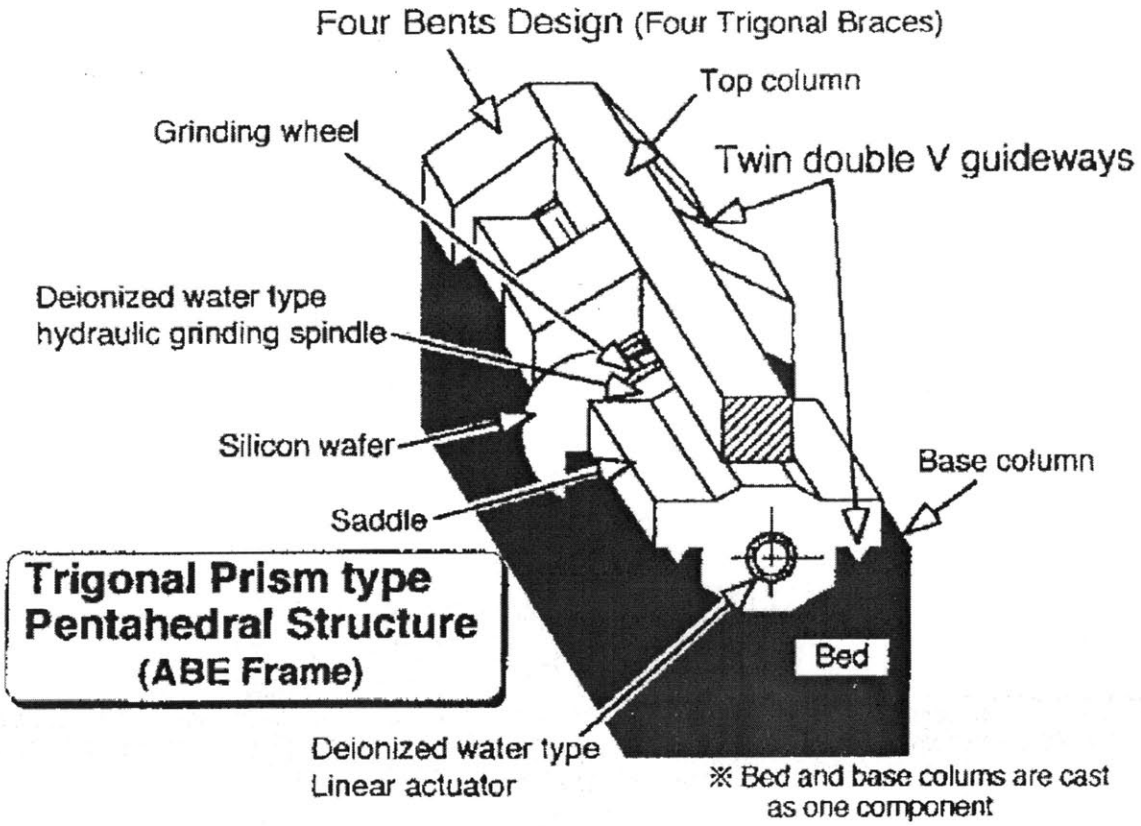

Figure A 2: ≥300mm diameter Si-Wafers, 5nm step positioning resolution of feed axis, hydrostatic actuator, hydrostatic bearings, [35]

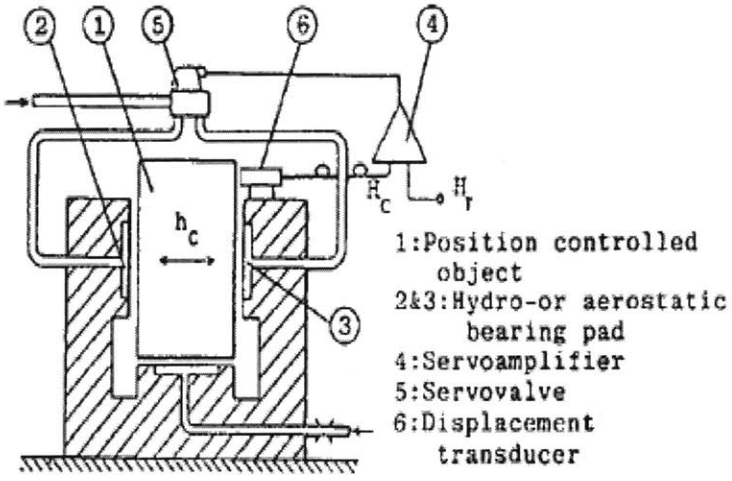

Figure A 3: hydrostatic or aerostatic nm positioning device, [36]

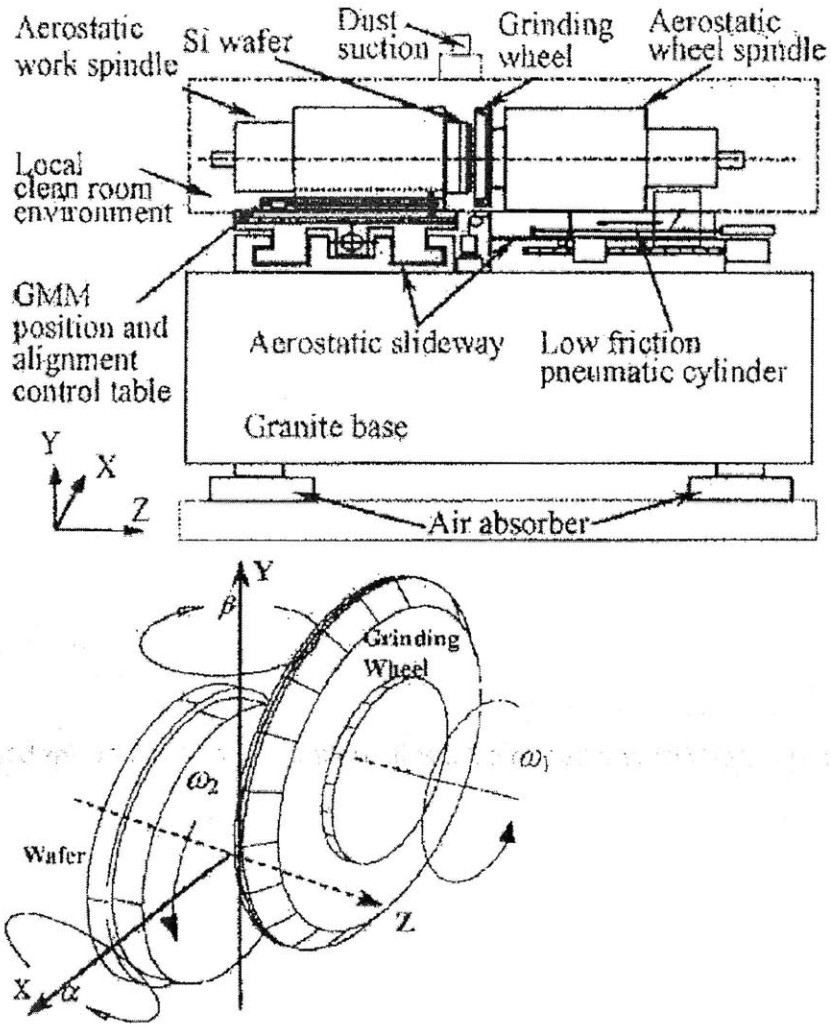

Figure A 4: 300mm Si-wafers, 1nm resolution in x and z spindles, aerostatic bearings driven by lapped lead screws, feed axis can either be driven by low friction air cylinder or lead screw, [37, 38]

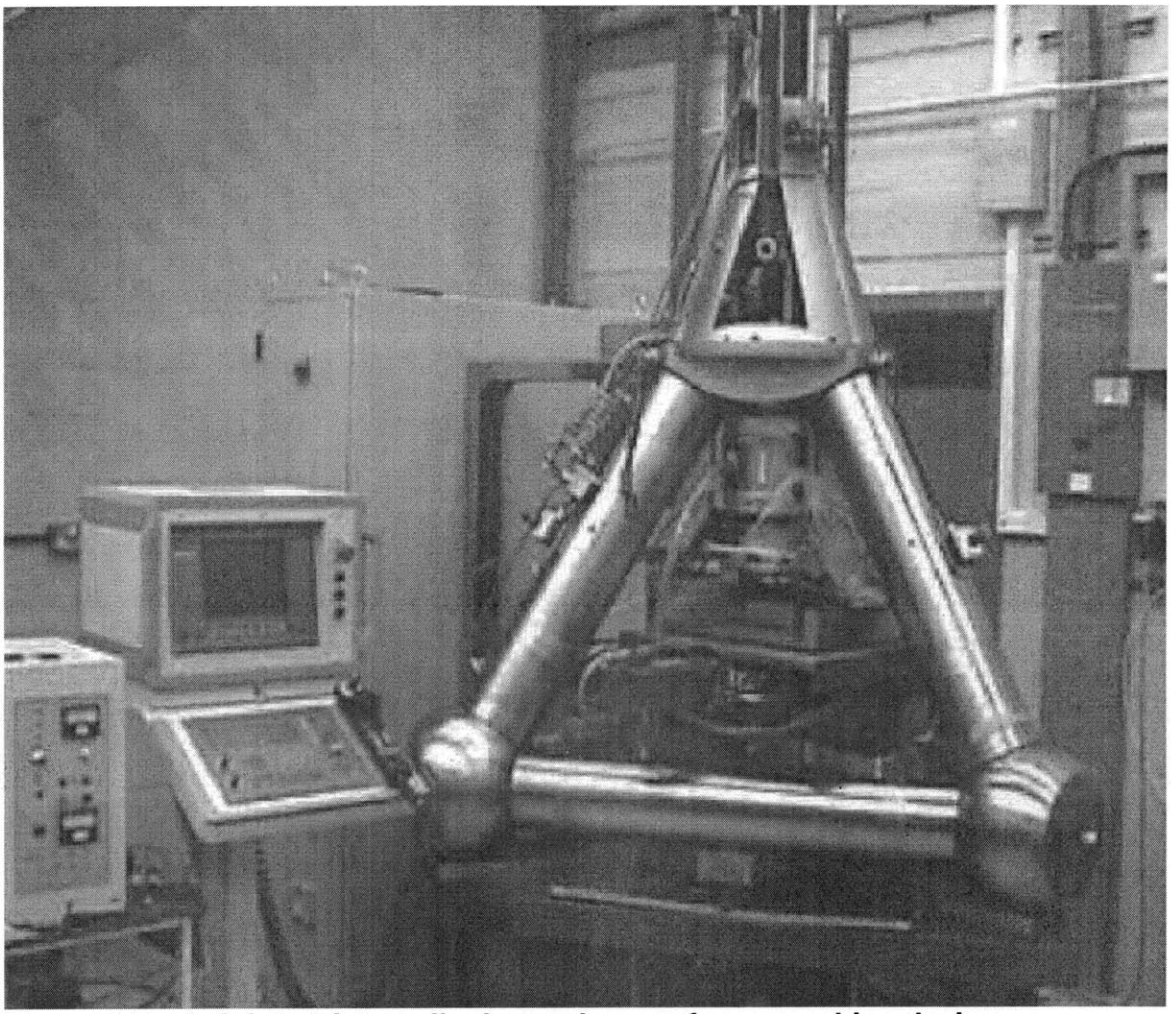

Figure A 5: pin jointed, internally damped space frame machine design

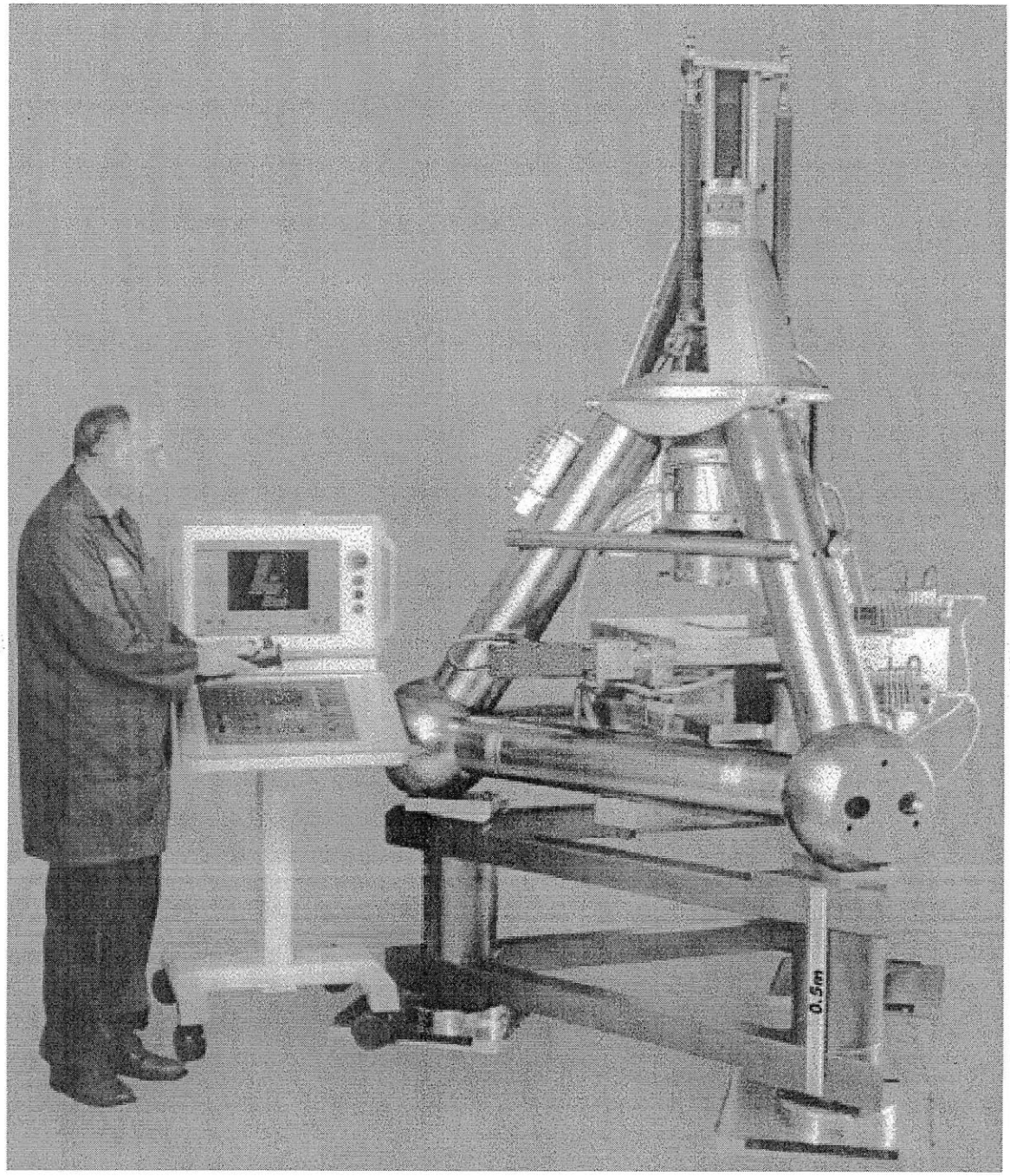

Figure A 6: pin jointed, internally damped space frame machine design, [39]

[1] www.svmi.com/non-siliconwafers.aspx

[2] http://en.wikipedia.org/wiki/wafer_(electronics)

[3] "Precision Machining of Future Silicon Wafers", Prof. Dr.-Ing. Fritz Klocke, Dipl.-Ing. Dietmar Pähler, Fraunhofer Institute for Production Technology (IPT), Aachen, Germany, 2001

[4] "Abrasive Machining of Silicon", H.K. Tönshoff, W. v. Schmieden, W. König, G. Spur, Keynote Paper Annals of the CIRP Vol. 39/2/1990

[5] "Parallelism Improvement of Ground Silicon Wafers." Matsui S.; Horiuchi T.; Transactions of ASME Journal of Engineering for Industry, 2:25, 1991

[6] „Ultraprecision grinding technologies in silicon semiconductor processing", E. Ahearne, G. Byrne, The Advanced Manufacturing Science Research Group, Department of Mechanical Engineering, University College Dublin, Republic of Ireland, Proceedings Instn Mech. Engrs Vol. 218 Part B: J. Engineering Manufacture, 253:267, 2004

[7] "Seiten-Planschleifen von einkristallinen Siliziumseiben ", Spur, G., Holz, B. Jahrbuch Schleifen, Honen, Laeppen und Polieren, 56. Ausgabe (Hrsg.: E. Salije), 1990, Vulkan Verlag, Essen, Germany

[8] http://cnfolio.com/images/img166planar.jpg

[9] "In Process Force Monitoring for Precision Grinding Semiconductor Silicon Wafers", Jeremiah A. Couey (1), Eric R. Marsh(1), Byron R. Knapp(2), R. Ryan Vallance(3), (1) Pensylvania State University, (2) Olympic Laser Inc., (3) Precision Systems Laboratory,

George Washington University, International Journal for Manufacturing Technology and Management, Vol. 7, 430:440, 2005

[10] "Grinding Behaviour of Silicon Wafer and Sintered Al_2O_3 by Constant Force Feeding Grinding System", Hyunjin Kim, Koji Matsumaru, Atsushi Takata and Kozo Ishizaki, Japan, AZojomo Volume 2, August 2006, ISSN 1833-122X, http://dx.doi.org/10.2240/azojomo0219

[11] M. E. Williams, D. L. Trumper, and R. Hocken, "Magnetic Bearing Stage for Photolithography," CIRP Annals - Manufacturing Technology, vol. 42, pp. 607-610, 1993.

[12] E. h. M. Weck and U. Wahner, "Linear Magnetic Bearing and Levitation System for Machine Tools," CIRP Annals - Manufacturing Technology, vol. 47, pp. 311-314, 1998.

[13] H. Shinno, H. Yoshioka, and K. Taniguchi, "A Newly Developed Linear Motor-Driven Aerostatic X-Y Planar Motion Table System for Nano-Machining," CIRP Annals - Manufacturing Technology, vol. 56, pp. 369-372, 2007.

[14] A. C. P. de Klerk, G. Z. Angelis, and J. van Eijk, "Design of a next generation 6 DoF stage for scanning application in vacuum with nanometer accuracy and mGauss magnetic stray field," in APSE 2004 Annual Meeting, Orlando, 2004, [Online], http://www.aspe.net/publications/Annual_2004/PAPERS/3NANO/1552.PDF, [Sept. 20, 2009].

[15] M. Holmes, D. Trumper, and R. Hocken, "Atomic-Scale Precision Motion Control Stage (The Angstrom Stage)," CIRP Annals - Manufacturing Technology, vol. 44, pp. 455-460, 1995.

[16] "Hydrostatic Lubrication", Bassani, Piccigallo, Elsevier, 1992

[17] "Hydrostatic and hybrid bearing design", W.B. Rowe, Butterworths, 1983

[18] "The Theoretical Flow Ripple of an External Gear Pump", Noah D. Manring, Suresh B. Kasaragadda, Mechanical and Aerospace Engineering Department, University of Missouri-Columbia, MO, Transactions of the ASME Journal of Dynamic Systems, Measurement and Control, Vo. 125, Sep 2003; 396-404; http://dx.doi.org/10.1115/1.1592193

[19] www.wikipedia.com, rare earth magnet

[20] www.vacuumschmelze.de

[21] http://pergatory.mit.edu/perg/research/archive/Kotilainen/hydrobushing.htm

[22] "Parametric Design and Optimization for a Nonlinear Precision X-Y Microstage", James B. Taylor1, Andres L. Carrano2, Yahya Fathi1, 1Dept. of Indust. Eng., NC State University, Raleigh, NC, USA, 2Dept. of Indust. Eng., Rochester Inst. of Tech., Rochester, NY, USA, Journal of Manuf. Syst., Vol. 19/No. 4, 2000

[23] "Precision X-Y Microstage with maneuverable kinematic coupling mechanism", James B. Taylor 1, Jay F. Tutu 2, 1 Dept. of Indust. Eng., NC State University, Raleigh, North Carolina, USA, 2 School of Eng., Purdue University, West Lafayette, IN, USA, Prec. Eng. 18:85-94, 1996

[24] "Design of Accurate Repeatable Kinematic Couplings", Martin Culpepper, Carlos Araque, Marcos Rodriguez, Dept. of Mech. Eng., MIT, Cambridge, MA, USA

[25] "A dual-purpose positioner-fixture for precision six-axis positioning and precision fixturing Part I. Modeling and design". Kartik M. Varadarajan, Martin L. Culpepper, Dept. of Mech. Eng., MIT, Cambridge, MA, USA, Prec. Eng. 31: 276-286, 2007

[26] "A dual purpose positioner-fixture for precision six-axis positioning and precision fixturing Part II. Characterization and calibration." Karitik M. Varadarajan, Martin L. Culpepper, Dept. of Mech. Eng., MIT, Cambridge, MA, USA, Prec. Eng. 31:287-292, 2007

[27] "Kinematic Couplings for precision fixturing – part 1: Formulation of design parameters.", A. Slocum, Dept. of Mech. Eng., MIT, Cambridge, MA, USA, Prec. Eng. 10:85-91, 1988

[28] "Kinematic Couplings for precision fixturing-part 2: Experimental determination of repeatability and stiffness.", A. Slocum, A. Donmez, Dept. of Mech. Eng., MIT, Cambridge, MA, USA, Prec. Eng. 103:115-122, 1988

[29] "Precision Machine Design", A. Slocum, Dept. of Mech. Eng., MIT, Cambridge, MA, USA, Prentice Hall, Englewood Cliffs, NJ

[30] "Design of three-groove kinematic couplings.", A. Slocum, Dept of Mech. Eng., MIT, Cambridge, MA, USA, Prec. Eng. 14:67-73, 1992

[31] "Compliant kinematic couplings for use in manufacturing and assembly." Martin L. Culpepper, Alexander Slocum, Dept. of Mech. Eng., MIT, Cambridge, MA, USA, Proc. of the 1998 ASME Int. Mech. Eng. Congress and Expo.. 1998, p.611-8

[32] "Principles and Techniques for Designing Precision Machines", Layton Carter Hale, MIT, Cambridge, MA, USA, PhD Thesis, p.105ff, 1999

[33] "Air bearing kinematic couplings", John Ziegert, Vadim Tymianski, Department of Mechanical and Aerospace Engineering, University of Florida, Gainesville, FL, USA, Prec. Eng. 31:73-82, 2007

[34] "A. Ultraprecision surface grinder having a glass±ceramic spindle of zero-thermal expansion", Namba, Y., Wada, R., Unno, K. and Tsuboi, *Ann. CIRP*, 1989, **38**(1), 331±334.

[35] "Development of a ductile mode double disk grinding machine with trigonal prism type pentahedral structure for super-large and super-flat silicon wafer", Abe, K. and Isobe, S., Proceedings of the 1st EUSPEN Topical Conference on *Fabrication and Metrology in Nanotechnology*, Copenhagen, Denmark, 28±30 May 2000, Vol. 1, pp. 26±33.

[36] "Nanometer Positioning Characteristics of Closed Looped Differential Hydro-or Aerostatic Actuator", A. Kanai, Tokyo Metropolitan University, and M. Miyashita (2)/Japan - Submitted by T. Hoshi,

[37] "State of the art technologies and kinematical analysis for one-stop finishing of 300mm Si wafer", Zhou, L. B., Eda, H. and Shimizu, J., J. Mater, Processing Technol., 2002, 129, 39±40.

[38] "Development of single step grinding system for large scale 300mm Si wafer: a total integrated fixed abrasive solution", Eda, H., Zhou, L., Nakano, H., Kondo, R. and Shimizu, J.; Ann. CIRP, 2001, 50(1), 225±228

[39] Ultra-precision finishing of brittle materials (e.g. glass), pin jointed, internally damped space frame", Lindsey, K. Tetraform grinding. Proc. SPIE, 1991, 1573, 129±135.